Phosphide based type-II stacked quantum dot arrays enhancing carrier spatial separation for multi-junction III-V/Si photovoltaic application.

(III-V/Si 多接合太陽電池用キャリア空間分離促進型リン系 type-II 積層量子ドット)

January 2021

Doctor of Philosophy (Engineering)

Piedra Lorenzana Jose Alberto

Toyohashi University of Technology

Abstract

GaP based III-V-N materials have attracted attention as absorber layer in solar cells for their large tunable band gap which cover 1.5-2.0 eV under lattice matching conditions to silicon. Despite this advantages III-V-N growth on Si remains as a complicated task to overcome due to the generation of structural defects, such as threading dislocations, stacking faults and antiphase domains. Optimization of growth conditions and understanding of GaP epitaxy is essential for the integration of III-V-N materials and Si substrates by GaP/Si heteroepitaxy. Along with the crystal defects originated from the interface carrier recombination due point defects and N-composition inhomogeneity result in poor conversion efficiency.

Accomplish high crystal quality epitaxy of GaP on Si substrate has been achieved through great effort. Diffusion length of adatom on the grown surface is one of the decisive factors to understand the growth mechanism since for techniques such as MBE it operates outside the thermodynamic equilibrium and the interaction between the adatoms, for growth temperature of 550 °C and 600 °C it seems that the diffusion mechanism is affected by the interaction of the Ga adatom and the dimers of the (2×4) surface reconstruction. It was concluded that the GaP (001) exhibits similar diffusion mechanism as the GaAs (001) for some growths conditions This behavior is also important in the formation of nanostructures such as quantum wells and quantum dots.

The goal of this work is to contribute to the achievement of efficient III-V-N photovoltaics on Si substrates. First, I focus on the diffusion mechanism of GaP homoepitaxy growth by the estimation of the diffusion lengths of two principal axes and its relation to the growth temperature. Directional anisotropy was observed along the $< 110 >$ and $< 1\bar{1}0 >$ directions. This anisotropy is highly consistent with the surface morphology, that if islands are formed, elongation of the growth island along $< 1\bar{1}0 >$ is also consistent with larger diffusion length along the $< 1\bar{1}0 >$ direction. This anisotropy is useful for the self-annihilation of the antiphase domains in the GaP/Si heteroepitaxy. In the results for low growth temperature there is not strong anisotropy of diffusion lengths, so the self-annihilation of antiphase domains is less likely to occur.

Then for the improvement of III-V-N solar cells efficiency, it was proposed a type-II band alignment QDs in a InP/GaAsPN stacked structure for the improvement of the carrier recollection. Type-II band alignment produce the carrier spatial separation, by this it is expected recollect carriers with the QDs, and with a stacked QD structure been able to extract them from the GaAsPN solar cell. First, I focus on the formation of self-assembled InP Quantum dots (QD)s on GaP. Several growth conditions were studied. For most of the studied conditions two types of QDs were observed characterized by their geometry. It was found that for low growth rate and V/III ratio more uniform and smaller QDs can be produced, a transition in QD size was observed for specific conditions. since the nucleation of larger QDs tends to generate crystal defects, these conditions should be avoided. The InP QD growth conditions used in the present work were far from typical ones for InP homoepitaxy, i.e., very low growth rate and very low P overpressure. Considering these situations, the effect of the V/III ratio and/or growth rate on InP QD size can be dominated by the rate of P desorption from the various facet surfaces that form the InP island.

Capping process and stacking of QDs was studied. Growth interruption process during the capping of the QDs was used to improve the homogeneity of the stacked QDs. Optimized growth condition of 0.025ML/s and V/III ratio of 20 together with a two-step growth interruption consisted of a removal of excess In atoms from the top of the QD by the growth interruption of the partial capped QD, and the posterior flattening of the GaP capping layer by a second growth interruption process. Two samples were prepared for the two-step growth interruption

evaluation, One included the growth interruption process and the second was grown without that process. For the sample without the growth interruption, the size of stacked QD increased and defects appeared in route of stacking. In contrast, sample with the proposed method, clear stacking of the InP QDs through the layers was present. In this case, the height of the QDs was slightly increased from 3 to 4 nm from the bottom to the top layers proved to control the QDs size and uniformity. Achieving a good quality 30 period InP/GaP structure without the implementation of any strain compensation layers.

These results can be applied in the following GaAsPN material. And may help in designing more efficient GaP-based III–V–N solar cells on Si substrates.

Acknowledgements

During the time that I have remained in the Toyohashi University of Technology, I had the pleasure of meeting and working with many people who had contributed to this work in many ways. It is difficult to thank all of them properly in this small space and sorry for been so bad expressing myself. Beforehand I apologize for the people that will not mention probably I just do not know how to write your names.

First, I would like to thank my advisor Dr. Wakahara Akihiro, who allowed and welcomed me to join his research group and all the support that he has provided me from the procedure concerning to my scholarship until the present day. His patience, dedication and eagerness to his students provided a great working environment. His advice and discussion allowed me to complete the PhD course.

I would also like to thank to Dr. Yamane Keisuke, who also supervised and greatly contributed with discussion and council to this work. The contribution to the guidance and maintenance in the laboratory is priceless.

To Shiota Koki who helped me during the long hours of sample fabrication and preparation.

To all the members of the optoelectronic group who had helped me with any research related issue or even with the language. I believe this group distinguishes by its strong friendship bounds.

Dr. López Máximo who introduced me to this field and provided the contact with Dr. Wakahara.

To all the university staff that has provided support.

I want to thank to all the friends that I had the chance to made, since coming to a foreigner country can be a real challenge. The support and joy founded in that many relationships have been a fuel in this process. There are so many names that I cannot recall all of them. To all the Mexicans that I met for the first time here and continue to chat. To all the foreigner students that had showed me a small piece of so many different cultures. Special thanks to Ernesto, Armando, Ricardo, Enrique, Paola, Martin, Tania, Shougo, Keisuke, Florent, Min, Nihan and Olivia for all their support in the hardest times. Karen and Chihiro will always be in my thoughts, see you in the next life Lily.

To my friends in Mexico that despite the distance can still make the same old jokes.

To my beloved parents José and Patricia who had provided love and had supported through everything in order to fulfill my dreams. To my siblings whom I still turn for advice. Thank you for always been there for me.

To the Japanese Government by the Ministry of Education, Culture, Sports, Science, and Technology (MEXT) for financial support through the Monbukagakusho scholarship.

Table of contents

Chapter 1 Introduction

1.1 Photovoltaic devices

In the last years, the effort for the generation of clean energy has continuing growing since the whole society is completely dependent of the electricity and the continue energy consumption seems to never end. The photovoltaics materials have gained their place in the research due to its potential to cover the human needs. This started with p-n junction silicon device in 1954[1]. Since then, several materials and devices have been fabricated to fulfill the requirements, the silicon based solar cells remains as a popular material in solar cells. Solar cells can be classified in what is known as generations, usually three generations are mentioned.

Silicon solar cells are the so called first generation of photovoltaics, it took advantages of the processing feedback and supply feedstock provided by the microelectronics industry[2]. The second generation of solar cells was developed as a cheaper alternative to crystalline silicon cells. They provided better mechanical properties, allowing more flexible utilization, but at the expense of lower efficiency. This thin film employed new growth methods. The second generation solar cells are mainly based on copper indium gallium selenide (CIGS), CdTe, and amorphous silicon later achieving efficiencies around 22%[3]. The third generation is composed of perovskite, organic, tandem, dye-sensitized, and other emergent concepts with potential to overpass the limitations of previous photovoltaics generations. These consist of low-cost low efficiency systems to high cost-efficiency system (mainly III-V multijunction). In the Figure 1.1 It is shown a chart with the maximum solar cell efficiencies achieved.

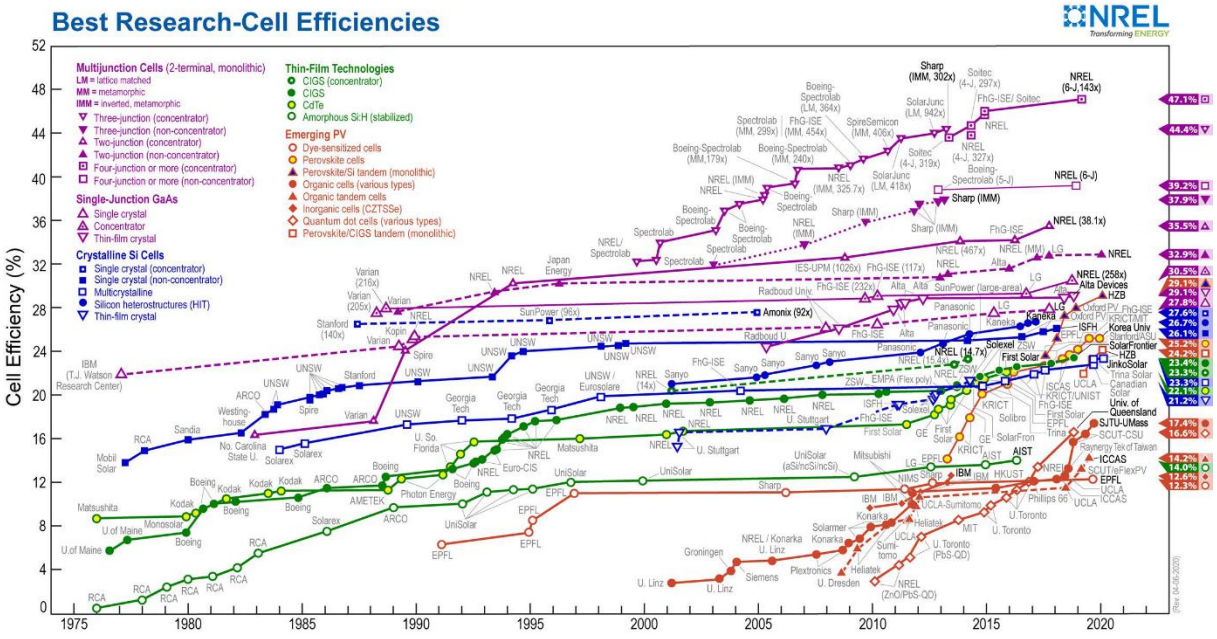

Figure 1.1 Maximum solar cell efficiency achieved for the different types of solar cells. This plot is courtesy of the National Renewable Energy Laboratory, Golden, CO. https://www.nrel.gov/pv/cell-efficiency.html

1.2 P-N junction and efficiency losses

Semiconductors can be classified depending on the carrier concentration as intrinsic and extrinsic semiconductors. The pure form of the semiconductor is called as intrinsic and the semiconductor in which intentionally impurities are incorporated to change the electrical properties of the material is called extrinsic. If the semiconductor is doped with atoms that can accept electrons, it is known as p-type which uses the lack of electrons, called holes, to increase its conductivity. Likewise, if it is doped with atoms that can donate electrons, it is called a n-type. In the case of Si when it is doped with Arsenic or Phosphorus atoms, which has one extra valence electron per atom. When the dopant atom enters in the lattice, substitute for one Si atom while bounding with 4 Si atoms release its extra valence electron into the Si lattice. Obtaining a n-type semiconductor. A p-type Si is obtained when a Boron or Gallium atoms enter in the lattice and substitute a Si atom while bound to four others and accept an electron from an adjacent atom. In this way the lack of electron, or hole, moves through the valence band of the material, making it conductive.

Solar cells are typically made from the union of a p-type and n-type materials, this is called a p-n junction. When the p and n regions are brought together, the large carrier concentration gradients at the junction cause diffusion. Holes from the p-side diffuse into the n-side, and electron from the n-side diffuse intro the p-side. As hole continue to leave the p-side, some of the negative acceptor ions near the junction are left uncompensated because the acceptors are fixed in the semiconductor lattice, whereas the holes are mobile. Similarly, some of the positive donor ions near the junction are left uncompensated as the electrons leave the n-side. This space charge region creates an electric field that is directed from the positive charge toward the negative charge as indicated in the Figure 1.2(a). This happens until the valence band (E_v) edge in the p material almost lines up with the conduction band edge (E_c), as shown in the Figure 1.2(b). Due to electric filed, the diffusion of the carriers cannot continue indefinitely, the electric field promotes a flow of charge, known as drift current, that opposes and eventually balances out the diffusion of electrons and holes. When a photon is absorbed in the solar cell and excites and electron from the ground state or the valence band in the p material to an excited conduction band state, then this electron become mobile in the conduction band and if it lives long enough in this excited state, it can diffuse to the junction and fall down the potential barrier where it can be collected as in Figure 1.2(c). In order to excite the electron from the valence band to the conduction band, the photon must have an energy equal or larger than the band gap of the semiconductor.

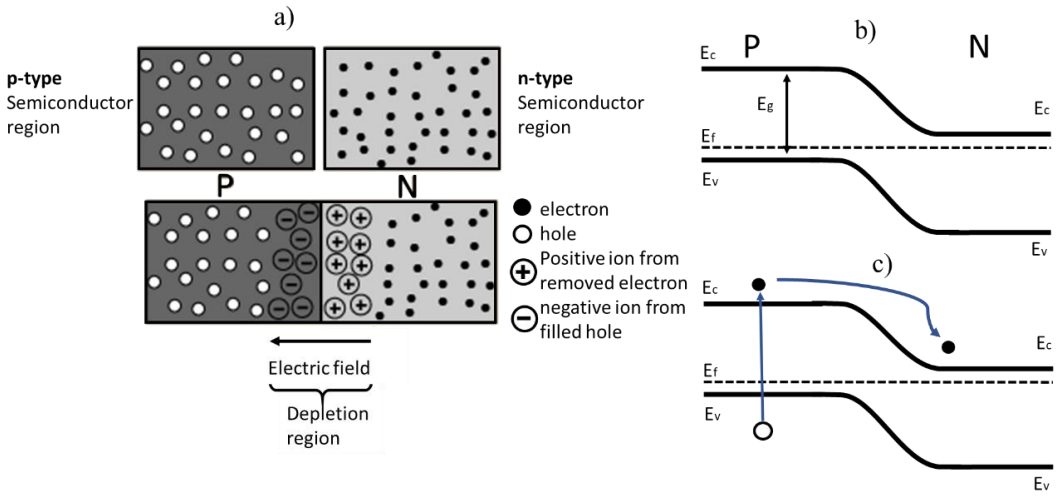

Figure 1.2 Schematic of a p-n junction and electric field in the depletion region a). Band diagram of the p-n junction b). Photon absorption that excites an electron into the conduction band.

Many processes exist that produce a loss in the overall efficiency in the solar cells such as transmission and thermalization loss, junction and contact voltage loss, and recombination loss. The light that arrives to the solar have specific values of energy, as mentioned before it is needed that the photons that excites the electrons from the valence band to the conduction band to have an energy at least as the band gap energy, photons with lower energy will be lost as transmission and thermalization, for photons with higher energies than the band gap the photo excited electron-hole pair will lose the energy that excess the bandgap in a similar way. This process is shown in the Figure 1.3 as 1 and is the main loss in efficiency in p-n junction solar cell. These losses limit the conversion efficiency of a cell to about 44%.

Recombination of the photoexcited electron-hole pairs is another important loss process. Defects within the cell and the lifetime of photogenerated carriers are two main factors than can reduce recombination loss. Lifetime of photogenerated carriers can be increased with the reduction of defects, by achieving this the lifetime can be ideally determined by radiative recombination in the cell which is the inverse process of the photoexcitation process. As shown by Shockley and Queisser[4] this symmetry between light absorption and light emission during radiative recombination can be used to derive fundamental limits on achievable solar cell performance. From this, solar cell can be considered as a black body of a 300 ºK temperature. From the difference between absorption and emission angles arises the Boltzmann loss, accounting for a reduction of 10% of the overall efficiency[5]. Since recombination between electrons and holes at different energies in the conduction and valence band occurs, the emitted radiation increases exponentially as the voltage across the cell increases at least for photon energies above the bandgap.

When open circuited, the voltage of the ideal cell builds up so that the number of above bandgap photons emitted as part of this voltage enhanced radiation balances the number in the incoming sunlight. At voltages below open circuit, the number of emitted photons is less, the difference between incoming and outgoing photons being made up by electrons flowing through cell terminals. For a band gap of 1.34 eV the Shockley and Queisser limit of efficiency is 33% under an illumination with the Am 1.5G spectrum(corresponding to standard test conditions[6]) and a backside reflector. This value is dependent of the sunlight concentration, the maximum value is 40.8% for 46200 times sunlight concentration.

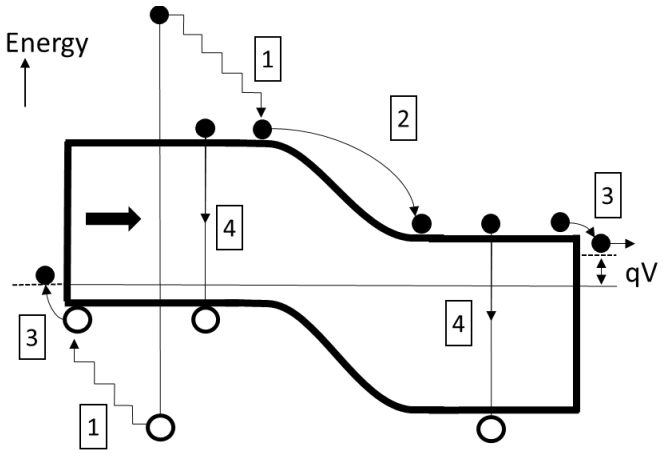

Figure 1.3 Loss processes in standard solar cell: (1) thermalization loss; (2) junction and (3) contact voltage loss; (4) recombination loss.

1.3 First generation

Silicon solar cells are the most widely employed solar cells, since Silicon is one of the most abundant elements on the earth, it possess an indirect band gap of 1.12eV[7] which allows the material to absorb photons in the visible region of light. There are three types of silicon used in the solar cells: single crystalline silicon, multicrystalline silicon, and amorphous silicon. Single crystalline silicon has the highest efficiency at about 28%[8], but is the most expensive amongst the three types. Multicrystalline has a lower efficiency of 24%[9], but is slightly less costly to produce. Amorphous silicon has a much lower efficiency at 16%[3], but it much less expensive to fabricate. Multicrystalline is the most widely commercially used since it low cost and good efficiency. First generation solar cells mainly consist of large area and single layer p-n junction from single crystal silicon.

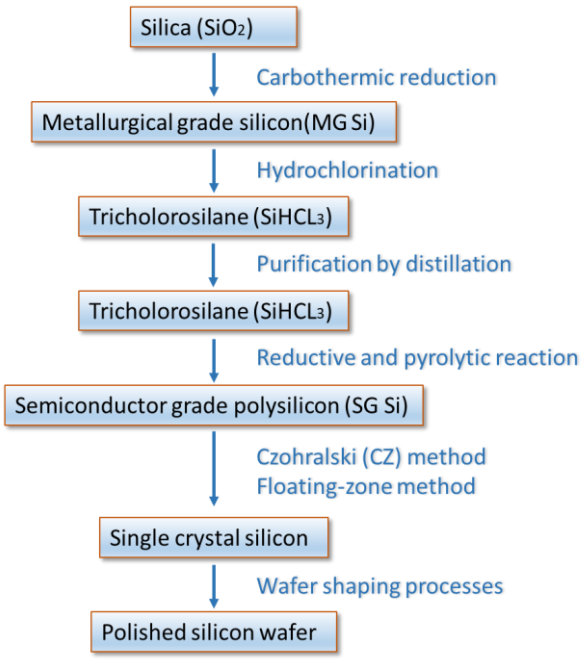

Figure 1.4 Flow diagram for typical silicon preparation processes[10].

The cost of fabricating single crystalline silicon solar cells is due to the purification process required for bulk silicon to turn it into monocrystal silicon, in the Figure 1.4 it is presented a flow diagram for the typical steps and methods for the silicon single-crystal preparation. The starting material for high-purity silicon single crystals is silica (SiO_2). The first step in silicon manufacture is the melting and reduction of silica. This is accomplished by mixing silica and carbon in the form of coal, coke or wood chips and heating the mixture to high temperatures in a submerged electrode arc furnace. This carbothermic reduction of silica produces fused silicon. A complex series of reactions occur in the furnace at temperatures ranging from 1500 to 2000∘C. The lumps of silicon obtained from this process are called metallurgical-grade silicon (MG-Si), and its purity is about 98–99%. The next step is to purify MG-Si to the level of semiconductor-grade silicon (SG-Si), which is used as the starting material for single-crystalline silicon. The basic concept is that powdered MG-Si is reacted with anhydrous HCl to form various chlorosilane compounds in a fluidized-bed reactor. Then the silanes are purified by distillation and chemical vapor deposition (CVD) to form SG-polysilicon. Several intermediate chemical compounds have been considered, such as monosilane

(SiH_4), silicon tetrachloride ($SiCl_4$), trichlorosilane ($SiHCl_3$) and dichlorosilane (SiH_2Cl_2). Among these, trichlorosilane is most used for subsequent polysilicon deposition for different reason such as: It can be easily formed by the reaction of anhydrous hydrogen chloride with MG-Si at reasonably low temperatures (200–400 °C), it is liquid at room temperature, so purification can be accomplished using standard distillation techniques, is easy to handle, store and transport.

Trichlorosilane is synthesized by heating powdered MG-Si at around 300 ºC in a fluidized-bed reactor. That is, MG-Si is converted into $SiHCl_3$, the reaction is highly exothermic and so heat must be removed to maximize the yield of trichlorosilane. While converting MG-Si into $SiHCl_3$, various impurities such as Fe, Al, and B are removed by converting them into their halides ($FeCl_3$, $AlCl_3$, and BCl_3, respectively), and byproducts such as $SiCl_4$ and H_2 are also produced.

The trichlorosilane, which has a low boiling point (31.8 ºC), is fractionally distilled from the impure halides, resulting in greatly increased purity, with an electrically active impurity concentration of less than 1 ppba. The high-purity trichlorosilane is then vaporized, diluted with high-purity hydrogen, and introduced into the deposition reactor. In the reactor, thin silicon rods called slim rods supported by graphite electrodes are available for surface deposition of silicon. In addition, this reaction, the following reaction also occurs during polysilicon deposition, resulting in the formation of silicon tetrachloride. The slim rods are preheated to approximately 400 ºC at the start of the silicon CVD process. This preheating is required to increase the conductivity of high-purity (high-resistance) slim rods sufficiently to allow for resistive heating. Depositing for 200–300 h at around 1100 ºC results in high-purity polysilicon rods of 150–200 mm in diameter. The polysilicon rods are shaped into various forms for subsequent crystal growth processes. Two main techniques have been employed to convert polysilicon into silicon crystals One is a zone-melting method commonly called the floating-zone (FZ) method, and the other is a pulling method traditionally called the Czochralski (CZ) method. In the FZ method, a molten zone is passed through a polysilicon rod to convert it into a single-crystal ingot; in the CZ method, a single crystal is grown by pulling from a melt contained in a quartz crucible. In both cases, the seed crystal plays a very important role in obtaining a single crystal with a desired crystallographic orientation. During FZ crystal growth, the molten silicon does not encounter any substance other than the ambient gas in the growth chamber. Therefore, an FZ silicon crystal is inherently distinguished by its higher purity compared to a CZ crystal which is grown from the melt, involving contact with a quartz crucible. This contact gives rise to high oxygen impurity concentrations of around 10^{18} atoms/cm^3 in CZ crystals, while FZ silicon contains less than 10^{16} atoms/cm^3. This higher purity allows FZ silicon to achieve high resistivities not obtainable using CZ silicon. However, it has been recognized for many years that FZ silicon, which contains fewer oxygen impurities than CZ silicon, is mechanically weaker and more vulnerable to thermal stress during device fabrication. High-temperature processing of silicon wafers during electronic device manufacturing often produces enough thermal stress to generate slip dislocations and warpage. These effects bring about yield loss due to leaky junctions, dielectric defects, and reduced lifetime, as well as reduced photolithographic yields due to the degradation of wafer flatness[10].

Multicrystalline silicon and amorphous silicon are much less pure than the single-crystal silicon which is related to its efficiencies. Amorphous silicon is prepared as a thin film not as a crystal. Multicrystalline silicon is made by pouring molten silicon in a mold and allowing it to cool, this process is called casting. The resulting silicon has no overall lattice structure, but the ingot produced has large column grains of crystals, The incorporation of hydrogen during the process plays an important role in passivating the grain boundaries. This is most conveniently introduced by plasma enhanced chemical vapor deposition (PECVD). The ingot is still sliced and treated as a single-crystal silicon ingot is treated, except that the bottom and top of the ingot are removed before slicing due to poor crystal quality at the edges. Casting method is much cheaper and simple than CZ method.

1.4 Second generation

Photovoltaic cells belonging to this generation are based on the use of thin films. There are three types of thin film cells: amorphous silicon, chalcopyrite compounds particularly copper indium gallium diselenide (CIGS), and cadmium telluride (CdTe). Amorphous Silicon is the most commercially used since the existing Silicon technology can be employed, unfortunately the low efficiency and the photodegradation over time are the main disadvantages.

There are a few fundamental differences between second generation and first-generation solar cell, although they still relay in a p-n junction. The main difference is the material employed in the solar cell; this has a direct band gap contrary to the Si indirect band gap. The substrate is either glass or a flexible web that is made of plastic or from a metal foil. Another advantage of thin film technology is that large glass substrate or continuous webs can be coated. Thin film cells have a top layer called window layer made of a large band gap material that absorbs the higher energy photons and a bottom layer called the absorber layer made from a smaller band gap material which absorbs the lower energy photons than are not absorbed by the window layer.

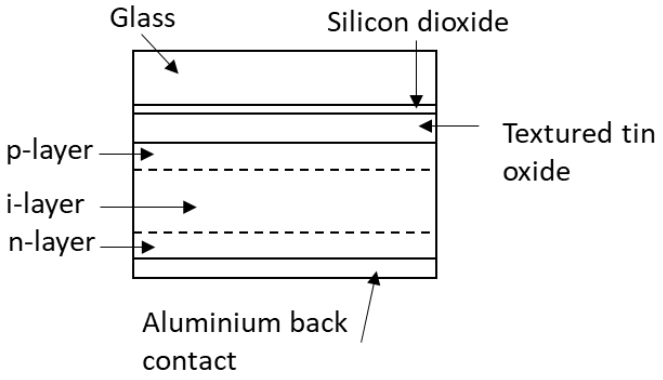

Figure 1.5 Schematic structure of an amorphous silicon single junction solar cell.

1.4.1 Amorphous silicon cells

Thin films of amorphous silicon are produced using chemical vapor deposition (CVD) of gases containing silane (SiH_4), usually PECVD [11] or hot wire CVD. The silicon can be deposited onto both rigid substrates such as glass, and onto flexible substrate, such as metallic sheets and plastics, enabling a variety of use. The material that is employed in solar cells is actually hydrogenated amorphous silicon. The hydrogenated amorphous silicon is found to have a direct optical energy bandgap of 1.7 eV[12] and an optical absorption coefficient $\alpha > 10^5$ cm^{-1} for photons with energies greater than the energy bandgap. This means that only a few microns of material are needed to absorb most of the incident light, reducing material usage and hence cost. Doping has proved to degrade the mobility and lifetime of minority carriers in amorphous silicon. This problem can be reduced if a p-i-n structure is employed as shown in the Figure 1.5. Despite that the initial efficiency of the cells in the laboratory can be superior to 12%, commercial modules when exposed to sunlight over a period of months degrade the cell to an efficiency value around 5%. This phenomenon is called Staebler-Wronski effect[11].

1.4.2 CdTe cells

In 1956 Loferski proved that the optimum energy bandgap for solar cell is around 1.5eV[13]. Since CdTe has a direct bandgap of 1.45 eV along with high optical absorption, it makes it a suitable material for solar cells. It was realized that a few microns were enough to absorb most of the incident light, minimizing material costs. The firsts thin film solar cells that were fabricated employed CdTe/Cu_2Te[14]. These materials were found to be unstable, due to the Cu_2Te layer. To avoid this CdS was employed, it`s energy bandgap of 2.42 eV makes suitable to transmit most of the solar spectrum. The substrate employed in this type of solar cells is typically soda lime glass coated with a thin conductive layer of tin Oxide or indium tin oxide. A thin film of CdS is deposited on the glass using chemical bath deposition (CBD), The CdTe layer can be deposited using several methods such as closed-space sublimation (CSS), physical vapor deposition (PVD), electrodeposition, atomic layer epitaxy, sputtering and spray pyrolysis, all these methods require temperatures greater than 400 ºC to ensure crystal quality. The highest efficiency CdTe-based solar cell produced to date have reached 22%[9].

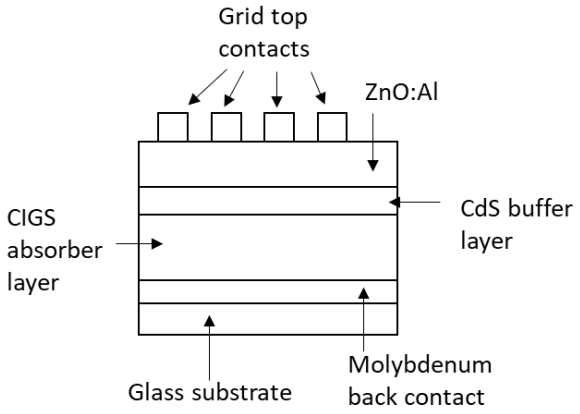

Figure 1.6 Scheme of a substrate configuration chalcopyrite device structure.

1.4.3 Chalcopyrite cells

Chalcopyrite materials possess a direct band gap that is widely tunable depending on the ratio of its elements, ranging from 1.0 eV to 1.7 eV. The CIGS material is the absorber layer and CdS is employed as the window layer for the same reasons as in CdTe cells. It should be noted that adding too much gallium results in the layers being too highly resistive for use in solar cell structures. An energy bandgap of 1.25 eV corresponds to the maximum widening achievable without loss of efficiency and hence most of the CIGS cell focus on that energy. Another chalcopyrite material with 1.5 eV direct energy band gap is cupper indium disulphide ($CuInSe_2$). The most employed methods to produce chalcopyrite materials are co-evaporation of elements, selenisation/sulphidisation of elemental precursor layers, and stacked elemental layer (SEL). Most of these photovoltaic devices are usually deposited in the substrate configuration i.e., back contact, absorber layer, buffer layer, transparent conductive oxide (TCO) and then a top contact grid. The back contact normally is molybdenum, the buffer layer is CdS and the TCO, Al-doped ZnO as shown in the Figure 1.6.

The passivation of grain boundaries and other surfaces in chalcopyrite semiconductors is attributed to the presence of sodium ions and oxygen from air annealing[11]. The sodium may diffuse into the absorber layer from the soda lime glass substrate, it is also common to introduce them directly into the layer by adding an inorganic source of the ions to the material to be evaporated or sputtered.

1.4.4 Health hazards

To produce thin film devices, a variety of chemicals and materials are employed. The types and the amounts of chemicals depend on the type of technology and the type of cell fabricated, also it depends on the manufacturer. Some of these chemicals includes acids and corrosive liquids such as: sulfuric acid, hydrochloric acid, hydrogen fluoride and nitric acid are normally employed in the wafer cleaning for crystal silicon. Many hazardous materials as well as explosive and toxic gases are involved in the manufacturing processes of thin film photovoltaic cells. Some of these chemicals can be toxic or harmful to the humankind. Not only the potential threat to health exists, also if it constitutes a real problem in the environment. The primary subjects exposed to the chemicals and its residues are the workers involved in its production, in the form of inhalation of vapor or dusts and via direct contact if spills occur. Another option could be accidental ingestion. The ones outside a manufacturing environment could be infected by chemicals via inhalation from stack emissions, elusive air emissions or from accidental release after fire or explosion. There is also the possibility of pollution to the environment, for example, at the surroundings of spent photovoltaics modules, groundwater seepage[15].

In the case of CdTe manufacturing, occupational health risk is associated with the toxicity of CdTe and cadmium Chloride ($CdCl_2$). Since cadmium compounds are usually used in powder and in liquid form, inhalation of cadmium vapors or dust and ingestion of spills is a concern. In the case of inhalation of small particles of cadmium, the risk of lung cancer is present. Long term exposure can have harmful effects on bones and kidneys[15]. Inhalation of cadmium containing vapors can result in metal vapor fever, pneumonitis, pulmonary edema, and finally death. CdTe and CdS thin films are solid, at ambient conditions, the vapor pressure is zero, which means, that is not possible to release vapor or dust. Even in residential fires 800 ºC to 1000 ºC there is no risk of evaporation since the melting point for the CdTe and CdS are 1041 ºC and 1750 ºC, respectively.

For the amorphous silicon solar cells, the main risk is related to the extremely pyrophoric properties of the Silane gas (SiH_4) which is used as precursor during the PECVD technique, It can ignite even for low concentrations of 2%. Hydrogen employed on amorphous silicon is explosive and flammable, therefore, it requires to be handled safely. The doping gases for the amorphous silicon such as: arsine, phosphine and germane are toxic, in case of leakage constitute a hazard to the health.

For CIGS solar cells a very thin film of CdS is deposited and acts as buffer layer. Although CIGS solar cells freed of toxic CdS have been successfully produced[16]. The toxicity of Cu, In, Ga and selenium are considered benign and Se is part of human nutrition. Although elemental selenium is moderated toxic, hydrogen selenide which is used in the fabrication of CIGS solar cells is highly toxic and is dangerous to life[17]. Some studies have shown that CIS and CGS have mild systemic toxicity[18].

1.5 Third generation

Third generation solar cells surge with the objective of reducing costs compared to the first generation and due to the toxicity and limited number of materials of the second generation. This type of photovoltaics devices does not rely on the p-n junction design from the previous generations. For example, organic solar cells and Dye-sensitized solar cells.

1.5.1 Organic solar cells

Organic solar cells are classified like this because the active layers of the cell are fabricated with organic materials. Molecular materials show semiconducting properties when they are constructed so that the carbon atoms present in the molecule or polymer chain are bonded as $sp^2 + p_z$ hybrid orbitals. Photo absorption in these materials creates an excited state which is generally confined to a molecule or a region of a polymer chain, this can be considered as an electron-hole pair, bound together by coulomb and lattice interactions[11]. The organic cells normally have a double layer or a distributed heterojunction structure. Double layer cell has two organic semiconductor layers in contact, sandwiched between co-planar electrodes and the dispersed heterojunction cell is made from a mixture of organic semiconductors between co-planar electrodes as shown in the Figure 1.7. In organic solar cells the active layer is formed by donor and acceptor materials for charge separation and transportation. The cost of production for these materials is a significant advantage compare with regular semiconductors. Organic cells can be fabricated on plastic sheets as substrate obtaining a flexible solar cell. Organic solar cells still have low efficiency, many organic photoconductors are known to be sensitive to oxygen, which may lead to degradation of the material. The highest efficiency achieved for organic cells is 18%[9].

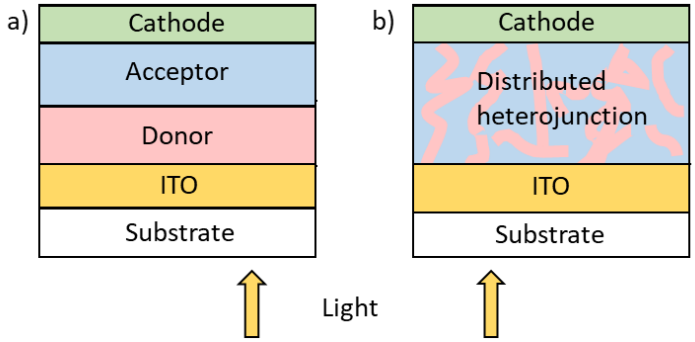

Figure 1.7 Schematic of the basic structure of a) double layer organic cell and b) distributed heterojunction.

1.5.2 Dye-sensitized solar cells

Dye-sensitized solar cells (DSSC) or Grätzel cells, were originally co-invented in 1988 by Brian O`Regan and Michael Grätzel[19]. In this type of solar cells, the process of light absorption and carrier transportation are separated. The light is absorbed by a sensitizer, which is anchored to the surface of a wide band semiconductor. Charge separation takes place at the interface via photon induced electron injection from the dye into the conduction band of the semiconductor to the charge collector. The employ of sensitizers having a broad absorption band in conjunction with oxide films of nanocrystalline morphology permits to harvest a large fraction of sunlight. Within the system is a mesoporous oxide layer composed of nanometer sized particles which have been sintered together to allow for electronic conduction to take place. Normal wide band gap materials are TiO_2, ZnO, and Nb_2O_3[20]. Attached to the surface of the nanocrystalline film is a monolayer of the charge transfer dye. Photoexcitation of the latter results in the injection of an electron into the conduction band of the oxide. The original state of the dye is next restored by an electron donation from the electrolyte. This type of solar cell have achieved a maximum efficiency of 12%[21].

1.5.3 Perovskite solar cell

A perovskite structure is a compound that possess the same structure as the perovskite mineral of the form $CaTiO_3$. Perovskite materials have a crystallographic family with the general ABX_3 stoichiometry with A and B cations and X an anion that bounds with both cations, the ideal cubic structure has the B cation in a 6-fold coordination, surrounded by an octahedron of anions as shown in the Figure 1.8 . These are low cost and easily synthesize material.

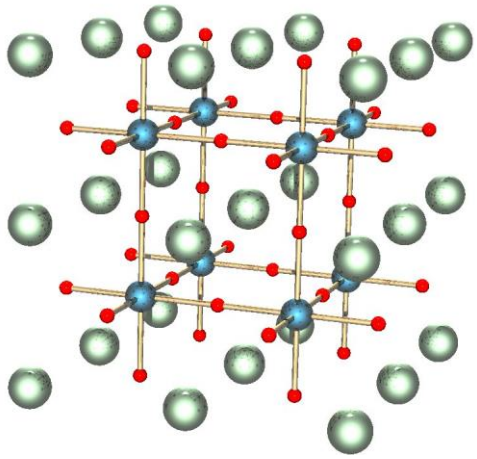

Figure 1.8 Perovskite cubic structure, red atoms represent the anions.

Perovskite solar cell is form basically by the perovskite photoactive film sandwiched between two electrodes. Inter facial buffer layers are often employed between the active later and the electrodes to facilitate the charge transport processes. There are two types of inter facial layers namely electron transport materials (ETM) and hole transport materials (HTM) which can be organic or inorganic. In principle one of the electrodes must be TCO such as indium or fluorine-doped tin oxide (ITO or FTO), in some cases, aluminum doped zinc oxide (AZO). The top electrode could be aluminum, silver, or gold. P-i-n or n-i-p structures are employed on perovskite solar cells. Depending on if the device contains mesoporous medium or not it is called mesoporous or planar structure, respectively. The processes of charge generation and collection in perovskite cell are not well understood due to the complex nature of the medium. The principles of p-n junctions are still applicable, however, studies on the charge transport dynamics suggest that the electron-hole pairs are generated immediately after photon excitation in the perovskite medium and then dissociated into free charge carriers in less than 2ps[22], [23] by the built-in electric field caused by the work function difference between the anode and the cathode. The main advantage of the perovskite material as absorber is the long char diffusion length and high carrier mobilities, diffusion lengths can reach as high as 1µm. two main type of structures are employed: mesoporous and planar structures. In mesoporous structures, the perovskite layers are formed on porous semiconductor metal-oxide (TiO_2) medium which create interpenetrating network between the two phases, which makes that the photogenerated electrons can be transported from the TiO_2 to the cathode while the holes are transported to the anode. In the planar structure, the devices are fabricated using interfacial buffer layers ETM and HTM through which the photo generated charges can be driven to the electrodes by the influence of either built in potential or external applied field. The efficiency of the perovskite solar cell depends on the quality of the morphology of the

perovskite material, formation of Ohmic contacts between the active layer and ETM/HTM layers, and the band gap of the perovskite film, been 1.2-1.6 eV the ideal range.

The main compounds employed in the ABX_3 perovskite structure are for A, the organic molecule ($CH_3NH_3^+ \; or \; NH_2CHNH_2^+$), for B a divalent metal($Pb \; or \; Sn$) and for X a halide ($Cl, br \; or \; I$)[24]. Highest efficiency on perovskite solar cell have reached 25%[25] in very short time although there are still some disadvantages like its poor reproducibility which affects directly the efficiency. A big issue is the toxicity, PbI which can be employed in the perovskite material is known for been toxic. Also, Pb the employment of Pb is something that should be resolved.

1.5.4 Multijunction cell

The multijunction cell or tandem cell, as the name suggest is formed by at least two cells with different band gaps. This allows the absorption of a narrower range of photon energies which is one of the main processes of efficiency loss. If the cells are stacked one over another with the highest band gap cell at the top, we can achieve the energy loss due to the filtering of the photon energy that is produced. The efficiency of the tandem cell increase as the number of cell increases, it has been calculated that for 2,3 and an infinite number of cells with under concentrated sunlight, the efficiency can reach 55%, 63% and 86%, respectively[26]. The cells are usually designed to be connected in series, this means that the cells should produce a similar amount of current, if a cell produce a less than 5% of the neighbor cell, then it will consume power instead of producing it, the best that can be done for the performance of the device is to short-circuit the low output cell, a by-pass diode that limits this consumed power is the most practical way to achieving it.

For the third generation of photovoltaics, different materials have been researched. III–V compound materials are commonly used in photovoltaic devices with higher efficiencies[27]–[30]. The highest performance in solar cells have been achieved by monocrystal III-V multijunction solar cells, reaching 47%[30]. This type of solar cells requires a high crystal quality to reach high efficiencies, so they are normally fabricated by Metal Organic Vapour Phase Epitaxy (MOVPE) and Molecular Beam Epitaxy (MBE). These epitaxial growth techniques ensure high crystal quality and III-V materials allows a wide variety of band gap energies. However epitaxial techniques requires that materials lattice matched to the employed substrate. Examples of these compounds are gallium arsenide (GaAs), indium phosphide (InP), gallium antimonide (GaSb), Aluminum arsenide (AlAs), etc., in the Figure 1.9 different materials with its lattice constant and band gap values are shown. Double and triple junction cells based on GaInP/GaAs/Ge systems have been developed for extraterrestrial purpose with efficiencies around 30% under terrestrial sunlight[31]. A six-junction cell with 47% efficiency employed an AlGaInP/AlGaAs/GaAs/GaInAsx3 structure[30]. Due to the deeply researched Si technology, low cost compared to III-V materials, viable incorporation of III-V-N compounds and materials properties such as hardness, mechanical integrity and thermal conductivity, tandem cells with a Si substrate are a promising research field.

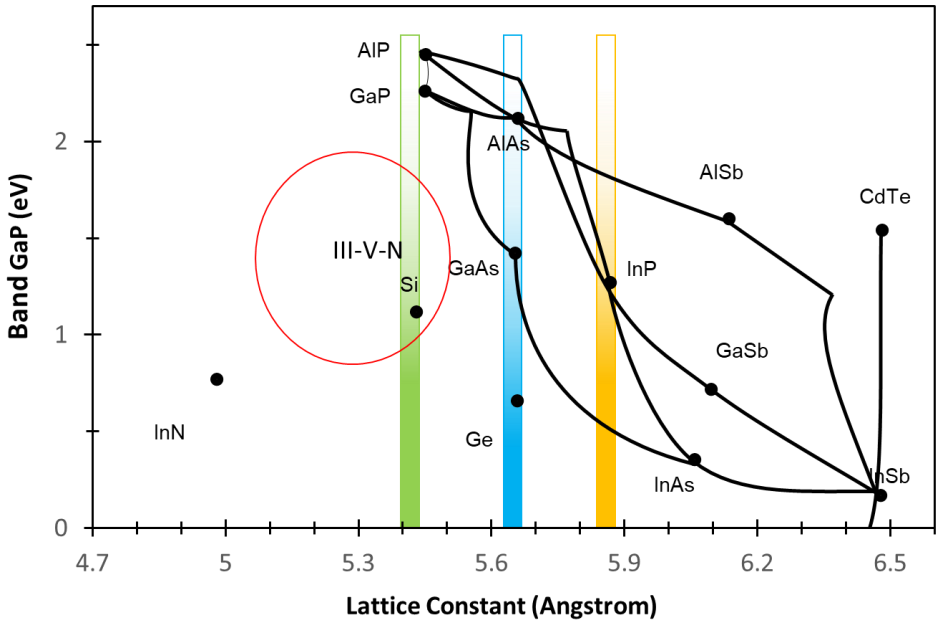

Figure 1.9 Band gap energy of semiconductors over lattice constants. Some nitride materials extend the range of material combinations significantly. Lattice matched heterostructures such as multi-junction solar cells can be grown on gallium arsenide, germanium (marked blue) and InP (marked yellow), while heterostructures on silicon (marked green) allows the application of dilute nitrides.

Other III-V tandem cells employ metamorphic growth allowing more flexibility of the materials combinations and better matching to the solar spectrum. Even when crystal quality is degraded due to dislocations , the metamorphic triple-junction GaInP/GaInAs/Ge cell has reached 40.7%[32], being the first device to exceed 40% efficiency. However, even with this flexibility it is still limited by the strain accumulated in the lattice which interferes with higher efficiencies. The development of direct wafer bonding technology has allowed the combination of mismatched materials through a permanent, electrically conductive, and optically transparent interface. The four-junction cell GaInP/GaAs/GaInAsP/GaInAs combines both the wafer bonding and the metamorphic growth reaching an efficiency of 44.7%, in this case the top cell was grown on GaAs substrate and bonded to the bottom cell grown on InP substrate[33].

1.5.5 Multiband solar cells

Another concept that can improve the efficiency of a solar cell, is by introducing multiple mini bands in the absorption material the absorption of photons with multiple energies that cannot be absorbed in a normal single junction cell. A solar cell with an intermediate band with energies between the valence and conduction band is called intermediate band solar cell (IBSC). This type of solar cell has the potential to surpass the efficiency of a normal cell by increasing the photocurrent via the absorption of band gap photons without degrading the voltage. In the Figure 1.10 we can observe how the absorption of an electron labelled as 1 allows the transition of an electron from the valence band to the intermediate band, and the absorption of a photon 2 allows the transition of an electron from the intermediate band to the conduction band. This two- step transition adds to the usual transition 3 from the valence band to the conduction band. The introduction of the intermediate band is creating 3 minibands in the absorption layer.

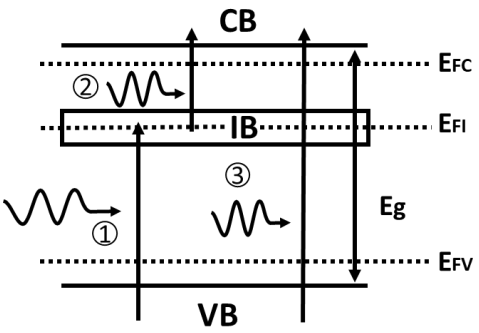

Figure 1.10 Band diagram illustration of the IBSC principle. IB is the intermediate band, CB the conduction band, VB the valence band. E_{FC}, E_{FI} and E_{FV} are the quasi-Fermi levels for electrons in the three bands[34].

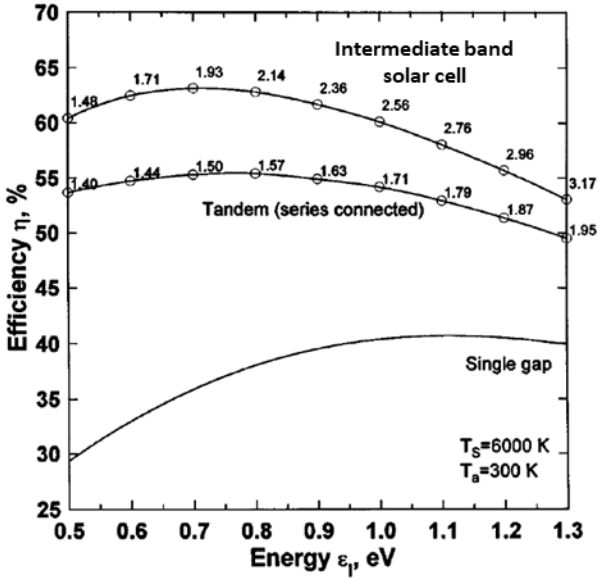

Figure 1.11 Calculated efficiency limits as a function of the lowest band gap for the Intermediate band, and two-terminal ideal tandem cell, vs the lowest band gap ε_l, and for a single band gap cell. The corresponding values of the highest band gap in cell are presented for maximum efficiency[35].

The intermediate band is electrically isolated from the external contacts so that no current can be extracted from the band. Antonio Luque and A. Marti probed, assuming that any irreversible mechanism is prevented, in particular, non-radiative transitions between any two of the three bands are forbidden, carrier mobilities are infinite and Ohmic contacts are applied so that only electrons, no holes can be extracted, the maximum possible efficiency of this type of cell with an $E_g = 1.93eV$ and $\varepsilon_l = 0.7eV$ (ε_i the lowest band gap), could reach 63.1% which is higher than the one from a single gap cell and the tandem cell[35] as shown in the Figure 1.11.

There are two main approaches to achieve the intermediate band in the solar cell, one is by introducing impurities in the absorption layer and the other is by introducing Quantum Dots (QD)s.

Deep center levels in the band gap were the first system suggested to study interband behavior. This approach requires adding impurities to the semiconductor with energy levels close to the middle of the

bandgap. However, in this situation Shockley-Read-Hall recombination is enhanced[36] and electron wavefunctions need to be delocalized forming a miniband for inhibiting non-radiative recombination[37]. Lifetime measurements on Ti and S implanted silicon wafers support this theory. However, the band anti-crossing (BAC) model concept provides a better alternative for forming an intermediate band in highly mismatched alloy materials. By adding N or O in the semiconductor lattice a band is formed inside the gap, as described by the BAC model. This band is the result of the interaction between the localized states of the N and O atoms mixing with the CB states and it has shown IB behavior. For example, in GaNAs electronic transitions from IB to CB has been identified[38], and in n-doped GaNPAs layers photoreflectance measurements show IB absorption[39] , while and Voc has been improved in ZnTe solar cells and ZnTeO IBSCs using n-ZnS window layer[40].

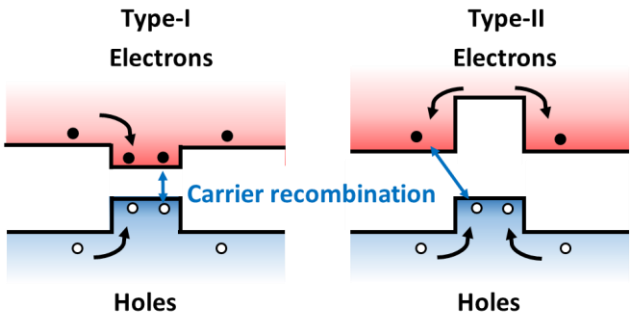

Figure 1.12 Energy band diagrams for a type-I and type-II alignment, carrier spatial separation due to the type-II alignment reduce the carrier recombination compared to type-I alignment.

QDs for intermediate band cells is the most studied approach. Although there are some limitations that needs to be surpassed for successful fabrication of IBSC. One problem is that the intermediate band is formed from the confined states from the QDs which are not effectively decoupled from CB or VB. The most studied system for IBSC is the type-I In (Ga)As/GaAs QD grown by the Stranski-Krastanov method. However, with this type of QD`s in solar cells, thermal excitation causes a carrier extraction from the QDs and a reduction in the carrier lifetime at the intermediate band because of the small confinement, which prevents the two-step photon absorption. On the other hand, the type II QDs exhibit better qualities. The type II possess a staggered confinement potential and results in spatial separation between electrons and holes in the QD, this spatial separation reduces the carrier recombination which also increase the lifetime of the carriers[41] as shown in Figure 1.12. This increase in the carrier lifetime is an improvement for a solar cell.

1.5.6 Carrier recombination reduction in III-V solar cells

An interesting solution to suppress the carrier recombination was proposed by Tanoue and Sakaki[42]. They introduced a multilayered heterostructure with type-II band alignment. For two materials A and B, when the electron affinities χ_A, χ_B and the energy gaps E_{gA}, E_{gB} satisfy the conditions $\chi_A > \chi_B$ and $E_{gA} + \chi_A > E_{gB} + \chi_B$, the photo-excited carriers could be spatially separated from the band edge discontinuities between the two materials of the heterostructure. They applied this scheme to avalanche photodiodes, when an electric field along the layer plane accelerates carriers to higher energy states (1), some energetic carriers may cause impact ionization in layers A and B (2). As carriers as initially separated,

electrons will see a band gap E_{gA} and holes E_{gB}. Since the impact ionization is easier to take place in narrower gap materials (E_{gA}), the initial ionization process 2 is expected to occur dominantly in layer A. Electrons in layer A will repeat the avalanching process (3). Holes produced in layer A by the impact ionization, will be accelerated to layer A or push into layer B. If the thickness of layer A is small enough such transfer process of holes across the layer boundary will be very efficient, causing that the majority of holes fall in B. This concept may also be useful in solar cells because the carrier recombination can be suppressed, increasing the carrier lifetime.

1.6 Prospect materials

The implementation of any photovoltaic technology relays in the balance between the production/installation cost and the energy obtention, which depends on its lifetime and conversion efficiency. As the more developed a technology becomes, less expensive results to increase the installed capacity by an additional watt[43]. Since the Si based photovoltaics is the most studied, it shows the lowest production cost. In comparison with silicon-based photovoltaics, thin film systems require less material per surface, avoiding also costly purification process. As a result, despite a much smaller volume fabricated, thin films solar cells can compete in terms of cost per Watt. In Figure 1.13 the three generations are summarized in terms of cost per Watt and efficiency.

III-V tandem cells have obtained the highest efficiencies. However, III–V substrates are expensive, increasing the production cost of these high-performance cells. The use of standard Si substrates would reduce the cost of high efficiency multijunction solar cells. To overcome this issue, a combination of III–V compounds and Si substrates can be used. Gallium phosphide (GaP) can be an excellent alternative for the integration of III–V materials and Si substrates owing to its low lattice mismatch with Si as shown on Figure 1.9. In particular, GaAsPN alloys have a large tunable band gap in the range 1.5–2 eV under Si lattice-matching conditions[44]. Potential solar cells with III–V–N materials grown on Si have been proposed with high theoretical efficiencies. For example, double-junction solar cells exhibit theoretical efficiencies over 36% and triple-junction over 44%[45], [46]. This makes the III-V-N materials very promising for solar cell fabrication.

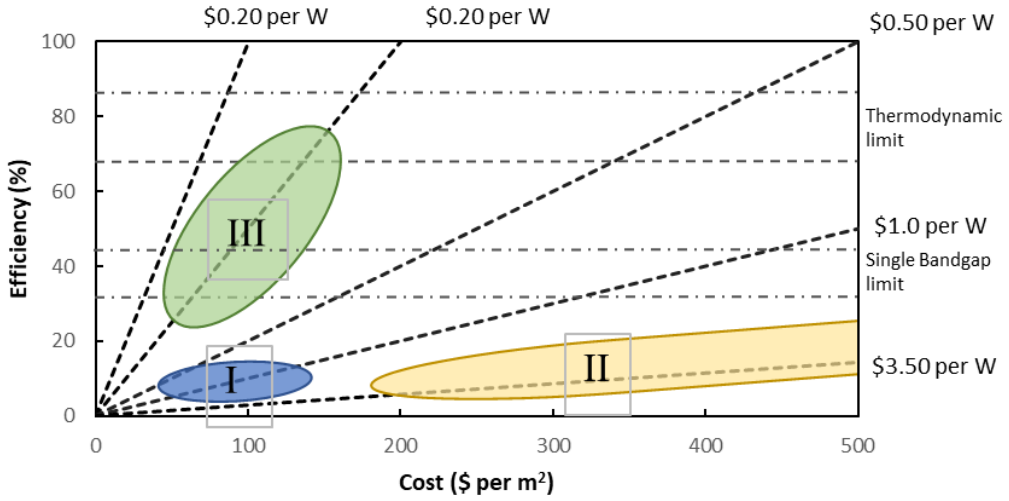

Figure 1.13 Efficiency and cost projections for first- (I), second- (II), and third generation (III) PV technologies.

Despite these advantages, III–V–N growth on Si is complicated owing to the generation of structural defects, such as threading dislocations, stacking faults, and antiphase domains, at III–V/Si interface[47]. To achieve high-quality crystals of III–V–N materials, a high-quality GaP heteroepitaxy can be implemented on Si[48], [49]. Thus, along with optimization of growth conditions, understanding GaP epitaxy is essential because the influence of initial GaP/Si heteroepitaxy is a critical step in the integration of III–V–N materials and Si substrates[50]–[53].

Despite many efforts on growth and device fabrication, the conversion efficiency of current III–V–N photovoltaics is still low[54]. Even in a dislocation-free structure, carrier recombination occurs because of point defects in the III–V–N layer. N–N, N-As split interstitials, and N-interstitials are the major point defects, and they act as carrier scattering centers, resulting in the diffusion length shortening of photo-excited carriers.

1.7 Objectives and Organization of thesis

The main objective is contributing to the fabrication of a functional GaAsPN based solar cell on Si substrates. To achieve that two issues will be addressed. First is the free defect heteroepitaxy of GaP/Si. To help to clarify the growth mechanism and enhance defect annihilation, the diffusion process of the GaP growth will be studied by the estimation of the diffusion lengths, with this the growth conditions that increase the annihilation of antiphase domains will be mentioned. The second issue is the carrier recombination loss in solar cells. To reduce this type of losses the implementation of an array of stacked type-II QDs embedded in the absorption layer is proposed. To achieve this, is necessary the successful low defect InP QD stacking in the GaAsPN matrix. Due to the lack of information concerning to this family of materials, as a first approach, the study of growth conditions and vertical stacking of InP QDs on GaP will be studied.

In the First chapter, I mention the motivation for this work as some precedents.

In the second chapter the fundamental concepts aborded in this work are mentioned as the calculated type-II band alignment for a InP QDs embedded in a GaAsPN matrix, in the third chapter the basics of the characterization techniques employed are mentioned.

In the chapter 4 the diffusion lengths measurement is presented, starting with the theory need for the estimation, after that the experimental method is described, and the results are presented followed by discussion of the results.

In the chapter 5, I start investigating the ideal growth conditions for the InP homoepitaxy, once obtained I proceed to achieve the formation of InP QDs on GaP substrates. The growth parameters and its dependence on the QD size is discussed. Followed by the stacking conditions of multiple layers of InP QDs. Finally, the optimization of all the conditions is applied to a 30-layer stacking array. A two-step growth interruption process is employed to reduce the formation of defects.

The chapter 6 consists of summarizing the results, conclusions of the presented work and future work topics.

Chapter 2 Background

2.1 Molecular Beam Epitaxy

Most of the semiconductor compounds currently used are almost always monocrystals materials. Of the great variety of growth techniques, Molecular Beam Epitaxy (MBE) and metalorganic vapor phase epitaxy (MOVPE) are the most employed multi-purpose techniques for heteroepitaxial research and commercial production. Due to the ultra-high vacuum (UHV) conditions which make it compatible with UHV characterization techniques and the precise growth control makes it one the most powerful tools for monocrystal growth.

Molecular Beam Epitaxy is a technique that it distinguishes from other evaporation techniques due to a much accurate atomic or molecular beams and for the UHV conditions, Alfre Y. Cho and John Arthur created the MBE technique in the late 60`s[55]. The MBE technique is capable of produce high quality films with abrupt interfaces and an excellent thickness control and composition.

Oil-free pumping is used to eliminate the possibility of contamination by hydrocarbon back streaming, typically rough pumping is made by sorption pumps and for UHV pumping cryogenic sorption pumps, titanium sublimation ion pumps, and turbomolecular pumps are normally used. Turbomolecular pumps can be used if they are provided by a suitable cold trap. A two or three stage substrate entry load-lock and preparation chamber isolated by gate valves are employed to minimize the system exposure to air. The growth chamber is surrounded by a large liquid nitrogen cooled cryopanel with the objective that the heated substrate is not directly exposed to thermal sources other than the molecular beams. The cryopanel also reduces contamination arising from outgassing from the walls of the chamber that are exposed to radiation from the effusion cells.

Because the MBE takes place in a UHV environment (pressure $\leq 10^{-10}$torr), it is possible to employ different in situ characterization tools such as Reflection of High Energy Electrons (RHEED), Auger electron spectroscopy, ellipsometry spectroscopy, Secondary Ion Mass Spectrometry, X-ray Photoelectron Spectroscopy, Scanning Electron Microscopy, etc. Particularly RHEED provides immediate feedback which improves the growth control.

In MBE reactor materials are deposited from molecular beams of the precursor materials introduced via gas-source cells normally arranged radially in front of a heated substrate holder which rotates to ensure temperature uniformity. The need to rotate the substrate to give uniformity also leads to complications in substrate-temperature measurement. The substrate is heated by radiation from a set of resistively heated tantalum foils behind the substrate holder, and both the heater and the thermocouple are stationary. Without direct contact between the thermocouple and the wafer, the indicated thermocouple temperature will be very different from the actual substrate temperature. Temperature calibration can be made by a pyrometer. In Figure 2.1 it is shown the basics elements of an MBE growth chamber. The simplest source cells are thermal evaporators called effusion cells or Knudsen cells. Typically, the effusion cells are made of pyrolytic boron nitride with tantalum heat shields. The source temperatures are maintained precisely (±0.1 °C) to control the flux of evaporation atoms. Due to the inability to rapidly ramp up or down the cell temperature, a shutter is used to turn each beam on and off. The source cells supply all atoms necessary for the growth and doping of the required semiconductor layers. A basic requirement for MBE growth is line of sight source impingement. This means that the evaporated source atoms must have mean free paths greater than the source to substrate distance, which usually goes from 5 to 30 cm.

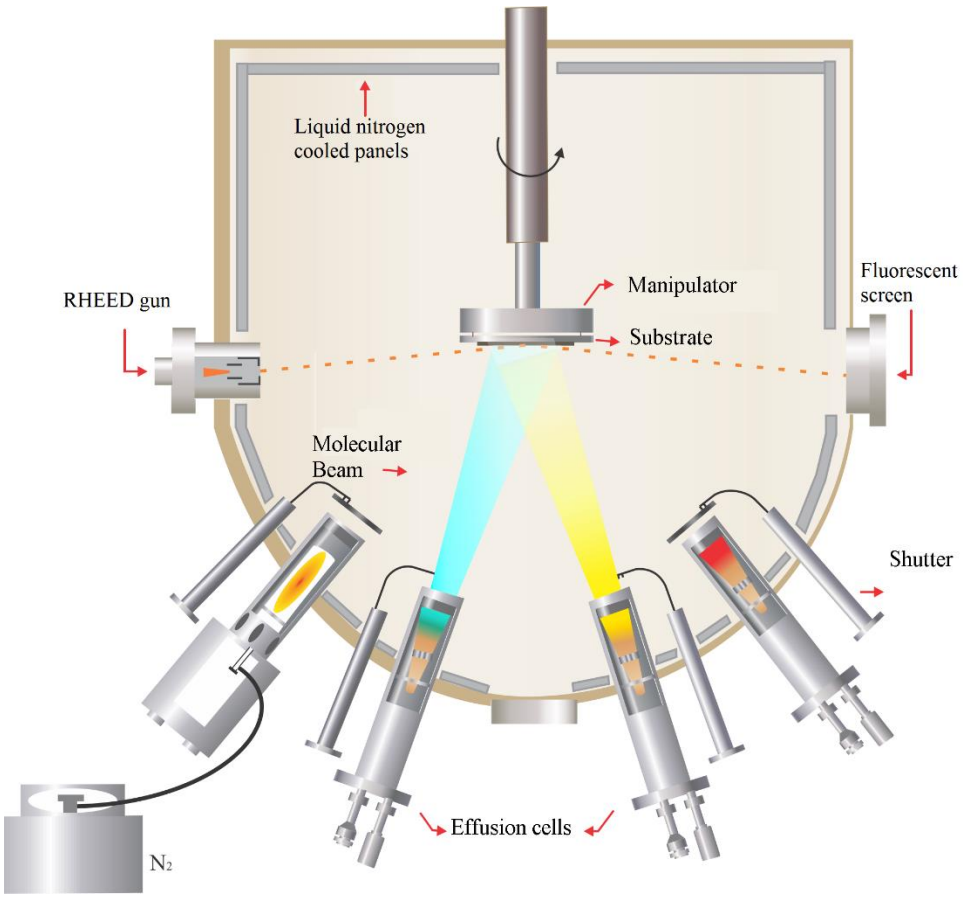

Figure 2.1 Schematic image of an MBE growth chamber, showing the effusion cells and shutters, the substrate holder, and the RHEED arrangement system.

The mean free path for an evaporated particle may be estimated if it is assumed that all other particles in the system are at rest. Supposing that a particle is moving at a c velocity, and all particles have a round cross section with diameter σ. Two particles that pass at σ or lees will collide. Therefore, each particle can be considered to have a collision cross section of $\pi\sigma^2$, and the collision volume swept out by a particle in time dt is $\pi\sigma^2 cdt$. If N is the volume concentration of particles, then the collision frequency will be.

$$f = N\pi\sigma^2 cdt \tag{2.1}$$

And the mean free path will be.

$$\lambda = \frac{c}{f} = (N\pi\sigma^2)^{-1} \tag{2.2}$$

A more accurate calculation of the mean free path may be made assuming that all the particles are in motion. Based on this, the mean free path for an evaporated particle is

$$\lambda = \left(N\pi\sigma^2\sqrt{2}\right)^{-1} = \frac{kt}{P\pi\sigma^2\sqrt{2}} \tag{2.3}$$

With P the pressure.

Typical values of the cross-section diameter σ range from 2 to 5 Angstroms, so that the mean free path is about 10m at a pressure of 10^{-5} torr. This pressure therefore represents an approximate upper limit for the system pressure during growth. To achieve this pressure conditions during growth, the chamber walls must be cooled to cryogenic temperatures by means of liquid nitrogen shroud, to reduce evaporation from this large surface area.

The flux of atoms from such effusion cell may be calculated using the kinetic theory of gases[56]. From this it is obtained that the evaporation rate from a surface area A_e is given by

$$\frac{dN_e}{dt} = \frac{A_e P}{\sqrt{2\pi kTm}} \tag{2.4}$$

Where P is the equilibrium vapor pressure of the source at the effusion cell temperature T and m is the mass of the evaporant. In terms of the molecular weight of the species, M, the effusion rate is.

$$\frac{dN_e}{dt} = \frac{A_e P}{\sqrt{2\pi kTM/N_A}} \tag{2.5}$$

Where N_A is the Avogadro's number. Simplifying,

$$\frac{dN_e}{dt} = 3.51 \times 10^{22} \frac{A_e P}{\sqrt{MT}} molecules/s \tag{2.6}$$

Where P is the pressure in torr. Because the equilibrium vapor pressure P varies exponentially with temperature, the effusion cell temperature must be controlled to within ±0.1 °c to keep effusion rate within a ±1% tolerance.

The flux of evaporant arriving at the substrate surface can be calculated from the evaporation rate at the effusion cell by

$$j = \frac{\cos\theta}{\pi l^2}\frac{dN_e}{dt} = 1.117 \times 10^{22} \frac{A_e P \cos\theta}{l^2\sqrt{MT}} molecules\ cm^{-2}s^{-1} \tag{2.7}$$

Where l is the distance from the effusion cell to the substrate and θ is the angle between the beam axis and the normal to the substrate.

The substrate-preparation techniques used prior to MBE growth are very important, as impurities on the surface provide nucleation sites for defects. Various chemical clean and etch processes are used, there is also the option of employing epi-ready substrates, with a volatile oxide film on the surface that protects the surface from contamination and can be thermally removed within the UHV chamber.

2.2 Growth process

During the growth of III-V materials by MBE, the atomic beams impinge on the substrate surface, and bound with the atoms on the surface. For low temperatures all the incident group III atoms stick on the substrate and only the enough group V atoms adhere to satisfy the stoichiometric growth. Above the congruent evaporation temperature III-V compounds are unstable. Group V atoms are preferentially desorbed above the congruent sublimation temperature, at higher temperatures evaporation of group III atoms become significant. The excess of group V atoms species are desorbed, to preserve the stoichiometric growth it is necessary only to supply group V atoms in excess. The growth rate depends entirely on the net group III flux.

The GaAs is the most studied compound by MBE growth, due to the similar crystal structure to GaP it is expected to have a similar growth mechanism. The model for the GaAs growth is based on the work of Foxon and Joyce[57], [58]. In the growth on GaAs (100), GaAs is formed by the evaporation of elemental, atomic, Ga and the sublimation of elemental arsenic which can either be dimeric (As_2) or tetrameric (As_4). When GaAs is grown from Ga and dimetric As [Figure 2.2 (a)] the reaction is one of dissociative chemisorption of As_2 molecules on single Ga atoms. The sticking coefficient of As_2 is proportional to the Ga flux (a first order process). Excess As_2 is reevaporated, leading to the growth of stoichiometric GaAs. For GaAs grown from Ga and tetrameric As [Figure 2.2 (b)], the process is different. Pairs of As_4 molecules react on adjacent Ga sites, Even when excess Ga is present there is a desorbed As_4 flux. The maximum sticking coefficient for As_4 is 0.5 For very low As/Ga flux ratios, when the As_4 surface population is small compared to the number of Ga sites, the growth rate-limiting step is the encounter and reaction probability between As_4 molecules (second order process). When the As_4 flux I bigger than the Ga flux and there is a high probability that arriving As_4 find adjacent sites occupied by other As_4 molecules and the desorption rate becomes proportional to the number of molecules being supplied. Growth thus proceeds by adsorption and desorption of As_4 via bimolecular interaction resulting in one As atom sticking for each Ga atom. As the growth temperature is increased As_2 is lost by desorption resulting in an increased Ga surface population.

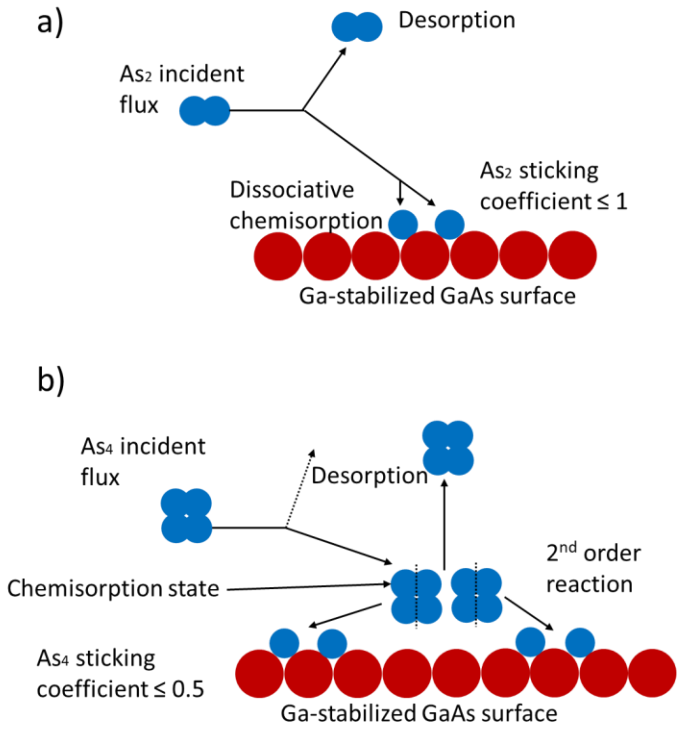

Figure 2.2 GaAs growth model by MBE for a) dimeric As and b) tetrameric As.

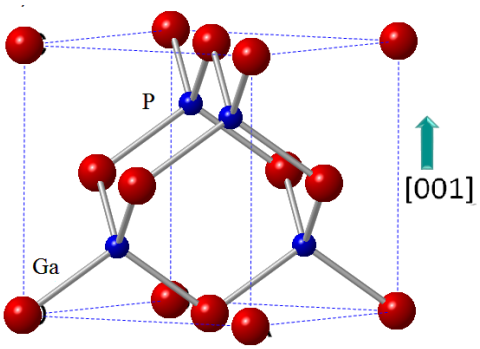

Figure 2.3 Image of the zinc-blende structure, Ga and P atoms are represented by the colors red and blue, respectively.

2.3 GaP crystal structure

Atoms in crystals are located at energetically most favorable sites. The locations depend on the characteristics of the atoms, such as their size and their electric structure. A crystal is a periodic arrangement of atoms in space. A space lattice and a basis comprise a crystal structure. The space lattice describes the periodic arrangement of point in which the atoms or group of atoms may be placed, whereas the basis can be a single atom, or an arrangement of atoms placed at each space lattice point.

In the Figure 2.3 it is shown the crystal structure of the Gallium Phosphide (GaP), this is a zinc-blende structure. This structure possesses high symmetry, due to the lattice constant is the same at the 3 perpendicular directions.

This structure is form by two face cubic centered (fcc) lattices displaced one from each other by one quarter in the diagonal of the crystal. It exists 4 GaP molecules at the unitary cell, each atom possesses 4 equidistant atoms from the opposite family arranged in the corners of the regular tetrahedrons[7].

Different effects exist due to the orientation of the zinc-blende crystals because of the polar nature of the structure. The GaP possesses a partially polar character since it is form by the different atoms of the two different fcc sub lattices. The ions from the Ga and P in the crystal assume a positive and negative net charge, respectively.

Due to this polar nature the {111} directions are not equivalent in the zinc-blende structure. In the [111] direction, the crystal may be built up by stacking alternating layers of Ga and P atoms. However, since these layers are not equally spaced but are stacked as … Ga-P—Ga-P—Ga-P. Each Ga atom will be tetrahedrally bonded to three P atoms in the layer directly below and to one P atom in the layer directly above. On the other hand, each P atom will be tetrahedrally bounded to one Ga atom in the layer directly below and three Ga atoms in the layer directly above, which can be seen in the Figure 2.4. This means that an P atom on the (111) surface will have three dangling bonds, whereas a Ga atom on the (111) surface would have on dangling bond. For this reason, this surface will be made up entirely by Ga atoms and is called the (111) A face. On the other side the $(\bar{1}\bar{1}\bar{1})$ face will comprise only P atoms and is called the (111) B face.

The (111) B face is electronically more active than the (111) A face. This is because on the (111) B, pentavalent P atoms are bonded to three Ga atoms in the underlying layer, leaving two free electrons each. In the (111) A face, however, the trivalent Ga atoms each participate in bonding with three P atoms from

the layer below, leaving no free electrons. Because of this, crystal growth and etching both occur rapidly on the (111) B face but slowly on the (111) A. Thus the (111) B face can be polished to a mirror finish and allows smooth epitaxial layers with good crystal quality, whereas the (111) A face is difficult to polish and epitaxial layers on this orientation tends to have poor morphology.

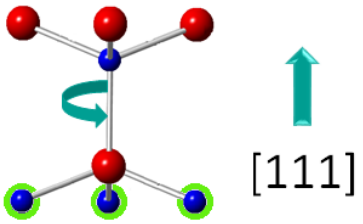

Figure 2.4 Representation of the $(1\bar{1}1)$ plane of a zinc-blende structure seen from the lateral side.

2.3.1 Surface Reconstruction

The surface of a semiconductor substrate will generally take on a structure different from that of a truncated bulk crystal. The driving force for this is energy minimization. In some cases, the rearrangement is rather subtle, altering neither the periodicity nor the symmetry of the surface. This is referred to as surface relaxation. In other cases, the rearrangement is such that changes the periodicity, and perhaps the symmetry of the surface and is called surface reconstruction. Often such reconstructions have been attributed to dimerization of the surface atoms, which serves to reduce the number of unsaturated dangling bonds. Reconstruction can be readily detected by electron diffraction techniques such as RHEED.

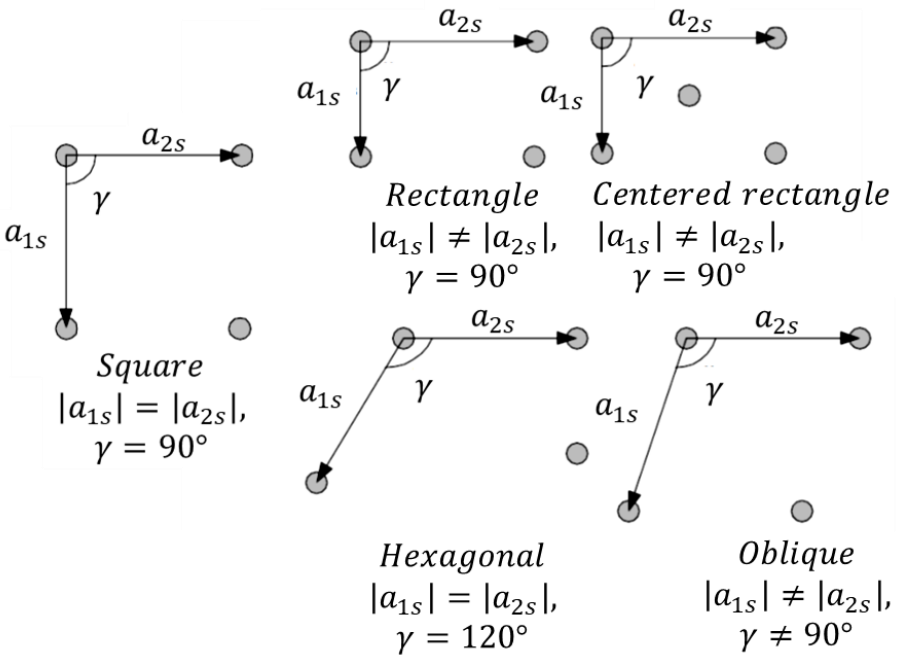

Figure 2.5 Unit cells of the five surface cells[59].

Surface atomic arrangements can be considered to belong to one of the five types of surface cells. These are square, rectangular, centered rectangular, hexagonal, and oblique nets, and their unit meshes are illustrated in Figure 2.5.

The assignment of the surface structure involves the identification of its symmetry and the determination of the positions of the atom within the unit cell. The former is readily found from the positions of diffracted electron beams, but the latter requires an analysis of the diffracted intensities. This interpretation is not straightforward, because phase information is lost in the diffraction pattern.

2.3.2 Wood´s Notation for Reconstructed Surfaces

Usually reconstructed surfaces are classified using Wood´s notation[59]. Suppose a_s is the surface mesh with unit translation a_{1s} and a_{2s}. Further suppose that the mesh of an unreconstructed surface (bulk exposed plane) is a_B with unit translations a_{1B} and a_{2B}. In Wood´s notation, the relationship between the reconstructed mesh and the mesh of the bulk exposed plane is expressed as $(a_{1s}/a_{1B} \times a_{2s}/a_{2B})R$, where R indicates a rotation of the surface mesh with respect to the bulk and is followed by the value of this rotation in degrees. (In the case that there is no rotation of the surface mesh, R is omitted.) The notation $c(\frac{a_{1s}}{a_{1B}} \times \frac{a_{2s}}{a_{2B}})R$ is used to denote a centered mesh. Wood´s notation is applicable to clean surfaces but can also extended to situations involving an adsorbate. Two examples are shown in Figure 2.6.

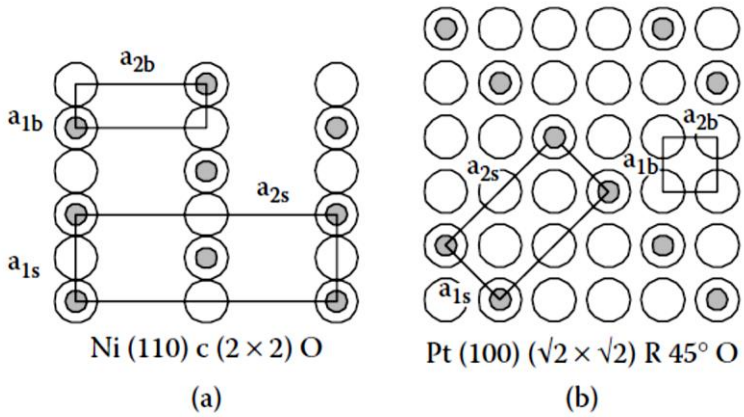

Figure 2.6 Surface structures for a) a Ni(110) surface with adsorbed oxygen, and b) a Pt(100) surface.

In general, the structure of a reconstructed surface will depend on the temperature. Different reconstructions may be observed at different temperatures during the pre-growth processing in an epitaxial reactor. Also, kinetic limitations may prevent the surface from taking on the equilibrium structure. Thus, a reconstructed structure that is stable only at high temperature may remain at lower temperature.

The presence of adsorbed species will generally affect the surface structure. Many surface structures that have been observed on Si only exist in the presence of adsorbed impurities. These could have important implications for nucleation and heteroepitaxy.

Si(001) surface is found to assume a (2×1) type reconstruction[60] if heated in an ultrahigh vacuum or a hydrogen environment. In all probability, the atomic structure of the reconstructed surface is consistent

with the pairing model[61]. However, the c(4×2) reconstruction and other structures have also been observed[62].

The GaP (001) typically exhibit a (2×4) reconstruction and present similar characteristic to the GaAs (001). The typical reconstruction assumes the β_2 structure. This structure contains two As in the first top atomic layer and one As dimer in the third layer per unit cell. At a lower As coverage the α structure is observed. The α structure contains two As dimers in the first layer and two Ga dimers in the second layer, per unit cell. The $\alpha(2 \times 4)$ is usually observed at higher temperatures, whereas the $\beta_2(2 \times 4)$ is generally observed at low temperatures.

2.4 Heteroepitaxy

Epitaxy is the process in which the crystalline orientation of a deposited film is influenced by the crystalline orientation of the substrate employed for the growth. Heteroepitaxy differs from homoepitaxy in that it requires the nucleation of a new phase A on a foreign substrate B. Because of this, the surface chemistry and physics play important roles in determining the properties of heteroepitaxial deposits, including structural and electrical characteristics, defect densities and structure, and the layer morphology.

At typical temperatures employed for epitaxial growth, the substrate surface may undergo a reconstruction, which is an atomic-scale change in the surface structure. The structure of the reconstructed surface may depend on the temperature and adsorbed species. Moreover, in some cases it has been found that the initial structure of the reconstructed substrate effects the structural and electrical properties of thick heteroepitaxial films grow on the surface.

On vicinal (tilted) substrates, the structure of steps and kinks on the surface can have an important influence on the heteroepitaxial growth. For example, in growth of a polar semiconductor on a nonpolar substrate, inversion domain boundaries (antiphase domain boundaries) may develop due to the lower symmetry of the heteroepitaxial crystal. However, it has been found that this behavior can be controlled by the proper choice of the substrate tilt and direction.

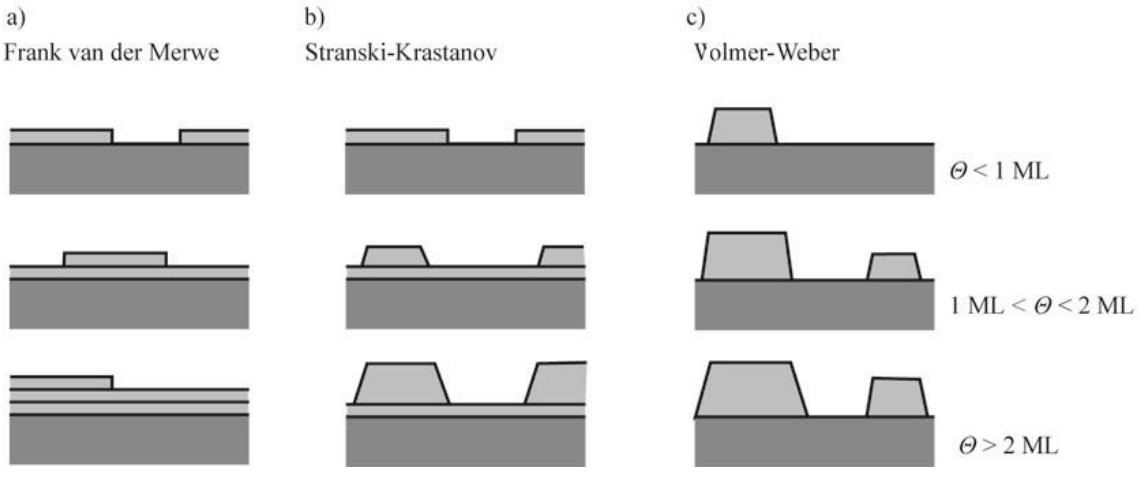

Figure 2.7 Schematic representation of the growth modes a) layer by layer (FM), b) layer and islands (SK), and c) by islands VW. Θ represents the thickness in monolayers.

Either energetics or kinetics may control the nucleation and growth mode for Heteroepitaxy. Traditionally, three possible growth modes have been identified as Frank-van der Merwe (FM), Volmer Weber (VW), and Stranski-Krastanov (SK) growth as shown in the Figure 2.7. The Frank-van der Merwe mode involves layer by layer growth, giving smooth interfaces; it is desirable for most of device applications and is mandatory for quantum well layers. Volmer-Weber (island growth) and Stranski-Krastanov (island on a continuous wetting layer) are undesirable for most applications; however, they can be useful for the fabrication of quantum dot devices. In all these situations, however, understanding the growth mode is important for the design of the device fabrication process.

2.4.1 Growth modes

In the classical theory, the mechanism of heterogeneous nucleation is dictated by the surface and interfacial free energies for the substrate and epitaxial crystal. The energy criteria are stated in terms of $\Delta\gamma$, the areal change in free energy associated with covering the substrate with the epitaxial layer, not including the bulk free energy of the epitaxial crystal. Then if γ_e and γ_s are the surface free energies of the epitaxial layer and substrate, respectively, and γ_i is the interfacial free energy for the epitaxial-substrate interface, then.

$$\Delta\gamma = \gamma_e + \gamma_i - \gamma_s \tag{2.8}$$

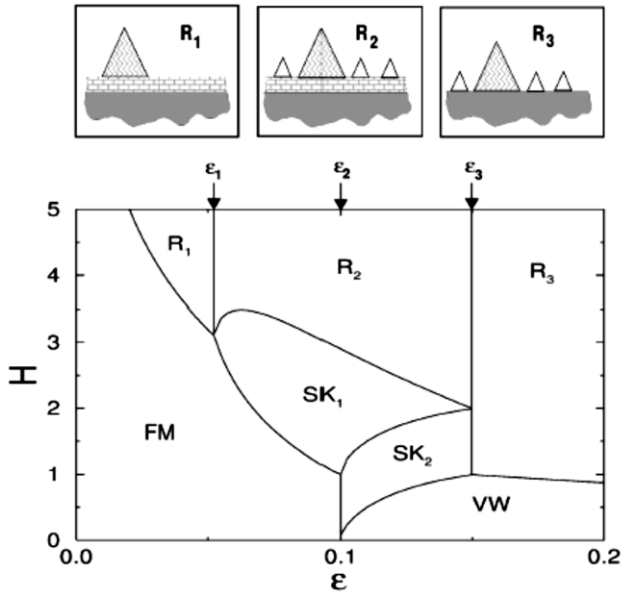

Figure 2.8 Equilibrium phase diagram for heteroepitaxy of a wetting material A on a substrate B. H is the average thickness in monolayers and ε is the lattice mismatch strain[63].

If minimum energy dictates the mode for nucleation and growth, the prevalent mechanism will be two-dimensional for $\Delta\gamma < 0$ and three-dimensional for $\Delta\gamma > 0$. Often the interfacial contribution can be neglected in comparison with the surface energy terms. If this is the case, then two-dimensional growth is expected for $\gamma_e < \gamma_s$ (it is said that the epitaxial layer will wet the substrate) but three-dimensional growth will occur with $\gamma_e > \gamma_s$, the existence of mismatch strain can cause islanding after the growth of a few

monolayers. This is because the strain energy in the coherent epitaxial layer increases in direct proportion to the thickness. At some point, it becomes energetically favorable to create islands that can relieve some of the mismatch strain by relaxation at the sidewalls. Therefore, SK growth mode is to be expected for in the case of a wetting layer unless the lattice mismatch strain is quite small. Whereas the VW growth mode is expected for a nonwetting epitaxial layer, the behavior of a wetting deposit is more complex and warrants further consideration. The wetting layer remains coherent, and lattice matched to the host material, while the QD begins to relax towards its natural lattice constant, therefore in a higher bandgap matrix, the wetting layer exhibits quantum well-like behavior.

Daruka et al. [63] investigated the growth of a lattice-mismatched, wetting epitaxial layer on a foreign substrate and created an equilibrium phase diagram that can help predict the growth mode for heteroepitaxy. In the development of their model, they assumed the growth of a wetting epitaxial layer B on a substrate A, with a thickness of H monolayers and a lattice mismatch f. The total deposit its distributed among the wetting layer with a thickness of n_1 monolayers, stable islands with an average thickness of n_2 monolayers, and large, ripened islands having an average thickness of $H = -n_1 - n_2$ monolayers. Both stable and ripened islands were assumed to be square pyramids with a fixed aspect ratio.

In the Figure 2.8 the phase diagram can be observed. The FM and the VW regions indicates the layer by layer and islands growth mode, respectively. The region R_1 is characterized by existence of the wetting layer and ripened islands (the ripened islands are characterized for no having a height limit), in region R_2 a wetting layer exist with ripened islands, but also stable islands exist, for the region R_3 ripened and stable islands appears but no wetting layer is present. The SK_1 region consist of a Stranski-Krastanov growth mode with stable islands with finite size and density grow on top of the initial wetting layer, a further increase in the growth time will give rise to the appearance of ripened islands along with stable islands (i.e., R_2). In the SK_2 region, we have a SK growth mode with stable islands and a wetting layer but in this case due to a large value of lattice mismatch strain the islands grow first, followed by the wetting layer, which fills in the area separating them. As the growth continues the wetting layer increases its thickness but the stable islands remain fixed in size, this continues until the SK_1 phase boundary is encountered.

2.4.2 Critical thickness

In heteroepitaxial growth where mismatched materials exist, the initial growth will be coherently strained to match the atomic distance of the substrate in the plane of the interface. This means that the pseudomorph layer matches the substrate crystal lattice constant in the plane of the interface, and therefore experiences biaxial compression. As the thickness of the growing layer increases, so does the strain energy in the layer. At some thickness, it becomes energetically favorable for the introduction of misfit dislocations to relax some strain. The thickness at which this happens is called the critical thickness. The usual model to obtain the critical thickness is the Matthews and Blakeslee Model[64]. Here it is considered that a preexisting threading dislocation in the substrate replicates in the growing epilayer and can bend over to create a length of misfit dislocation in the interface once the critical thickness is reached. For the threading dislocation the resolved shear stress acting in the direction of slip is

$$\sigma_{res} = \sigma_{\parallel} \cos\lambda \cos\phi \tag{2.9}$$

Where $\sigma_{\parallel}$ is the biaxial stress, λ is the angle between the Burgers vector and the line in the interface plane that is perpendicular to the intersection of the glide with the interface, and ϕ is the angle between the interface and the normal to the slip plane. The glide force acting on the dislocation is.

$$F_G = \frac{\sigma_{res} bh}{\cos\phi} = \sigma_{\|} bh \cos\ \lambda \tag{2.10}$$

Where b is the length of the Burgers vector for the threading dislocation and h is the film thickness. Assuming biaxial stress in an isotropic semiconductor we have

$$\sigma_{\|} = \frac{2\mathrm{G}(1+v)}{(1-v)}\epsilon_{\|} = \frac{2G(1+v)}{1-v} f \tag{2.11}$$

So that

$$F_G = \frac{2\mathrm{G}bfh(1+v)\cos\ \lambda}{(1-v)} \tag{2.12}$$

Where G is the shear modulus and v are the Poisson ration. The line tension of the misfit segment of the dislocation is given by.

$$F_L = \frac{\mathrm{G}b(1-v\cos^2\alpha\ )}{4\pi(1-v)}[\ln\left(\frac{h}{b}\right)+1] \tag{2.13}$$

G has been assumed to be equal for the epitaxial layer and the substrate, α is the angle between the Burgers vector and the line vector for the dislocations, and h is the layer thickness.

To find the critical thickness, we equate the glide force to the line tension for the misfit segment of the dislocation and solve for the thickness. Denoting h_c we obtain that.

$$h_c = \frac{b(1-v\cos^2\alpha\ )[\ln\left(\frac{h_c}{b}\right)+1]}{8\pi|f|(1+v)\cos\lambda} \tag{2.14}$$

For the case of zinc blende crystals, we have that $\cos\lambda = cos\ \alpha = \frac{1}{2}$ and $b = a/\sqrt{2}$ which corresponds to, whit this the approximated critical thickness for InP/GaP heteroepitaxy 60º dislocations on $\frac{a}{2}\langle 110\rangle\{111\}$ slip systems. The Poisson ratio for the InP is 0.36.

Experimentally the critical thickness in the Stranski-Krastanov mode for GaAs and GaP materials tends to be between 1.4 and 1.8 ml[65], [66].

2.4.3 Crystal defects

A crystal is aperiodic arrangement of atoms in space. A space lattice and a basis comprise a crystal structure. The space lattice describes the periodic arrangement of points on which atoms may be placed, whereas the basis can be a single atom, or an arrangement of atoms placed at each space lattice point. A perfect crystal in practice is almost impossible to achieve. A lot of the properties of the materials are affected by the defects such as electronic conductivity, diffusion, plastic deformation, and mechanical strength, in semiconductors the electronic conductivity is specially affected. Defects can be classified as three basic types of defects in crystals, such as point defects, linear defects, and planar defects.

Point defects appears when the crystal periodicity is not fulfilled at one lattice point or in a neighboring position. The most common point defects are interstitials and vacancies. Interstitials defects are atoms located between the regular lattice sites. Vacancies are produced when an atom is missing from the regular sites.

Dislocations are linear defects often originated because of the application of stressed in the lattice. Linear defects consist of groups of atoms on irregular lattice sites. Two main types of dislocations are classified: edge dislocations and screw dislocations. These are characterized by two dislocation vectors: the dislocation which is the direction of the linear structure, and the Burgers vector which is the principal direction of the strain field near the dislocation.

To find the Burgers vector let us consider a section of the crystal that initial does not contain defects, consider a circuit from atom to atom counting the same number of atomic distances in all directions that is closed, if the circle now includes a dislocation with the dislocation line inside and perpendicular to the circuit, the circuit will deform, the vector that closes the circuit is the Burgers vector. The strain field generated by the dislocation will replace the existing atoms deforming the circuit. If the rectangle is deformed to a trapezium, for edge dislocations the burgers vector will be perpendicular to the dislocation line. The edge dislocation involves an extra half-plane of atoms in an otherwise perfect crystal, the edge dislocation shown in the Figure 2.9 (b) is called a positive edge dislocation, a negative edge dislocation would be called if the extra half-plane of atoms would be in the lower section of the dislocation line. If the rectangle is deformed into a 3-dimensional shape, the Burgers vector will be parallel to the dislocation line (screw dislocation). A screw dislocation can be created by the application of a shear stress. Considering a perfect crystal, if the stress is larger than the elastic limit of the crystal it will cause the atoms on either side of the shear plane to be displaced by one atomic distance. The arrangement of atoms around the screw dislocation forms a single surface helicoid. If the helix advances one plane for each clockwise rotation made around the dislocation line, the dislocation is a right-handed screw dislocation, if the direction is the opposite, then it is a left-handed screw dislocation as shown in the Figure 2.10.

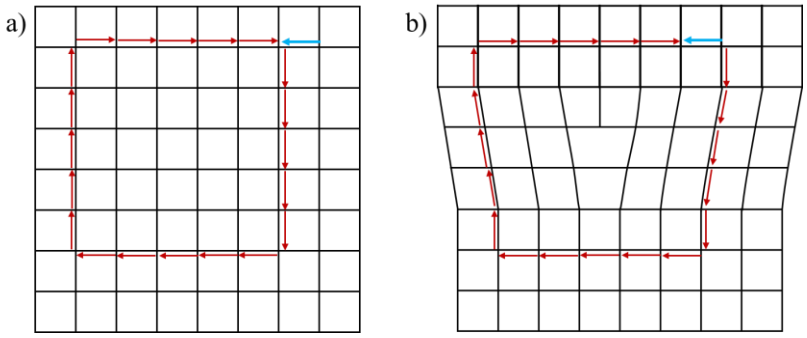

Figure 2.9 a) Burgers circuit in a free defect crystal, b) Burgers circuit enclosing a positive edge dislocation with its line of dislocation into the draw. The closure failure of the circuit denoted as a blue arrow is the Burgers vector.

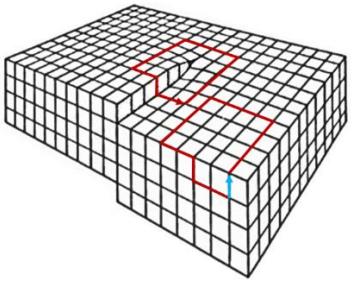

Figure 2.10 Screw dislocation in a crystal. The red line encloses the dislocation and the red circuit with the blue arrow denotes the circuit with the burgers vector. In this case it is a left-handed screw dislocation.

In semiconductor heteroepitaxy different kind of planar crystal defects can be found, such as stacking faults, twins, and antiphase domains.

Stacking faults are defects produced in the stacking of the atomic layers within the crystal, this could be as a fault in the stacking sequence of the layer, a missing layer or an extra layer are called intrinsic and extrinsic stacking, respectively. For example, in the zinc-blende structure in the [111] direction the stacking can be indexed as ABCABC for an intrinsic stacking the resulting sequence will be ABCBC, and for an extrinsic stacking it would be ABCBABC. Stacking faults are planar defects that are bounded on either side by partial dislocations. There are called partial dislocations because the Burgers vector is not a lattice translation vector, this means that the Burgers vector does not start and end on a normal lattice site of the perfect crystal lattice. Stacking faults are created by the dissociation of a perfect dislocation into partial dislocations.

The twins are another type of planar defect resulting from the change in the stacking sequence. In diamond and zinc-blende crystals, the twins occur almost exclusively on the (111) planes. For example, a twin boundary in a zinc-blende crystal may be denoted as ABCABACBA. Here the normal crystal and its twin share a single plane of atoms (the twinning plane or composition plane) and there is reflection symmetry about the twinning plane. Twinning involves a change in the crystal orientation in long-range order of the crystal. This means that twins cannot be created by the insertion or removal of an atomic plane. Twins normally occurs during crystal growth.

Antiphase domains boundaries, also called inversion domain boundaries, play an important role in heteroepitaxy of a polar semiconductor on a nonpolar substrate. Examples include GaN/α-Al_2O_3 (0001), AlN/Si (001), GaAs/Si (001), InP/Si (001), and GaP/Si (001). Due to the lower symmetry of the polar semiconductor, it can grow with one of the two (non-equivalent) crystal orientations on the nonpolar substrate. The boundaries between regions having these two orientations are antiphase domain boundaries (APB). Generally, antiphase domains (APD)s is expected to introduce states within the energy gap and give rise to nonradiative recombination, thus degrading the efficiencies of LEDs and cause excess leakage in p-n junctions. In, addition, the charging of APB will give rise to scattering of charge carriers and degrade the performance of majority-carrier devices such as FETs.

For the heteroepitaxial growth of zinc-blende semiconductor on a (001) surface, APBs that are inclined to the interface may annihilate one another. The annihilation can occur by the interaction of APBs on {111} planes[67]. Here APB annihilation occurs at the line of intersection of the two APB planes, which lies along a <110> direction parallel to the interface. Annihilation reactions can also occur Between APB on {011} planes, which can meet along a <010> direction.

For the GaP growth on Si a two-step growth process of nucleation and overgrowth has been employed for the reduction of APD, with this the formation and annihilation of APDs can be decoupled. The nucleation step helps in creating the site occupation preference to initiate a predominant GaP orientation while the overgrowth conditions enhance the annihilation of APBs by direct it towards another APB. In the Figure 2.11 it is shown how by growth of GaP on Si (100) with a small offcut angle towards the [110] direction can force the propagation of APB originated on adjacent atomic step to self-annihilate.

Efficiency of real multi-junction solar cell tends to be limited by crystal defects, especially misfit dislocations and stacking faults, generated during metamorphic growth, which is responsible of a carrier lifetime shortening (and thus a reduction of the current extraction)

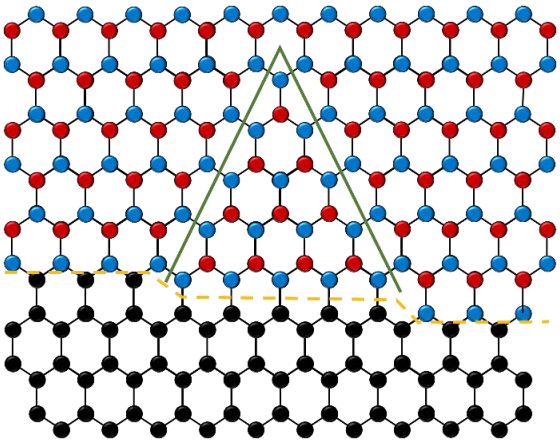

Figure 2.11 Sketch of the (110) cross-section of GaP on Si presenting the self-annihilation of two adjacent APBs (denoted by the green line) originated on different atomic steps.

Lin et al.[48] investigated the effects of V/III flux ratio and growth rate on the propagation and annihilation of antiphase boundaries during the overgrowth step, and discovered that by enhancing the Ga-adatom orientation dependent surface diffusion, the growth of existing antiphase domains was suppressed by the surrounded film such that the antiphase domains annihilated. Suggesting that finding the correct growth conditions that enhance the Ga-adatom orientation dependence surface diffusion will significantly increase the self-annihilation of APD. In the FIGURE it is shown an illustration where anisotropy in Ga adatoms diffusion occurs, within the APD the diffusion length of Ga adatom is longer in the $< 110 >$ direction while outside the APD the Ga adatoms have a longer diffusion length in the $< 1\bar{1}0 >$. The difference in enhanced diffusion in the APD and outside could lead in slightly different growth rates where the surrounding region overgrows the APD, forcing it to self-annihilate.

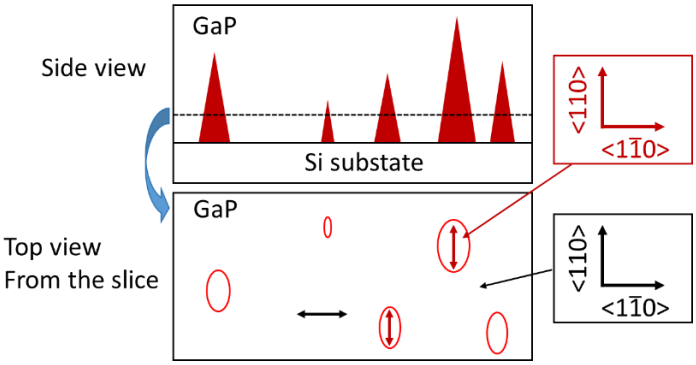

Figure 2.12 Illustration of GaP/Si growth with Ga adatom surface diffusion direction dependent. In the upper image side view of the growth with red sections that represents the APD. In the lower image the top view of the region indicated by the dotted line. In the top view the arrows indicate the longer diffusion direction of Ga adatoms.

2.5 Proposed solar cell.

The search for better renewable energy sources has strongly increased in recent years. Si has been the most employed commercial semiconductor in the solar cells. The highest efficiency of practical Si-based solar cells has already reached values near the maximum theoretical efficiency[68]. To further improve the performance of solar cells, different materials have been researched. III–V compound materials are commonly used in photovoltaic devices with higher efficiencies[27], [28], [30], [32]. However, III–V substrates are expensive, increasing the production cost of these high-performance cells. To overcome this issue, a combination of III–V compounds and Si substrates can be used. Gallium phosphide (GaP) can be an excellent alternative for the integration of III–V materials and Si substrates owing to its low lattice mismatch with Si. In particular, GaAsPN alloys have a large tunable band gap in the range 1.5–2 eV under Si lattice-matching conditions. The Figure 2.13 shows a schematic diagram of solar spectrum absorbed for different wavelength by stacking different semiconductors. Geisz, and Friedman obtained the efficiencies for ideal double junction solar cell using standard spectra shown in the Figure 2.14. In the case of Si as the bottom cell, the highest efficiency of 37% is obtained for a material with a 1.7 eV band gap. For the range of 1.6 to 1.8 eV the efficiency lies from 35% to 36%. GaAsPN can achieve 1.7 eV of band gap becoming ideal for this type of structure.

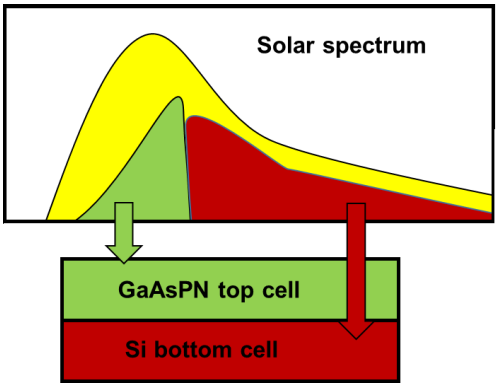

Figure 2.13 Schematic diagram of the solar spectrum absorption in a double junction solar cell.

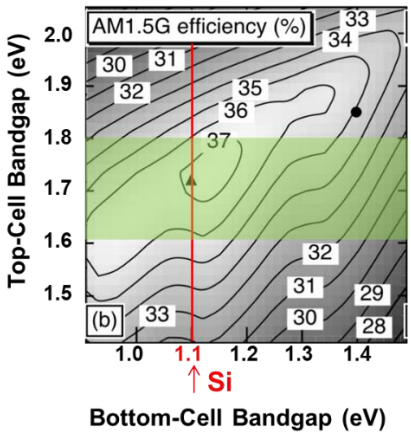

Figure 2.14 Efficiency contour plots of ideal series connect two junction solar cell using standard spectra: AM1.5G.[73]

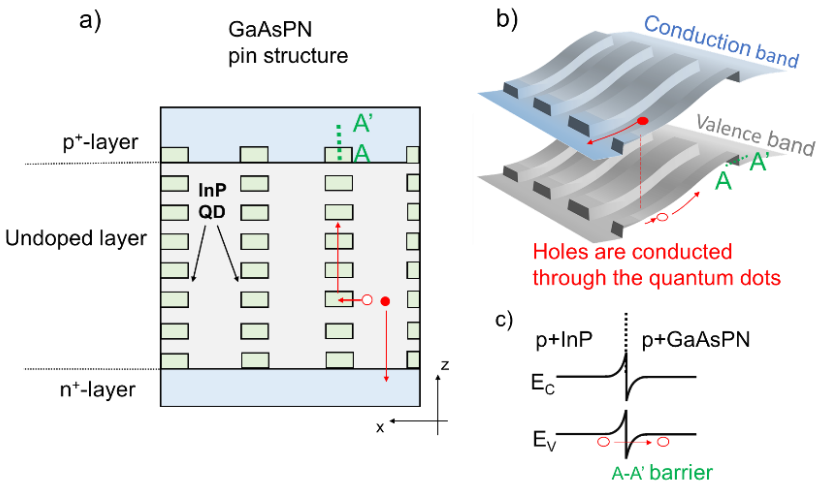

Figure 2.15 Sketch of the energy band diagram for the proposed solar cell. (a) stacked InP QD layer embedded in a GaAsPN pin solar cell structure. The filled circles represent electrons that travel outside the QDs, and the empty circles represent holes traveling through the QDs. (b) Conduction paths of the carriers through the conduction and valence band, the continuous band represents the overlapping of the hole wavefunction through the QDs. (c) Interface between the last QD embedded in the p+ layer is shown.

This study is made with the purpose of producing high efficiency multi-junction III-V-N/Si solar cells. But one drawback from these materials is the poor minority-carrier transport properties. This is a major handicap for the carrier recollection and hence the efficiency. To solve this problem and based on the concept of carrier spatial separation mentioned in the Section 1.5.6, the introduction of type-II stacked QD arrays is one effective way. I plan to use a multijunction solar cell (two junction) as shown in the Figure 2.13 which benefits from the characteristics of lattice matched to Si multijunction solar cells, I plan also to include vertical stacked InP QDs embedded in the GaAsPN layer expected to have type-II band alignment to reduce the carrier recombination in the III-V-N material. The inclusion of the QDs is expected to increase the efficiency compared with a similar cell that does not include the QDs.

In a high crystal quality solar cell based on InP/GaAsPN type-II band alignment by the vertical stacking of InP QDs embedded in GaAsPN, the spatial separation of photo-excited carriers plays a vital role so the carriers can be conducted along the vertical direction reducing the carrier recombination that is typical consequence of the point defects generated in the diluted nitride materials. However, there are a few reports on band alignments and QD stacking in these materials[69]–[72]. This approach differs from the QD approach of the intermediate band gap solar cell that employs QDs to create an intermediate band between the valence and conduction bands to increase the photon energy range that can be absorbed by the cell[35]. In the proposed case, the inclusion of the vertical aligned QDs is not with the purpose of increasing the absorption or create an intermediate band but to increase the carrier recollection and lifetime after the photo absorption occurs in the GaAsPN layer.

Figure 2.15(a) shows the design of the proposed p-i-n solar cell using type-II alignment. To extract the charge carriers from the undoped layer, a structure consisting of vertically aligned InP QDs embedded in a GaAsPN matrix is placed along the absorption layer with p+ and n+ GaAsPN doped layers. By designing GaAsPN as a lattice-matching or slightly tensile strained conditions[74], this structure can be grown on a Si substrate without the generation of misfit dislocations. Figure 2.15(b) represents the band structure of the stacked InP/GaAsPN type-II QDs in the p-i-n solar cell where columnar InP dots forms miniband in the

valence band by the overlap of the hole wavefunctions. With a suitable size of QDs and composition of the GaAsPN layer, a type-II alignment can be formed. In addition, the bandgap of both InP and GaAsPN can be tunable approximately 1.7 eV, as shown hereafter, which is an appropriate value for III–V/Si tandem solar cell[75]. By the band edge discontinuity, electrons and holes will be spatially separated. Electrons are conducted outside the QDs. Holes can be conducted through the mini band inside the QDs caused by the overlap of the hole wave functions. The p+ GaAsPN capping layer next to the QD is incorporated to the structure. By employing heavily doped InP/GaAsPN interface, the conducted holes could be extracted to p+ GaAsPN by tunneling over the valence band discontinuity, as shown in Figure 2.15(c).

Band alignment of the proposed structure was calculated using Nextnano software, which is based on the density functional theory for matrix modeled using an elastic continuum medium[76]. Figure 2.16 shows an example of the band alignments of square plate InP QDs along the <001> and <100> directions. The height and base of the dots were set to be 5 nm high and 20 nm, respectively. The compositions of As, P, and N of the GaAsPN layer were designed to be 19%, 76%, and 5%, respectively, to achieve a bandgap energy of 1.7 eV for III–V/Si tandem solar cell application with lattice-matching conditions to Si. Both Γ and X band show a type-II alignment along <001> and <100> directions. The L band is above the conduction band minimum of both InP and GaAsPN. Inside a InP quantum dot, the energy gap, which is defined as the gap between the ground state of the hole and the conduction minimum, is calculated to be 1.7 eV. These calculation results suggest that InP/GaAsPN is a suitable system that possesses the desired characteristics of the proposed tandem solar cell. In the Figure 2.17 it is also shown the different diameter values for a 5 nm height QDs embedded in GaP, GaPN and GaAsPN matrix, from here 5nm height QD with diameter from 15 and 20 nm can achieve suitable energies. Due to the expected recollection of carriers with the above mentioned energies by the QDs, the Quantum efficiency is expected to increase with the implementation of the vertical aligned QDs. In this case due to the spatial separation of the InP QD valence band and the GaAsPN conduction band the probability of optical absorption is very low. Therefore, this situation is not considered in the proposed concept.

To realize InP/GaAsPN vertical ordered QD array, understanding the initial growth process of InP on GaAsPN and the uniformity of formed InP dots is important. As a first approach to vertical ordered QD array, an InP/GaP system which has a similar lattice-mismatch to InP/Si was employed, to know the growth process and the uniformity of P-rich material system. So, the growth conditions for the nucleation of InP/GaP QDs are needed.

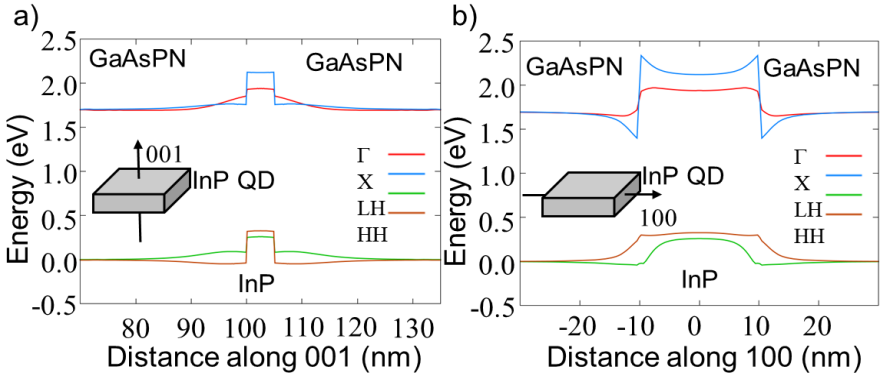

Figure 2.16 Calculated type-II band alignment for InP QD embedded in a GaAsPN matrix. The horizontal axis denotes the (a) [001] direction and (b) the [100], which correspond to a high and lateral size of the QD, respectively.

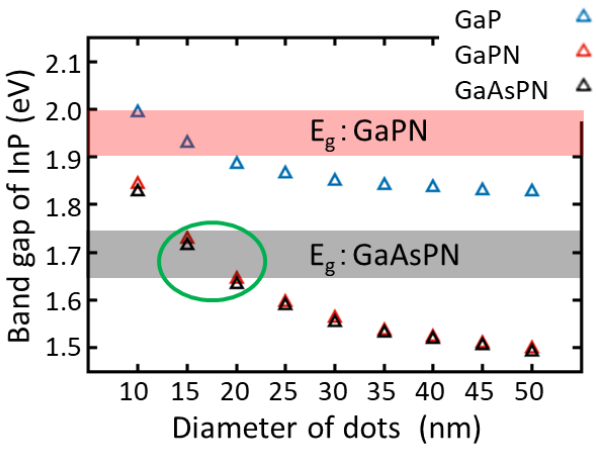

Figure 2.17 Calculated InP QD energy embedded in a GaP, GaPN and GaAsPN matrix for different QD lateral size with a fixed 5 nm QD height.

2.6 Band gap

2.6.1 Energy band

To explain the electronic structure of a material the energy band structure is a very useful concept. The energy band structure is derived from the Schrödinger equation, in the time independent form.

$$\left(-\frac{\hbar}{2m}\nabla^2 + V(\boldsymbol{r})\right)\psi(\boldsymbol{r}) = E\psi(\boldsymbol{r}) \tag{2.15}$$

where ∇ is the gradient, $\hbar$ is the Planck`s constant, and m is the mass of the particle. V(r) denotes the potential energy experienced by the particle. For solids, potential energy depends on the interactions between the particle and all the atoms in the solids. Therefore, finding the exact solution to this problem is quite challenging. Since we are considering a semiconductor crystal; the potential energy is periodic meaning that.

$$V(\boldsymbol{r}) = V(\boldsymbol{r} + \boldsymbol{a}) \tag{2.16}$$

where **a** is the primitive vector of the material. Bloch`s theorem considered that for periodic potential energies the solutions to the Schrödinger equation takes the form of a plane wave modulated by a periodic function. As result, periodicity of the atoms makes the energy states of crystals periodic in E-**k** space, where **k** is the electron wavevector. In addition, the semiconductor crystals have some energies which are forbidden for every **k**-vector.

The relation between the electron wavevector **k** and the energy E is called the dispersion relation. Allowed energy states in E-**k** space form continuous energy bands. In semiconductors the main bands are called valence band and conduction band. The valence band is defined as the highest occupied energy band, and the conduction band as the lowest empty energy band at 0 K. The difference between the minimum of the conduction and maximum of the valence band is called bandgap.

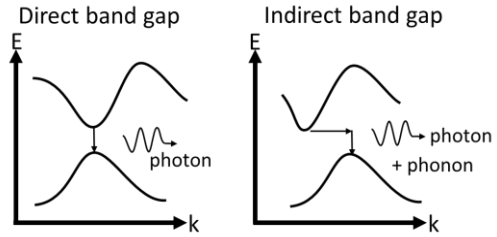

Figure 2.18 Energy band structures for a direct and indirect band gap materials.

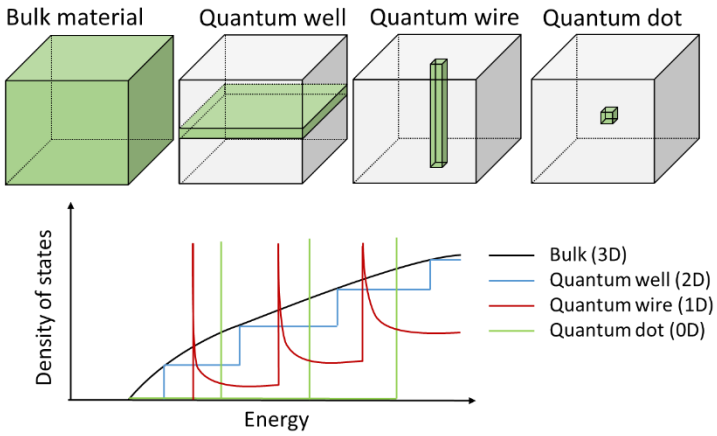

Figure 2.19 Density of states for different ideal structures, depending on the degrees of freedom.

All optical processes occurring in different materials follow the conservation laws of energy and momentum and can be described with E-**k** diagrams. Semiconductors can be classified as direct or indirect band gap materials. In direct band gap materials, the conduction band minimum is located at the same **k**-vector value as the valence band maximum. For indirect band gap materials, the conduction band minimum is not located at the same **k**-vector value as the valence band maximum. For photon emission of absorption phenomenon, the position of the energy states at which the electron is accessible is very important. In emission, an electron that losses its energy going from a minimum state in the conduction band to the maximum state of the valence band will generate a photon with the band gap energy value. For the indirect band gap material another process is required to conserve the momentum, this is normally via phono interaction as shown in Figure 2.18. Which makes direct band gap materials more efficient. In the Figure 1.9 a diagram with different semiconductor band gap over lattice constants is presented.

2.6.2 Quantum structures

The energy value of the band gap is very important for optoelectronic device. A method to control the energy of accessible for the electrons is by spatial confinement. When particles are spatially confinement in lengths comparable to its de Broglie wavelength, it shows quantum effects, as the electron in a quantum well potential. The density of states is the number of states per interval of energy in which an electron can have this energy. In bulk materials carriers are allowed to move in all 3 dimensions, the structures that confine carriers spatially are called quantum wire, quantum well, and QDs when the carriers are confine in one dimension, two dimensions and three dimensions, respectively, as shown in the Figure 2.19. As the

degrees of freedom decrease, the density of states profile becomes narrower, and a smaller number of states can be occupied by carriers. In the case of QDs ideally discrete energy levels are predicted. Fabrication of these structures results in the placement of a small band gap material within a larger band gap material.

2.6.3 Quantum dots

Semiconductor quantum dots (QDs) are of great interest for applications, including single-electron transistors, lasers, infrared photodetectors. In all these applications, the quantum dots may be fabricated by heteroepitaxial growth in a Volmer–Weber or Stranski-Krastanov growth mode. In many cases, the resulting dots may have a random distribution on the growth surface, and this is entirely adequate for some device applications. On the other hand, some applications require the precise positioning of quantum dots, or regular arrays of dots, either one-dimensional or two-dimensional. Self-assembly processes have emerged that appear capable of satisfying these needs, at least to some extent. The term self-assembly has been used extensively in the literature with various meanings. In some cases, the term is used to describe the growth of islands with uniform size, even though their spatial distribution may be quite random. In other cases, self-assembly is used to describe the growth of quantum dot islands in a regular geometric pattern, either one-dimensional or two-dimensional in nature. (This type of self-assembly has also been called self-organization).

In semiconductor the reduction in geometry leads to quantum confinement with sharper density states and unique electronic and optical properties. To obtain these quantum properties is required to meet the following properties[77]; small lateral size which is related to carrier effective masses to achieve expected quantum confinement, relatively narrow size distribution to avoid inhomogeneous broadening of electronic transition in optical applications, interfaces with high degree of definition to produce an abrupt carrier confinement potential, and structural chemical stability, meaning that the interfaces must retain its chemical integrity and being stable against the formation of structural defects during all stages of fabrication.

Confinement in QDs can also arise from electrostatic potentials generated by externals electrodes, doping, strain or impurities[78]. Brus gave the first theoretical calculation for semiconductor particles (using CdS and CdSe as examples) based on ‘‘effective mass approximation’’. In this approximation, an exciton is considered to be confined to a spherical volume of the crystallite of the electron and hole is replaced with effective masses (m_e and m_h) to define the wave function[79].

$$E_{g(qd)} = E_{bulk} + \frac{h^2}{8R^2}\left(\frac{1}{m_e^*} + \frac{1}{m_h^*}\right) - \frac{1.786e^2}{4\pi\epsilon_0\epsilon_r R^2} \tag{2.17}$$

Where $E_{g(qd)}, E_{bulk}$ are the band gap energy of the QD and bulk semiconductor, respectively, R is the radius of the QD, m_e^*, and m_h^* are the effective mass of the excited electron and hole, respectively, and h is the Planck`s constant.

If we assume that the Schrödinger equation can be Decoupled into a radial part and a spherical harmonic part, meaning that $\psi(\boldsymbol{r}) = R(r)Y(\theta, \phi)$. The Brus equation can be used to describe the emission energy of QD in terms of the band gap energy and radius of the QD in the form of [80]:

$$\Delta E(R) = E_g(R) + \frac{h^2}{8R^2}\left(\frac{1}{m_e^*} + \frac{1}{m_h^*}\right) \tag{2.18}$$

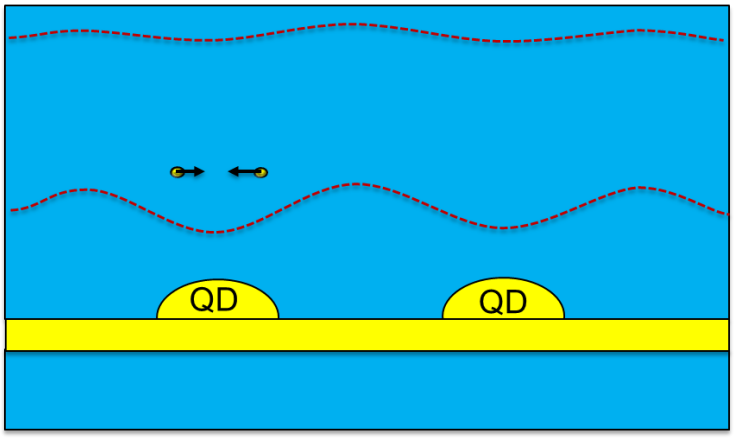

Figure 2.20 Schematic illustration of strain regions due to QDs.

When a capping layer is grown coherently on a strained layer, a biaxial stress is generated in a dislocation-free layer. However, a perfectly flat film with a constant potential along the surface is at an unstable equilibrium because the system can lower its free energy by rearrangement of atomic positions via mass transport along the surface[81], [82]. The presence of QD generates strain regions on the capping layer that provides a mechanism for preferential nucleation of subsequent QDs. This strain region is dependent on the capping thickness as shown in the Figure 2.20. This process of preferential nucleation can be repeated through the multiple stacking of QDs layer forming a well ordered QD arrays. This preferential nucleation process reduces the spatial random formation of QD which reduce QD density and produces more uniform QD size distribution.

2.6.3.1 Indium flushing (IF)

To improve the control of the size of the quantum dots in stacking layers the technique of In flushing[83] has been employed successfully. This consists in the deposition of a capping layer over the quantum dots of a height equal to the desirable maximum height of the quantum dot, after this a thermal treatment (at a higher temperature) is applied to remove all surface In atoms to insure identical growth conditions for each layer. The consequence for this is the modification of the quantum dot shape to what sometimes is called a quantum disk. A variation of this is to perform the thermal treatment at the growth temperature as H. Sasakura et al. mentioned[84] called low temperature-indium flushing (LT-IF).

The overall procedure can be seen in Figure 2.21, first the Quantum dots are formed on the surface, after that a partial capping layer is grown, this will help to control the height of the quantum disk. The normal procedure at high thermal treatment expects that the uncapped quantum dots will completely evaporate and only complete capped quantum dots will remain but it has been found that the capping procedure have significant effect on the dot properties and shape[85]. With an indium flushing at the same growth temperature, it is expected that the In (in the case of InAs QD`s) migrate away to form a new partial wetting layer on top of the GaAs cap. The overgrowth of the capping layer is expected to happen without delivering additional Ga atoms. In practice, the degree to which each of the steps happens will depend on the exact growth kinetics. Indeed, with sufficiently high surface mobility of the group III atoms and relatively slow growth rate of the cap material, the technique will lead to continuous dissolution of the island during the capping process without the need of any growth interruption.

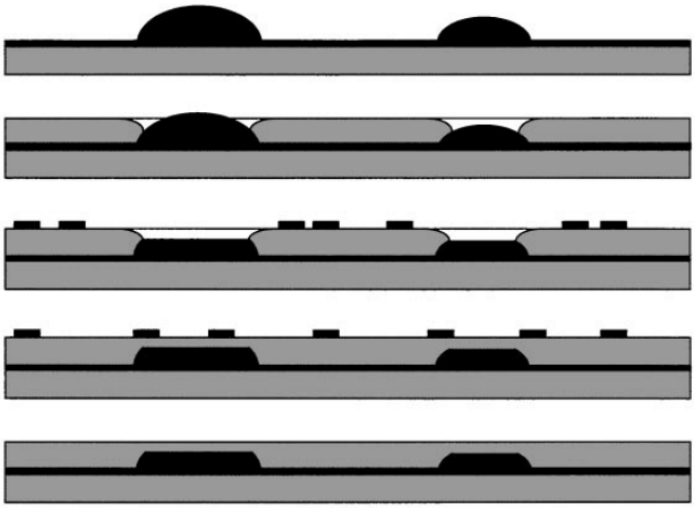

Figure 2.21 Schematic representation of the low temperature indium flushing (LT-IF) technique.

2.6.3.2 Ostwald ripening

Ostwald ripening phenomenon occurring in solid or liquid solutions, it describes its evolution of an inhomogeneous structure over time. In general, any first-order phase transformation process results in a two-phase mixture composed of a dispersed second phase in a matrix. However, because of the large area surface, the mixture is not initially in thermodynamic equilibrium. The total energy of the two-phase system can be decreased via an increase in the size scale of the second phase and thus a decrease in total interfacial area. This is called Ostwald ripening or coarsening. Since the excess energy associated with the total surface area is usually small, such surface energy driven morphological changes typically manifest themselves as the last stage of a first-order phase transformation process[86]. After the formation of QDs, Ostwald ripening force the disappearing of smaller QDs by slowly reducing its size, except for bigger ones which grows at the expense of the smaller ones. This process becomes energetically favorable when the surface of coherent QDs provides a new energy minimization site for other existing QDs. At growth temperatures adatoms diffuse along the surface which allows the coarsening. Coalesced QD can reach geometries of 25 nm height and over 100nm base [87]. These type of QD can be source of lattice dislocations.

2.6.4 Band alignment

To obtain the values of the band alignments at ideal interfaces we need to know the positions of the atoms. For strained-layer interfaces one must include the appropriate strains in each of the materials to construct a pseudomorphic interface, here only perfect pseudomorphic dislocation-free will be considered.

The strains in a pseudomorphic system can be determined by minimizing the macroscopic elastic energy, under the constraint that the lattice constant in the plane is the same throughout the structure (with a the lattice constant and the subscripts $\parallel$ and $\perp$ are used to identify the parallel and perpendicular quantities to the plane interface). We can express the strain tensor components parallel and perpendicular to the plane of the interface. For a system in which h_1 and h_2 are the thickness to the unstrained layers of the semiconductors 1 and 2 respectively, we can obtain.

$$a_{\parallel} = a_1 G_1 h_1 + \frac{a_2 G_2 h_2}{G_1 h_1 + G_2 h_2} \tag{2.19}$$

$$\epsilon_{i\parallel} = \frac{a_{\parallel}}{a_i} - 1 \tag{2.20}$$

$$a_{i\perp} = a_i\left[1 - D_i\left(\frac{a_{\parallel}}{a_i} - 1\right)\right] \tag{2.21}$$

$$\epsilon_{i\perp} = \frac{a_{i\perp}}{a_i} - 1 \tag{2.22}$$

Where i denotes the material 1 or 2 and G_i is the shear modulus,

$$G_i = 2\left(c_{11}^i + 2c_{12}^i\right)\left(1 - \frac{D_i}{2}\right) \tag{2.23}$$

The constant D depends on the elastic constants c_{11}, c_{12} and c_{44} of the respective materials and on the interface orientation.

$$D^{001} = 2\frac{c_{12}}{c_{11}} \tag{2.24}$$

$$D^{110} = c_{11} + 3c_{12} - \frac{2c_{44}}{c_{11} + c_{12} + 2c_{44}} \tag{2.25}$$

$$D^{111} = 2\frac{c_{11} + 2c_{12} - 2c_{44}}{c_{11} + 2c_{12} + 4c_{44}} \tag{2.26}$$

For orientations other than the (001) $a_{\parallel}$ and $a_{\perp}$ do not represent the actual lattice constant in the crystallographic plane of the interface, but merely express how the dimension of the unit cell change under strain, as given by the equations (2.20) and (2.22).

If we have a substrate of semiconductor 1 with an overlayer of semiconductor 2 is the case in which $h_1/h_2 \to \infty$ from equation (2.19) $a_{\parallel} \to a_1$. In general, for the case in which a thin layer is grown on a substrate, the value of $a_{\parallel}$ is determined by the substrate and may varied using different substrates. However, for free standing superlattices $a_{\parallel}$must be determined by using the equation (2.19) once $a_{\parallel}$ is known $a_{i\perp}$ can be obtained using equation (2.20).

These formulas can help us to determine the strain originated in the layers as the atomic positions, except for the interatomic distance for the interface itself. First principles total energy calculation have shown that the interplanar separation between the outermost layers of semiconductors1 and 2 at the interface is close to the average of the layer spacings in the two bulk materials[88].

For the (111) and (110) interfaces, strains reduce the crystal symmetry in such way that the separation of the two atoms in the bulk unit cell of the zinc blende structure is not uniquely determined from the macroscopic strain.

The model solid theory relays in two main aspects; first is the generation of an accurate band structure, and second is the alignment of this band structure to an absolute energy scale. The first part is accomplished by performing density functional calculations on individual bulk semiconductors, described by ab initio pseudopotentials[89]. The calculated band structures include scalar relativistic effects, but no spin orbit

splitting effects, these are added posteriori. The second part that stablish the absolute energy scale can only be present when the energies in the bulk semiconductor can be referred to the vacuum level.

Besides the position of the average valence band on an absolute energy scale, $E_{v,av}$, the model solid approach can give us information about the variation of this energy when strain is present in the system. Shear components of the strain lead to splitting of the valence bands. For the calculation of the bands energies, it is considered the contribution of the effect of the band when the solid is compressed and the effect of the shifting of the electrostatic potential due to the hydrostatic component of the strain. The total effect leads to a hydrostatic deformation of the potential for the valence band:

$$a_v = \frac{dE_{v.av}}{dln\Omega} \tag{2.27}$$

Which express the shift in the $E_{v.av}$ per unit fractional volume change. A similar definition applies to the conduction band deformation potential a_c.

When using bulk semiconductor, one usually considers only the relative shift of the conduction band with respect to the valence band, however, for heterojunction problems values for individual band edges are essential, since they influence the discontinuities at the interface. These effects are expressed as

$$\Delta E_{v.av} = \frac{a_v \Delta\Omega}{\Omega}, \tag{2.28}$$

Where a_v is the hydrostatic deformation potential for the valence band, and $\frac{\Delta\Omega}{\Omega} = tr\left(\underset{\epsilon}{\rightarrow}\right) = \left(\epsilon_{xx} + \epsilon_{yy} + \epsilon_{zz}\right)$ which is the fractional volume change. Similarly,

$$\Delta E_c = \frac{a_c \Delta\Omega}{\Omega}. \tag{2.29}$$

Even when no shear strains are present the valence band is usually split due the spin orbit effects. This allows to obtain the position of the topmost valence band:

$$E_v = E_{v.av} + \frac{\Delta_0}{3}. \tag{2.30}$$

For the conduction band positions we have

$$E_c = E_v + E_g \tag{2.31}$$

Where E_v is obtained from (2.31). The model doesn`t distinguish between different interface orientations, this means that the band lineups at lattice-matched interfaces are therefore independent of interface orientation.

Most of the zinc blende semiconductors includes three degenerate values bands at Γ. These bands are strictly degenerate only in the absence of strain and spin-orbit splitting. They are labeled $E_{v,1}$, $E_{v,2}$ for light and heavy holes bands respectively, and $E_{v,3}$ for the split off band. The average of these 3 bands is referred as $E_{v,av}$. When no strain is present, spin-orbit effects raise the $E_{v,1}$ and $E_{v,2}$ with respect to $E_{v,3}$; the shift of the uppermost bands with respect the $E_{v,av}$ was mentioned in (2.30). The strain splitting is proportional to the magnitude of the strain and is well described in terms of deformation potentials. For strain along [001] the shifts of the valence band with respect the average $E_{v,av}$ are:

$$\Delta E_{v,2} = \frac{1}{3}\Delta_0 - \frac{1}{2}\delta E_{001}, \tag{2.32}$$

$$\Delta E_{v,1} = -\frac{1}{6}\Delta_0 + \frac{1}{4}\delta E_{001} + \frac{1}{2}\left[\Delta^2 + \Delta_0\delta E_{001} + \frac{9}{4}(\delta E_{001})^2\right]^{1/2}, \tag{2.33}$$

$$\Delta E_{v,3} = -\frac{1}{6}\Delta_0 + \frac{1}{4}\delta E_{001} - \frac{1}{2}\left[\Delta^2 + \Delta_0\delta E_{001} + \frac{9}{4}(\delta E_{001})^2\right]^{1/2}, \tag{2.34}$$

Where $\delta E_{001} = 2b(\epsilon_{zz} - \epsilon_{xx})$, with b the shear deformation potential for a strain of tetragonal symmetry, b is negative for the semiconductors interested in this work. With the values taken from [88] for the constants involved the band lineups were calculated. We considered a GaP substrate, above this an InP layer of 5nm thickness and finally a GaP layer. In the Figure 2.22 the illustration of the band alignment is shown, from we can observe that a type II alignment between the GaP and the InP layer is possible.

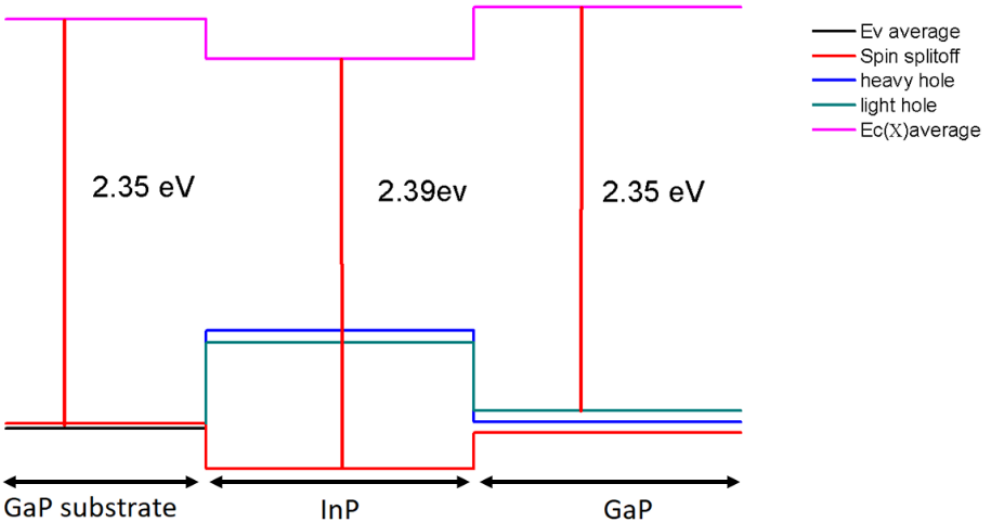

Figure 2.22 Schematic illustration of the band lineup between the GaP and InP, it was considered a 5nm thickness InP. The illustration shows that a type II alignment is possible.

Chapter 3 Characterization techniques

3.1 Reflection of High-Energy Electron Diffraction (RHEED)

The RHEED technique is one of the most important techniques in an MBE system since is a critical in situ diagnostic tool. It allows the verification of a smooth, contaminant free surface prior to growth, as is necessary for the epitaxy of high-quality material. It can also be used to determine the growth rate, composition, and growth mode in situ. Surface structure can be studied by RHEED as well. Electron diffraction techniques require a high vacuum, and therefore cannot be used for in situ diagnostics during vapor phase epitaxy.

In s typical RHEED experiment, high energy (10- to 100 keV) beam of electrons is incident on the sample surface at a small angle of 1° to 2°. Diffraction of the electrons is governed by the Bragg law, as with x-ray diffraction. However, there are two important differences between RHEED and x-ray diffraction. First, the electrons do not penetrate significantly into the sample, so diffraction is essentially from the two-dimensional surface lattice. Second, for the high-energy electrons used in RHEED, the Ewald sphere is large in diameter, so many reflections are excited at once.

Because the diffraction occurs from a two-dimensional net of atoms on the surface, the reciprocal lattice comprises a set of rods perpendicular to the surface in the real space. These rods can be indexed using the two Miller indices hk.

The electrons in a RHEED experiment behave as waves, with a de Broglie wavelength given by

$$\lambda = \frac{hc}{E} \tag{3.1}$$

Where h is the Planck constant, c is the speed of light, and E is the electron energy. For example, an electron energy of 100keV correspond to a de Broglie wavelength of 3.7 pm. The radius of the Ewald sphere is $|k_0| = 1700\ nm^{-1}$. The Ewald sphere is so large compared to the separation of the reciprocal lattice rods that It will intersect several rods, exciting several Bragg reflections for any given geometry. The diffraction pattern therefor e comprises a set of streaks, as shown in Figure 3.1.

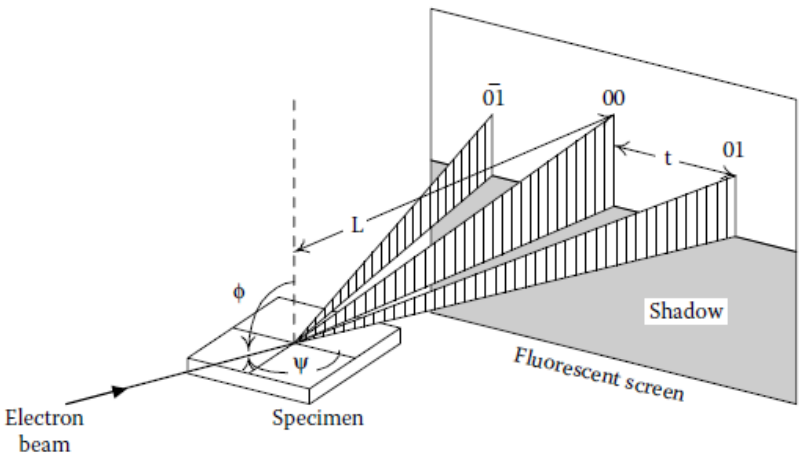

Figure 3.1 Reflection high-energy diffraction experiment[90].

If the distance from the sample to the screen is L and the separation between the 00 and hk streaks on the screen is t, then.

$$t = L\tan(2\theta_{hk}) \tag{3.2}$$

If the surface structure is a square lattice with lattice constant a, then by the Bragg law,

$$\lambda = 2d\sin\theta_{hk} = \frac{2a\sin\theta_{hk}}{(h^2+k^2)^{1/2}} \tag{3.3}$$

In a RHEED experiment, $\lambda \ll a$ so that

$$a \approx (h^2+k^2)^{\frac{1}{2}}\lambda L/t \tag{3.4}$$

Therefore, the lattice constant for the surface may be determined. This analysis can be extended to other surfaces lattices, and by performing RHEED experiments at different azimuths ψ, it is possible to determine the dimension of the surface unit mesh.

RHEED is commonly used in situ during MBE growth to discern the growth rate and growth mode. In the case of Frank-van der Merwe (layer by layer) growth, a streaky diffraction pattern is obtained, and the intensity of a particular streak oscillates with time. Much information is contained in the RHEED oscillation characteristics, and sophisticated models have been developed for their analysis. To determine the growth rate and layer thickness, it suffices to recognize that one period of the growth rate corresponds to the growth of 1 ml. The intensity is maximum for a smooth surface. The nucleation of a new layer on this surface causes a roughening until the new layer completes, and the process repeats, this process is shown schematically in Figure 3.2. If the period of the RHEED oscillations is T, then the growth rate is.

$$g = \frac{1ML}{T} \tag{3.5}$$

The surface roughness, and therefore the growth mode, may be discerned from the nature of the RHEED pattern. As noted previously, a streaky pattern is an indication of an atomically flat surface. In the case of the rough surface, the electron beam will penetrate islands or other structures on the surface, giving rise to diffraction from a three-dimensional lattice, showing a spotty RHEED pattern.

As mentioned, with the observation of RHEED patterns it is possible to distinguish between a rough surface and a flat surface, since the growth of QD´s by the Stranski-Krastanov growth occurs from a transition from a two-dimensional growth to a three-dimensional growth it is possible to monitor this transition. Transmission through quantum dots with low index facets produce chevrons a schematic representation of the chevron´s origin is shown in the Figure 3.4. The interrelationship between parallel planes and chevron formation provides a suitable approach to determine the facets forming the quantum dots in certain directions by calculation the chevron angle.

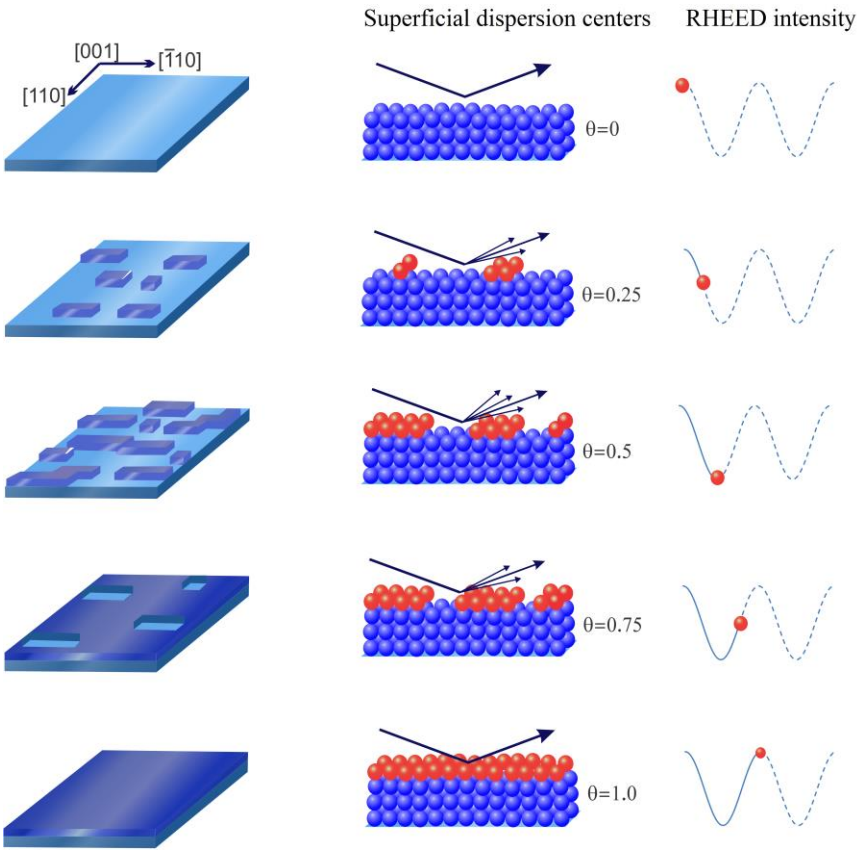

Figure 3.2 Scheme of the specular spot intensity of a RHEED pattern as function of the rate coverage, been θ the monolayers.

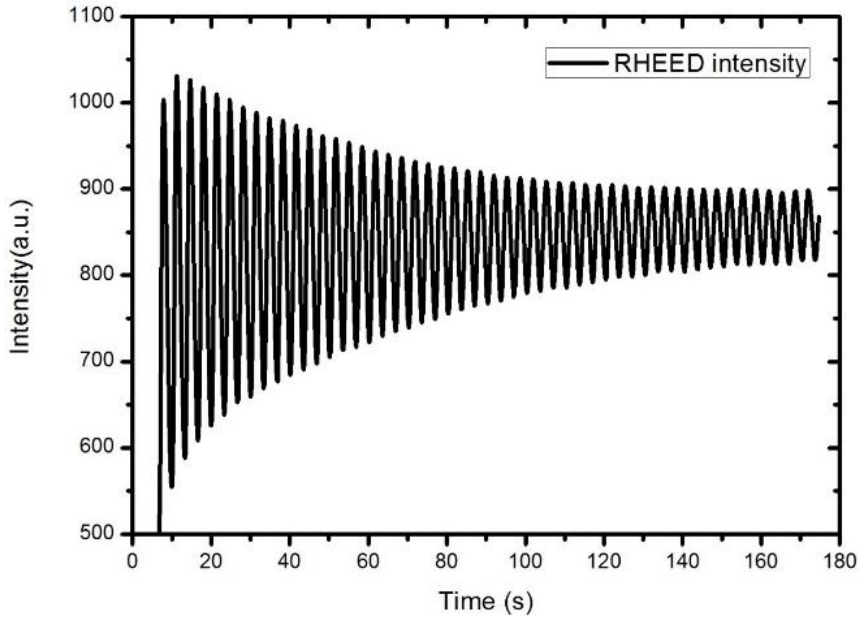

Figure 3.3 RHEED Intensity oscillations of a GaP layer with a 0.3 µm/h growth rate.

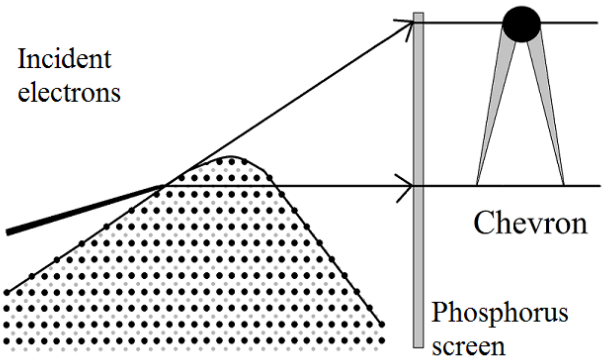

Figure 3.4 Schematic representation of the Chevron formation.

3.2 Atomic Force Microscopy (AFM)

The Atomic Force Microscopy (AFM) allow us to observe the surface, thus characterize the surface morphology and growth mode. AFM has sufficient resolution for the study of the surface atomic structure. An AFM system consist of a sharp tip which is mounted on the tip of a millimeter-size cantilever as shown in the Figure 3.5. The AFM measurements can be performed to insulating surfaces. An AFM measures the force between the tip and the sample. A force F exerted on the tip by the sample deflects the cantilever by Δz:

$$F = C\Delta z \tag{3.6}$$

Where C is the force constant of the cantilever. The displacement of the cantilever is measured as a function of tip position, often by using the back of the cantilever as a reflector for the laser beam which is measured by a photodetector. Motion of the reflector changes the path of the laser beam, which is detected using a photodiode array; picometer-scale displacements can easily be measured. Since a typical value of the force constant is $C = 1N/m$ pN-scale forces van be transduced. Forces well below 1fN have been measured under special circumstances.

The simplest mode of operation is contact mode, where the tip is dragged along in contact with the surface and the cantilever deflection is measured. This gives a measure for the sample topography, but it can damage the sample. Noncontact or intermittent-contact imaging modes are less invasive, and they also can give information about the long-range forces between the sample and the tip. In these techniques, the cantilever oscillates just above the sample due to an applied driving force of amplitude $F\omega$ near the cantilever resonance frequency ω_0. Modeling the cantilever as a driven simple harmonic oscillator, the magnitude of the cantilever response at a frequency ω is given by.

$$|z_\omega| = \frac{F_\omega}{C}\frac{\omega_0^2}{\left[(\omega^2-\omega_0^2)^2+\left(\frac{\omega\omega_0}{Q}\right)^2\right]^{1/2}} \tag{3.7}$$

Where Q, the quality factor of the oscillator, is the ratio of the energy stored in the cantilever to the energy dissipated per cycle. Note that on-resonance, $\omega = \omega_0$, the response is Q times larger than at low frequencies, making the detection of small forces possible.

The parameters characterizing the oscillating cantilever are sensitive to any forces that occur between the tip and the sample. These forces can be van der Waals, electrostatic, magnetic, or other. The interaction shifts the resonance frequency ω_0 and/or modifies Q. This change is recorded and used to construct an image. For example, in tapping mode imaging, the tip ´´taps´´ the surface during the closest approach of the oscillation cycle, causing both a frequency shift and additional dissipation.

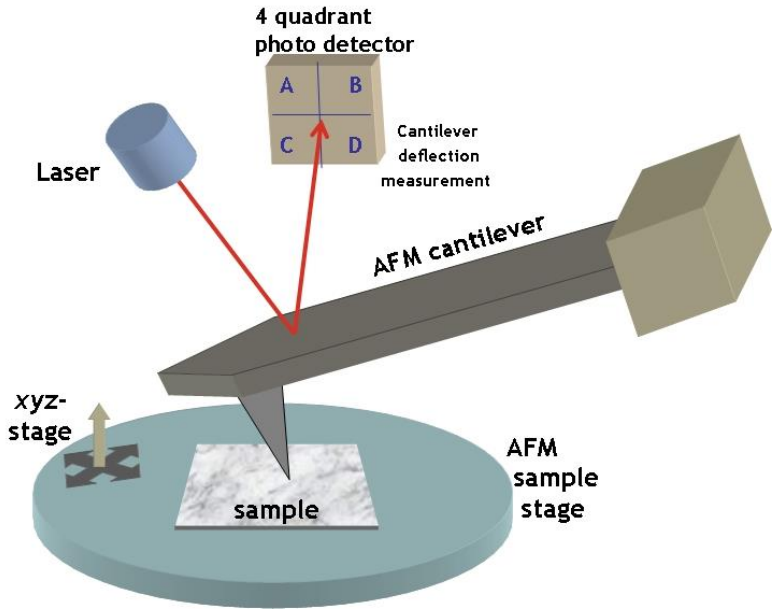

Figure 3.5 AFM schematic principle system.

3.3 Transmission Electron Microscopy (TEM)

Transmission electron Microscopy (TEM) is a valuable technique for the observation of dislocations, stacking faults, twin boundaries, and other crystal defects in heteroepitaxial layers. TEM characterization is applicable to most heteroepitaxial conductor samples, if they can be thinned to transmit electrons and that they are very stable when exposed to a high-energy electron beam in ultrahigh vacuum. Conventional TEM use electron energies of ~100keV, whereas this could be ~1 MeV in a high-voltage TEM. For observation in a conventional TEM, typical heteroepitaxial samples must be thinned to less than about 100 nm. This requirement may be relaxed somewhat if the sample is made up of light atoms with low atomic number or if high-voltage electrons are used. The sample preparation is destructive, and in some cases, it can alter the defects that are to be observed.

The electrons in a TEM behave as waves, with a de Broglie wavelength given by Equation (3.1.). The TEM uses lenses to produce an image, but the lenses are electromagnetic in nature. Lens aberrations, along with mechanical and electrical instabilities, usually limit the resolution of the TEM to 0.2 nm.

The operation of a TEM instrument is shown schematically in Figure 3.6. Collimated high energy electrons from a condenser lens impinge on the semiconductor specimen and are transmitted through it.

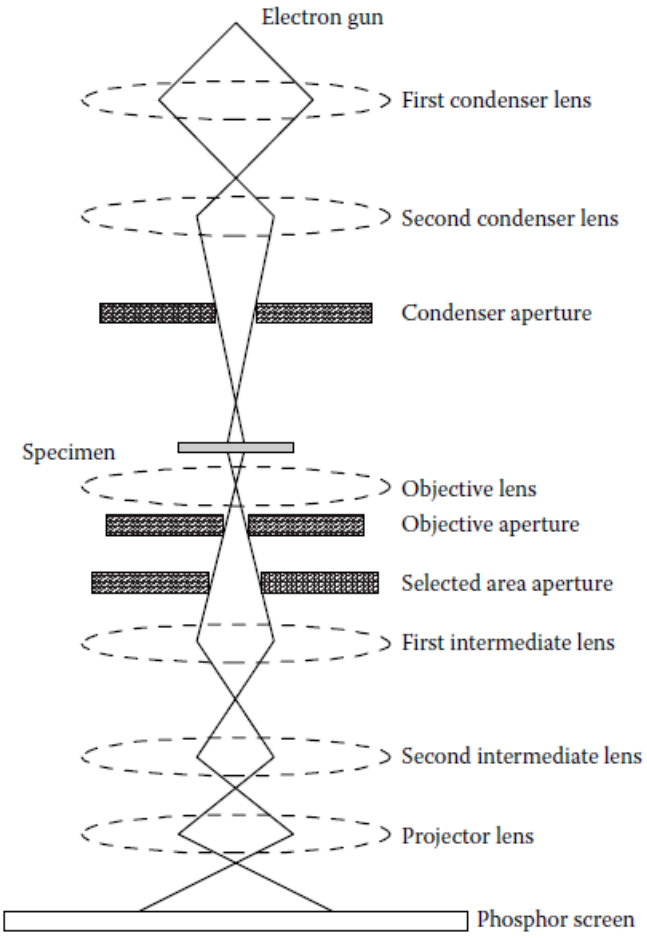

Figure 3.6 Transmission electron microscope set up[90].

The electrons are scattered into directions by the crystalline sample according to the Brag law for diffraction. These diffracted beams are brought into focus at the focal plane for the objective lens.

In the diffraction mode, the first intermediate lens is focused on the back focal plane of the objective lens, thus capturing the diffraction pattern. This diffraction pattern is magnified and projected by the combination of the intermediate and projection lens. The diffraction pattern displayed on the screen comprises an array of spots, each corresponding to a particular diffraction vector g. The diffraction mode is used to index the diffraction beams and to facilitate the selection of the diffraction spots to be used in ultimately forming an image.

In the imaging mode, the intermediate lens is focused on the inverted image of the sample formed by the objective lens. This image is magnified and projected onto the screen with an overall magnification of up to 10^6. An aperture at the back focal plane of the objective lens is used to select only one diffracted beam to form the image. If the beam transmitted directly through the image g = [000] is chosen, a bright field image result. If one of the diffracted beams is chosen to form the image, then a dark-field image is produced.

The variation of the image intensity leaving the specimen may be understood using two simplifying approximations. First, the specimen is assumed to behave as if made up of narrow columns (the column approximation) with axes parallel to the incident beam. The image therefore represents an intensity bit map

for the array of columns. Second, it is assumed that the image is formed by the directly transmitted beam plus only one diffracted beam (the two-beam approximation).

A uniform, perfect crystal, with uniform thickness, will produce an image with uniform electron intensity. Image contrast results from crystal nonuniformities, including variations in thickness, changes in composition, inclusions, and voids. Dislocations may also produce image contrast, if they displace the diffracting planes such that their separation or orientation changes. Based on the column approximation, we can state that the condition for image contrast by a crystal defect is $g \cdot u \neq 0$, where u is the vector by which atoms are displaced from their normal sites within a particular column. In other words, the condition for invisibility is $g \cdot u = 0$.

For an edge or screw dislocation, image contrast will result if the Burgers vector has a component in the direction of the diffraction vector. Again, the condition for invisibility (zero contrast) for an edge or screw dislocation is.

$$g \cdot u = 0 \tag{3.8}$$

For dislocations of mixed character, there is no condition for which $g \cdot u = 0$. Instead, the invisibility criterion is approximately satisfied for $g \cdot b = 0$ and weak contrast is observed even if $g \cdot b = 0$.

The invisibility condition can be applied to the determination of the Burgers vector direction for a dislocation. If a dislocation is invisible (or nearly invisible, in the case of mixed dislocation) in two images produced using the diffraction vectors g_1 and g_2, then its Burgers vector must be perpendicular to both diffraction vector, this means it is in the direction $g_1 \times g_2$. In this way, the Burgers vector, and the character (edge, screw, or mixed) may be determined for dislocations in a heteroepitaxial layer.

A critical step in the TEM experiment is the sample preparation. It is necessary to prepare a thin foil that includes the region to be examined and that is thin enough to transmit the electrons. Often this can be achieved by a combination of wet etching and ion milling. In some cases, etch stops layers can be used for the preparation of thin foils.

Chapter 4 Diffusion length

4.1 Introduction

In this chapter, a method for evaluating the surface diffusion length of Ga adsorbed atoms during GaP growth is discussed, this information will be valuable for the initial steps in the GaP growth on Si due to the contribution in the annihilation of antiphase domains and in the caping process of quantum dots since the diffusion of Adatoms plays a fundamental role.

The theoretical growth rate distribution near the boundary between two different planes is shown by solving the diffusion equation which is based on the evaluation method for the surface diffusion length in GaAs growth [91]. A stripe structure is etched in a GaP (001) substrate by photolithography and chemical etching, next, GaP is grown on the stripe structure, which was employed for this method, the grown film thickness near the surface boundary is observed with a transmission electron microscope (TEM), and theoretical fitting based on diffusion theory is performed.

Diffusion length of adatom on the grown surface is one of the decisive factors to understand the growth mechanism since for techniques such as MBE which operates outside the thermodynamic equilibrium and the interaction between adatoms, and the surface atoms can strongly affect the overall growth. This behavior is also important in the formation of nanostructures such as quantum wells and quantum dots. Nishinaga et al. [92] measured in situ the diffusion length of Ga adatom (λ_{Ga}) for GaAs (001). In their experiments

4.2 Example of reported surface diffusion length in GaAs growth rf-MBE

There has been some studies about the surface diffusion length of Ga adatoms during GaAs[91], [93]–[95]. For example Nishinaga et al. [91] used the diffusion phenomenon of atoms between two different adjacent planes, they observed the distribution of the growth rate at the initial growth near the boundary of the plane from the RHEED oscillation intensity, the surface diffusion length is derived by applying a one-dimensional growth model using diffusion theory .Figure 4.1 shows the principle in which by measuring the growth rate distribution on one facet near the boundary, one can know the direction of the surface diffusion. If the growth rate decreases as the distance is increased, then the lateral flux is coming from the adjacent facet, in the other case if the growth rate increases as the distance is increased, then the lateral flux is going in the direction of the adjacent facet.

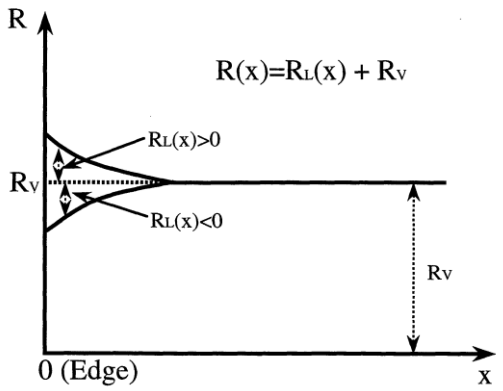

Figure 4.1 RHEED Schematic illustration of the distribution of the growth rate on the (001) GaAs surface near the edge. Where $R_L(x)$ is the growth rate due to the Ga lateral flux and R_v is the one due to the direct Ga flux[91].

4.3 One-dimensional growth model using diffusion theory.

In accordance with the diffusion theory reported for GaAs growth [96], a theoretical formula for estimating the surface diffusion length from the grown film thickness is derived below. A schematic diagram of the cross section of two different adjacent crystal planes as shown in the previous section is shown in Figure 4.2. Each parameter in this section is defined as follows.

n: Adsorbed atom concentration

Ji: Supply amount from molecular beam

Di: Surface diffusion coefficient

ai: Constant corresponding to the amount of interplanar diffusion

$\tau\, i, inc$: Lifetime of adatoms until incorporation to the crystal

$\tau\, i, des$: Lifetime of adsorbed atoms until detached from the surface.

$\tau\, i$: Overall lifetime of adsorbed atoms

$\lambda\, i$: Surface diffusion length of adsorbed atoms

C: Adatoms volume

θ: angle formed by two different crystal planes.

$Tdirect$: Growth thickness due to molecular beam

$Tdiff$: Constant related to growth film thickness due to interplanar diffusion

Consider the diffusion equation near the boundary on two different surfaces. When the boundary region is set to x = 0 the diffusion step, then the expression is

$$\frac{dn}{dt} = J_1 + D_1\frac{d^2n}{dx^2} - \left(\frac{n}{\tau_{1,inc}} + \frac{n}{\tau_{1,des}}\right) \qquad (x > 0) \qquad (4.1)$$

$$\frac{dn}{dt} = J_2 + D_2\frac{d^2n}{dx^2} - \left(\frac{n}{\tau_{2,inc}} + \frac{n}{\tau_{2,des}}\right) \qquad (x < 0) \qquad (4.2)$$

Assuming that the substrate rotates sufficiently quickly during growth, the relationship between J 1 and J 2 is.

$$J_2 = J_1\cos(180 - \theta) \qquad (4.3)$$

Considering that crystal growth by simultaneous supply is in a steady state, solving differential equations (4.1) and (4.2) with a big concentration of adatoms.

$$n(+\infty) = \frac{1}{\frac{1}{\tau_{1,inc}} + \frac{1}{\tau_{1,des}}}J_1 = \tau_1 J_1 \qquad (x > 0) \qquad (4.4)$$

$$n(+\infty) = \frac{1}{\frac{1}{\tau_{2,inc}} + \frac{1}{\tau_{2,des}}}J_2 = \tau_2 J_2 \qquad (x < 0) \qquad (4.5)$$

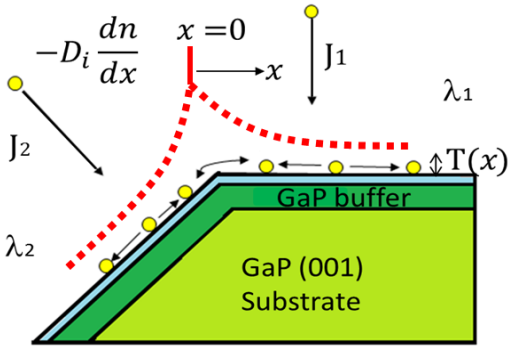

Figure 4.2 Schematic diagram of the cross section of two adjacent crystal planes.

The solution of the differential equation can be expressed as

$$n(x) = \tau_1 J_1 + a_1 e^{-\frac{x}{\lambda_1}} \qquad (x > 0) \tag{4.6}$$

$$n(x) = \tau_2 J_2 + a_2 e^{-\frac{x}{\lambda_2}} \qquad (x < 0) \tag{4.7}$$

With the boundary condition

$$n(+0) = n(-0) \tag{4.8}$$

$$D_i \frac{d_n(+0)}{dx} = D_2 \frac{dn(-0)}{dx} \tag{4.9}$$

By solving equations (4.6) and (4.7), the atomic concentration becomes

$$n(x) = \tau_1 J_1 + \frac{\tau_2 J_2 - \tau_1 J_1}{1 + \frac{D_1 \lambda_2}{D_2 \lambda_1}} e^{-\frac{x}{\lambda_1}} \qquad (x > 0) \tag{4.10}$$

Assuming that the volume of adsorbed atoms is C, and the growth time is t, the growth film thickness is.

$$T_1(x,t) = \int_0^t \frac{C_n(x)}{\tau_{1,inc}} dt \qquad (x > 0) \tag{4.11}$$

It can be obtained that.

$$T_1(x,t) = C \left(\frac{\tau_2 J_2 - \tau_1 J_1}{1 + \frac{D_1 \lambda_2}{D_2 \lambda_1}} e^{-\frac{x}{\lambda_1}} + J_1 \right) t = T_{direct} \pm T_{diff} e^{-\frac{x}{\lambda_1}} \tag{4.12}$$

Which can be relabeled as

$$T(x) = T_0 + T_1 e^{-\frac{x}{\lambda_1}} \tag{4.13}$$

Where T_0 to the growth thickness due to the molecular beam and T_1 the constant value on growth film thickness due to interplanar diffusion. From this it is obtained that the growth film thickness changes exponentially from the boundary.

4.4 Experimental method

Samples were grown using a molecular beam epitaxy apparatus, and the growth was carried out on GaP (001) substrates with patterned stripes. The stripes were prepared by photolithography and chemical etching in a solution of $HCl:H_2O_2:H_2O$ = 20:1:15. Before loading the sample into the chamber, photoresist was removed using the chemical solution JELK-101 followed by HCl treatment for the removal of native oxide layer. The obtained stripes are shown in the Figure 4.3. Two sets of stripes of 4~8 μm width and 1 μm depth were arranged in every substrate oriented along the $< 110 >$ direction and along the $< 1\bar{1}0 >$ direction. The stripes are formed by the $< 110 >$ or $< 1\bar{1}0 >$ and the $< 111 >$ facets. The sample also include a non-pattern section in order to perform AFM measurements as shown in Figure 4.4. After the growth, the samples were prepared for TEM observation. Molecular species Ga/Al and P_2 were supplied by using a solid-source effusion cell filled with metallic Ga(7N)/Al(6N) and a valve cracker cell filled with phosphorus (6N), respectively. Samples were thermally treated 10 min. at 700 °C. The structure consisted of 30-nm-thick GaP buffer layer grown at 600 °C, 5-nm-thick AlP marker layer was used in most of the samples and a 100-nm-thick GaP layer for the diffusion length measurement. The samples were prepared using a constant GaP growth rate of 0.3 μm/h with a V/III flux ratio of 4. The growth temperature was varied from 500 °C to 650 °C.

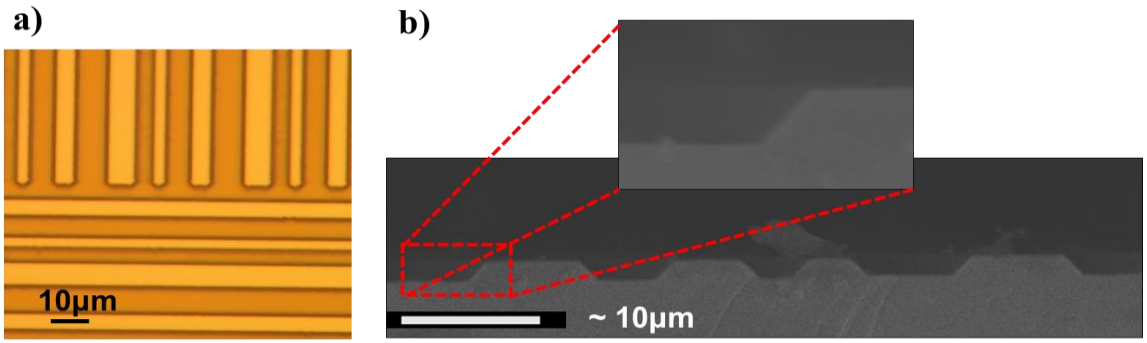

Figure 4.3 Stripe structure image by a) optical microscope and b) sectional SEM.

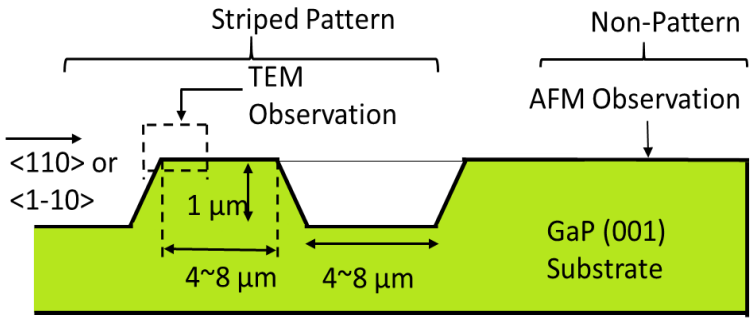

Figure 4.4 Sample stripe structure scheme.

4.5 Results

4.5.1 RHEED results

Figure 4.5 shows the RHEED patterns during the growth at the different temperatures employed in the diffusion length study for the $< 110 >$ and $< 1\bar{1}0 >$ directions, 2×1 reconstruction was observed at 500 °C which changed to a 2× 4 reconstruction with the temperature increase. Although sharp streaks were confirmed at 650 °C, surface reconstruction was unclear. After growth, 2×4 reconstructions appeared in samples grown at 550 °C, 600 °C and 650 °C. These results suggested that all the samples were grown with relatively flat surface though morphological investigation is shown hereafter.

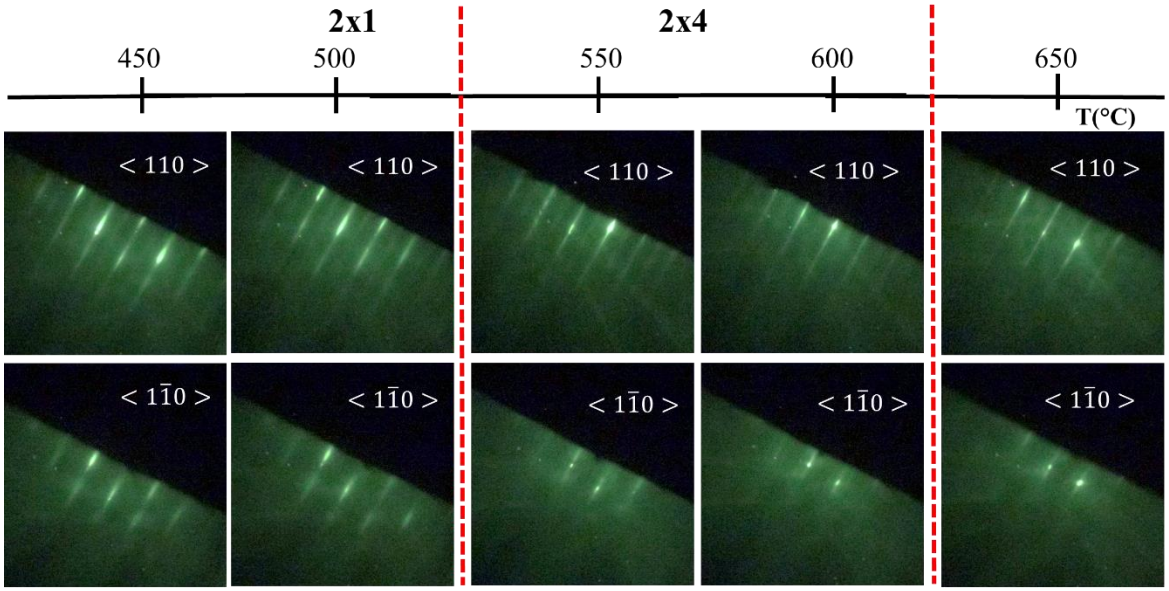

Figure 4.5 Typical RHEED patterns during the growth of GaP layers for all the growth temperatures and a V/III ratio of 4.

4.5.2 Diffusion length estimation

For all the samples the increase in the growth rate was observed near the edge of the stripe as sketched at Figure 4.4. A typical example of TEM image is shown at Figure 4.6, here the is an increase of the thickness in the deposited layer at the edge of the stripe can be observed caused by the flux of adatoms at the adjacent plane. Surface was composed of (113) facet and sloped (001) plane with exponential curve instead of the $< 111 >$ facet. The (113) facet was likely originated from the $< 111 >$ facet formed on the striped pattern substrates and net Ga adatom diffusion would occur from (113) facet to (001) plane. Then, the diffused Ga adatoms incorporated with the λ_{Ga} on (001) plane resulting in a sloped (001) with exponential curve. Through image analysis the thickness distribution was obtained, and the fitting employed for the diffusion length estimation from the sample grown at 600 °C is shown in the Figure 4.7 for both directions. The data is well fitted to the Equation (4.13) so the λ_{Ga} was estimated around 0.27 µm for the $< 110 >$ direction and 0.63 µm for the $< 1\bar{1}0 >$ direction. The value of the λ_{Ga} for $< 110 >$ direction ranged from 0.11 µm to 0.75 µm and for the $< 1\bar{1}0 >$ direction it ranged from 0.06µm to 1.7µm at current growth conditions as

shown in the Table 4-1. With these values the plot of the diffusion length as a function of growth temperature (1000/T) is shown in Figure 4.8. For most of the temperatures used the λ_{Ga} along $< 1\bar{1}0 >$ direction is bigger than the one at $< 110 >$ direction also a clear dependence on the temperature is observed. From the data presented in the Figure 4.8 it is possible to estimate the values for the diffusion lengths at 480 ºC of growth temperature, this information may be useful for the stacked quantum dots study. The estimated diffusion length along the $< 1\bar{1}0 >$ direction is 53nm and for the $< 110 >$ direction is 98nm, these values are very close to the ones measured at 500 ºC, as we can see from the data the variation of growth temperature in this region of the curve is much less significant compared to higher temperatures. The data obtained from the TEM observation shows no reduction of T_0 value for all samples grown at different temperature, which means that all supplied Ga atoms were incorporated in the crystal without desorption.

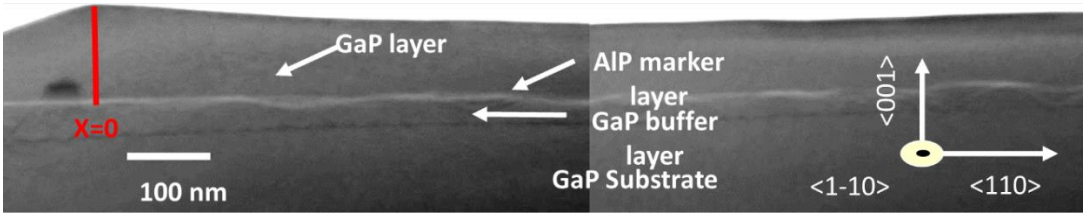

Figure 4.6 Cross sectional TEM image of GaP along <110> direction on the edge of a stripe growth at 600 °C

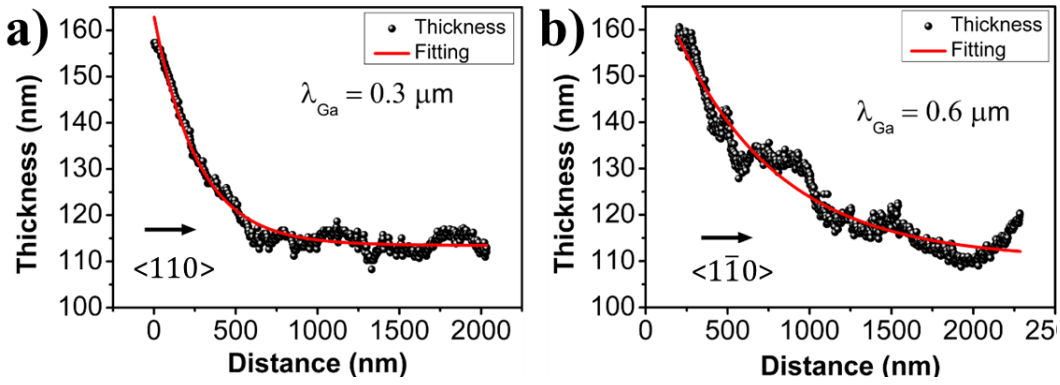

Figure 4.7 Measured thickness as a function of the distance for the two directions a) $< 110 >$ and b) $< 1\bar{1}0 >$, the fitting line was obtained from the one-dimensional growth model, the sample was grown at 600 °C.

Table 4-1 Diffusion length values for different growth temperatures and crystal directions.

Growth Temperature (°C)	$< 110 >$ direction (µm)	$< 1\bar{1}0 >$ direction (µm)
500	0.11	0.06
550	0.23	0.31
600	0.27	0.63
650	0.75	1.7

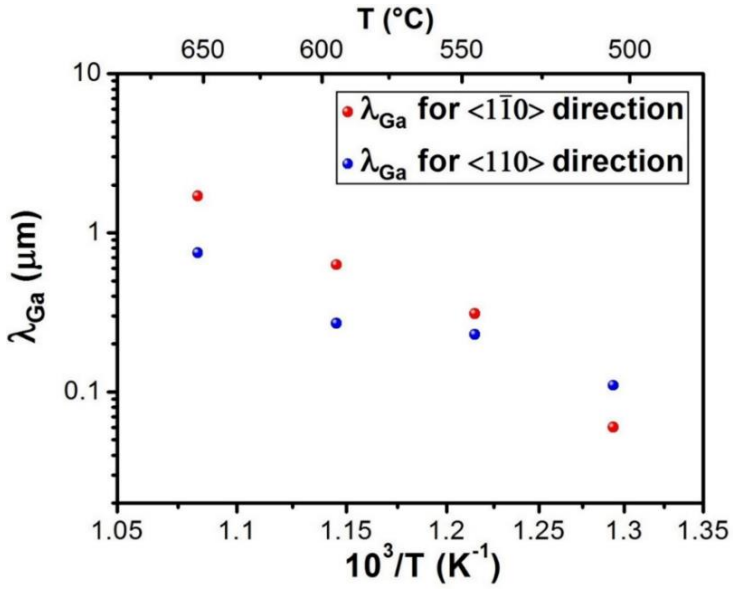

Figure 4.8 Diffusion length versus 1/T for the different growth temperatures along $< 110 >$ and $< 1\bar{1}0 >$ directions. The inversion of the anisotropy indicates a similar diffusion length at both directions around 535 ºC.

4.5.3 AFM measurements

All the samples were measured by AFM, at standard growth conditions the GaP shows a peculiar morphology which consist in small oval shaped islands. Figure 4.9 shows AFM images grown at the different temperatures. The RMS value was ranged from 0.15 nm to 1.54 nm. This roughness was a negligible value for the estimated thickness distribution near the boundary as it was shown in the Figure 4.7. The size of the growth shows a tendency to increase its size with the temperature and finally reach a step and terrace structure. For the samples grown at 550 °c and 600 °C, oval shaped islands elongated along the $< 1\bar{1}0 >$ direction as shown in Figure 4.9 (b) and (c) respectively, this orientation shown by the green line in Figure 4.9 corresponds to the direction in which the longer diffusion length was obtained. For the sample grown at 500 °C, the orientation of the oval shaped islands is not clearly defined since the islands are too smalls and there´s no uniform size as observed in Figure 4.9 (a). Since the substrate has an unintentional offset angle below 0.5°, a step and terrace structure would be formed when the adatom diffusion length was longer than the average terrace width of the substrates like the one observed in Figure 4.9 (d) These steps are aligned perpendicular to the $< 1\bar{1}0 >$ direction although for this sample those steps and not entirely regular.

Figure 4.10 plots the island size for the $< 110 >$ and $< 1\bar{1}0 >$ directions as a function of the diffusion length. The size of the islands was obtained using Gwyddion software by measuring them along both directions of the individual islands and considering the mean value. The value for the $< 110 >$ direction ranged from 55.9 nm to 181.4 nm and for the $< 1\bar{1}0 >$ direction it ranged from 50.9 nm to 415.2 nm as shown in the Table 4-2. The results show the correlation between the island size and the diffusion length with a correlation coefficient of 0.95 and 0.99 for $< 110 >$ and$< 1\bar{1}0 >$ direction, respectively.

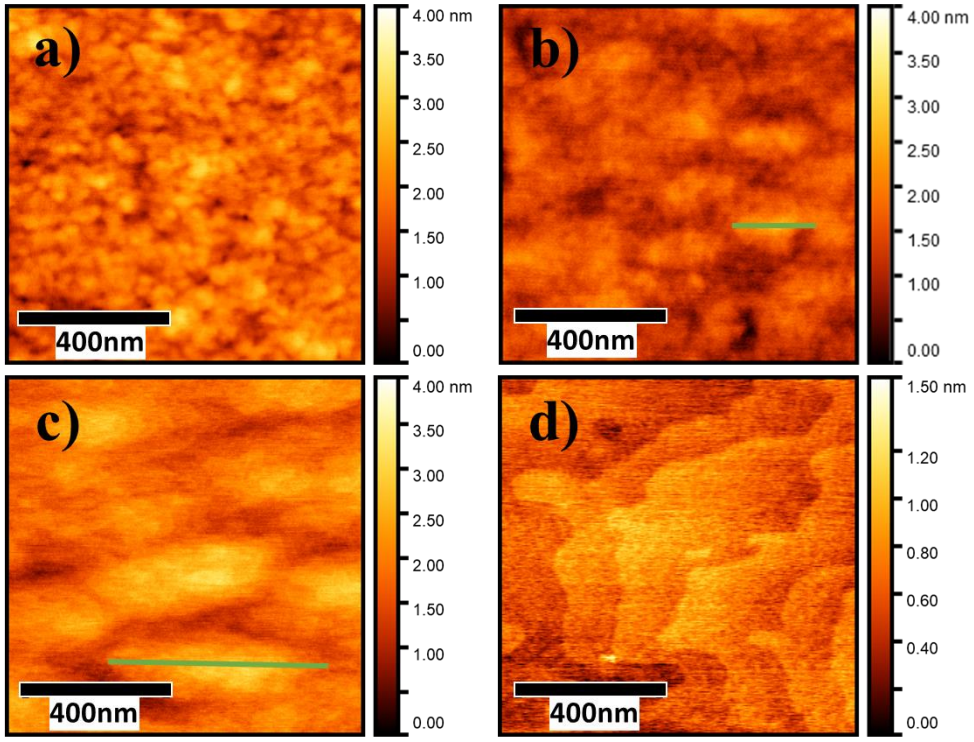

Figure 4.9 AFM 1×1 μm^2 images of the GaP surface grown at a) 500 °C, b) 550 °C, c) 600 °C and d) 650 °C, oval shaped islands are observed for the samples grown from 500 °C to 600 °C, in these conditions the orientation of the island is indicated by the green line. The image of the GaP surface grown at 650 °C exhibits a step flow growth. The horizontal direction corresponds to the $< 1\bar{1}0 >$ direction and the vertical to the $< 110 >$ direction.

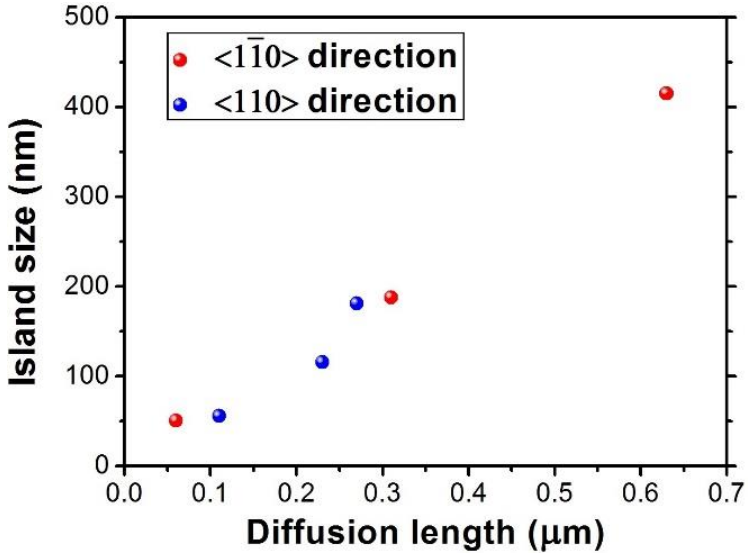

Figure 4.10 Island size as a function of the diffusion length for the $< 110 >$ and the $< 1\bar{1}0 >$ directions of the samples grown from 500 °C to 600 °C.

Table 4-2 Island size along both directions for the different growth temperatures.

Growth Temperature (°C)	Island size along $< 110 >$ direction (µm)	Island size along $< 1\bar{1}0 >$ direction (µm)
500	56	52
550	116	188
600	181	415

4.5.4 Migration enhanced epitaxy (MEE)

Due to the formation of crystal defects during the heteroepitaxy of GaP/Si many efforts have been dedicated to the understanding of the generation of these defects, it has been shown that to reduce the formation of stacking faults and misfit dislocations a GaP layer on Si grown by MEE is very effective[53], [97]. MEE growth is performed by the alternately supply of the III and V atoms, this procedure promotes the diffusion of the group III adsorbents since they do not react until the Group V elements are supplied again. The growth of GaP by MEE is usually done from 450 ºC to 500 ºC. A sample was grown by MEE to evaluate the diffusion length by this method. The sample was grown on an epiready GaP (001) substrate with the same growth conditions of the stripped structure and buffer layer of the ones employed for the samples grown by MBE. A 100nm thick GaP layer was grown at 500 ºC, with a growth rate of 0.15 µm/h with a Ga flux of $2.19 \times 10^{-5} Pa$.

In the Figure 4.11 it shown the measurement of the thickness and fitting of the sample grown by MEE for the $< 110 >$ and $< 1\bar{1}0 >$ directions, the diffusion lengths were estimated from the fitting to the one-dimensional diffusion model as 1600 nm and 1200 nm for the $< 110 >$ and $< 1\bar{1}0 >$ directions, respectively. Two main differences were observed, first is the magnitude of the diffusion lengths compared with MBE growth, by MEE growth diffusion lengths are more than one order of magnitude longer, and second is the anisotropy, here diffusion length at $< 1\bar{1}0 >$ direction is shorter than the diffusion length for $< 110 >$, this is also different from the general tendency of the MBE growth.

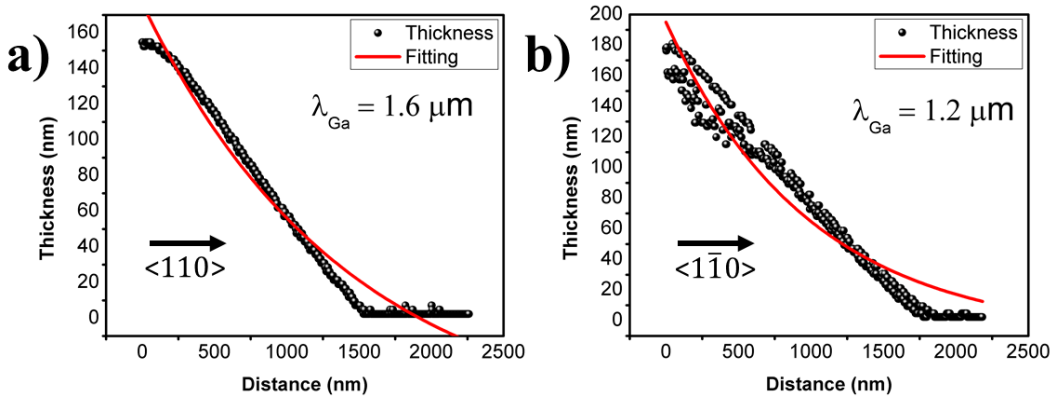

Figure 4.11 Measured thickness as a function of the distance for the two directions a) $< 110 >$ and b) $< 1\bar{1}0 >$, the fitting line was obtained from the one-dimensional growth model, the sample was grown at 500 °C.

In the Figure 4.12 it is shown the AFM 1×1 μm^2 images for samples grown at 500 ºC by (a) MBE and (b) MEE growth modes. In the MBE growth islands did not have a clear orientation due to the small sizes of it, but for MEE growth the islands are orientated preferentially in the $< 1\bar{1}0 >$ direction. Also, the sizes are longer than the MBE islands, this is expected since the diffusion lifetime in MEE is longer. Comparing with MBE growth, the anisotropy in the diffusion lengths is related with the morphology of the islands, and the longer diffusion length leads the orientation of the oval shaped islands, in case of MEE this is not happening, and the situation seems to be the opposite. The average size of the MEE islands is 70 nm and 140 nm for the $< 110 >$ and $< 1\bar{1}0 >$ directions, respectively, it is possible to estimate the diffusion lengths from the islands size or vice versa, by estimating the diffusion lengths from the islands sizes from the linear behavior presented in the Figure 4.10, the obtained values are completely different from the measured ones, for example, estimated diffusion lengths are 102 nm and 233 nm for the $< 110 >$ and $< 1\bar{1}0 >$ directions, respectively. This is due to the influence of the striped structure employed. In the Figure 4.13 it is shown the TEM cross-section images of the stripes edges employed in the measurements of the diffusion lengths, for the case of the $< 110 >$ direction, the (111)a plane is located next to the growth surface, since this is a Ga ending surface, during the supply of the Ga atoms this are not easily incorporate and diffusion to (001) is predominant. On the other side for the $< 1\bar{1}0 >$ direction, the (111) b plane is located next to the growth surface, this is an As ending surface where the absorption of Ga adatoms easily occurs. Since the one-dimensional growth model consider diffusion from adjacent planes producing dominant diffusion in one direction, due to the alternated atoms supply of the process and the polar nature of the (111) planes the one-dimensional growth diffusion model is not suitable for the estimation of diffusion lengths during MEE growth. For diffusion length measurement by MEE growth future reconsideration of the model should be done.

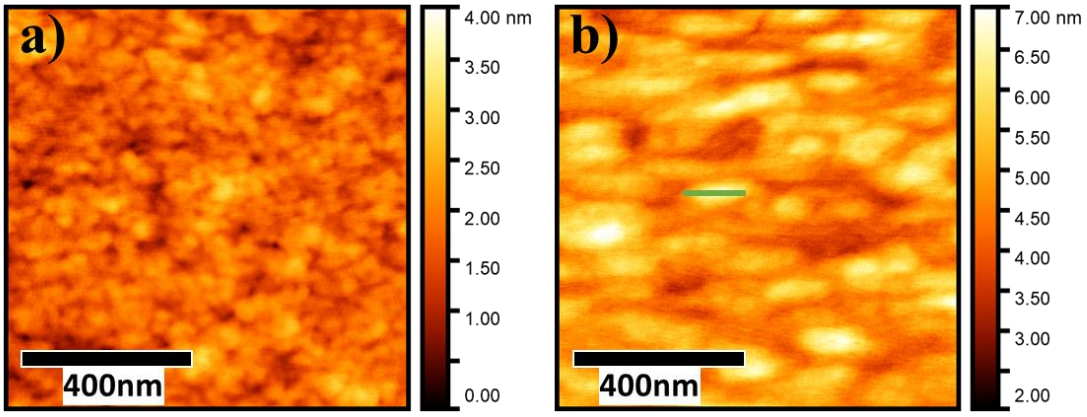

Figure 4.12 AFM 1×1 μm^2 images of the GaP surface grown at 500 °C by a) MBE, and b) MEE growth mode. Oval shaped islands are observed for the samples, in these conditions the orientation of the island is indicated by the green line for MEE growth. The horizontal direction corresponds to the $< 1\bar{1}0 >$ direction and the vertical to the $< 110 >$ direction.

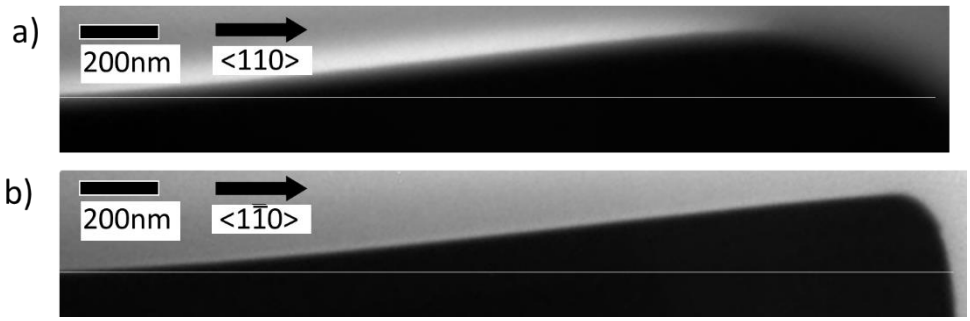

Figure 4.13 Cross sectional TEM image of GaP on the edge of the stripes used for the diffusion lengths measurement, grown at 500 ºC by MEE along a) <110> and b) $< 1\bar{1}0 >$ direction.

4.5.5 Discussion

It is noted that these AFM results are correlated with the behavior of the diffusion length as a function of the temperature as shown in Figure 4.8. The island size was strongly dependent on the diffusion length as expected and present a clear tendency as shown in Figure 4.10. In addition, elongation of the grown island along the $< 1\bar{1}0 >$ direction is also consistent with the larger diffusion length along $< 1\bar{1}0 >$ than $< 110 >$ direction at 550 °C and 600 °C. The correlation is also observed in the sample that exhibits the step flow growth with steps aligned perpendicular to the $< 1\bar{1}0 >$ direction as mentioned by Ratcliff et al.[50]. In step flow growth the formation of irregular steps can be attributed to the difference in the diffusion lengths due to a bigger incorporation of adatoms in the perpendicular direction of the steps producing the early stage of island formation. The irregular steps observed in the sample grown at 650 °C, are evidence of a longer diffusion length along the $< 1\bar{1}0 >$ direction. Since the diffusion length values are small and hence the size of the islands is small at 500 °C it is not possible to determinate the orientation. In the case of the GaAs (001) surface, for the $\beta_2(2 \times 4)$ surface reconstruction it was suggested that a directional anisotropy in the effective diffusion barriers exists, which results in longer diffusion lengths along the $< 1\bar{1}0 >$ direction. Similarly, 2×4 surface reconstruction was observed in this work and this behavior matches the measurement of the diffusion length values for the samples grown at 550 °c and 600 °C. The change in the diffusion length anisotropy at 500˚C during MBE growth seems to be related to the surface reconstruction as observed by RHEED patterns, been a 2x1 for 500˚C and 2x4 for the rest of the temperatures.

For MEE growth, AFM results shows oval shaped islands elongated towards the $< 1\bar{1}0 >$ direction on the surface suggesting directional anisotropy of adatom diffusion. The estimations of the diffusion lengths in this type of growth were not conclusive due to the differences in the process compared with MBE. By extrapolating the results obtained from MBE growth, diffusion lengths are expected between 100 nm and 200nm. These preliminary results suggest that the behavior is like MBE growth at higher temperatures.

This directional anisotropy may be informative to understand key growth processes in some cases, i.e., annihilation of APD. In the APD region, crystallographic orientation is rotated at 90° along the $< 001 >$ direction compared to the main domain. At the antiphase boundary of the grown surface, incorporation of Ga adatoms diffused along the $< 110 >$ compete with those diffused along the $< 1\bar{1}0 >$ direction. In such a case, adatom diffusion length will affect the shape of the APD or result in a self-annihilation process. Lin et al.[48], investigated the effects of V/III flux ratio and growth rate on the propagation and annihilation of

antiphase boundaries of GaP on Si by a two-step growth process. Since the orientation of GaP grown on Si (001) depends on the occupation of either Ga or P atoms in the zincblende sublattice, the lack of site occupation preference for Ga will give rise to the formation of antiphase domains. They found that increasing growth rate suppressed Ga adatom diffusion that leads to a more uniform growth rate for the APD and main domain regions, which leads to the apparition of more antiphase domains at the end of the growth. Low growth rate allows that the diffusion length of the Ga adatom become significant enough to produce GaP growths with the correct orientation and fewer APDs. In this work the anisotropy is clearly present with a growth temperature 600 ºC and higher for MBE growth. For 500 ºC diffusion lengths also exhibit directional anisotropy, but the AFM images does not clearly show this behavior, this may be due the small diffusion lengths. Despite the incongruent results between islands size and diffusion lengths, the AFM clearly shows the directional anisotropy needed for the self-annihilation of APDs at 500 ºC by MEE growth. The reversal in the diffusion length anisotropic values at 500 ºC by MEE seems to be related to the one-dimensional diffusion model and should be taken with caution, and for MBE seems to be related to the change in surface reconstruction.

4.6 Summary

Diffusion length of adatom on the grown surface is one of the decisive factors to understand the growth mechanism. In this work the diffusion length of Ga was estimated by using a one-dimensional diffusion growth model and their temperature dependence was discussed on two principal axes by MBE. It is quantitatively clarified that the diffusion length of the Ga adatoms increased with the growth temperature. Directional anisotropy in the diffusion length was observed along the $< 110 >$ and $< 1\bar{1}0 >$ directions. This anisotropy was highly consistent with the surface morphology i.e., elongation of the growth island along the $< 1\bar{1}0 >$ direction is also consistent with the larger diffusion length value along $< 1\bar{1}0 >$ direction.

It can be concluded that the GaP (001) exhibits a similar diffusion mechanism as the GaAs (001) for some growth conditions. The diffusion length in GaP is related to the morphology of the islands and the orientation of this islands it´s determined by the longer value for the diffusion length. For growth temperature of 550 °C and 600 °C it seems that the diffusion mechanism is affected by the interaction of Ga adatom and the dimers of the (2×4) surface reconstruction. At lower temperatures, the diffusion mechanism changes since surface reconstruction changes, for the growth temperature of 650 °C it was observed a change in the surface reconstruction although the relation between λ_{Ga} along $< 1\bar{1}0 >$ is larger than λ_{Ga} along $< 110 >$ was preserved. To help with the self-annihilation of APDs a growth temperature of 600 ºC or higher is desire.

For MEE growth the one-dimensional diffusion growth model is not appropriate to estimate the diffusion lengths. Despite this, the results obtained from the study through MBE growth and the AFM results suggest that at 500 ºC directional anisotropy is achieved, been good conditions for the APD reduction.

With the estimation of diffusion lengths by island formation is possible to find growth conditions in which diffusion anisotropy is present in order to increase the antiphase domains self-annihilation during GaP/Si heteroepitaxy.

Chapter 5 InP QDs morphology and vertical alignment

5.1 InP growth

To achieve the carrier spatial separation proposed for III-V-N photovoltaics, the successfully InP QDs in the GaAsPN matrix growth should be achieved. Due to the lack of information about these materials a starting point is the optimization of growth conditions for the InP QDs in a GaP matrix and later good quality stacking of a InP QDs in a GaP matrix, good crystal quality is required for the QDs, with this in mind, first, the growth conditions of the InP homoepitaxy were investigated.

5.1.1 InP homoepitaxy

Growth conditions of InP homoepitaxy were investigated, including growth temperatures and the V/III ratio with the purpose of obtaining a flat and free defect surface. The growth temperatures ranged from the 350 °C to 480 °C, also the growth rate studied was 15, 30 and 45. The samples grown consisted of a 50nm thick InP layer, before the deposition of the InP a thermal cleaning was performed on the InP (001) epiready substrates at 500 °C for 5 min. in a P overpressure environment. The In Beam Equivalent Pressure (BEP) measured for this samples were 2.19×10^{-5}Pa.

To investigate the thermal cleaning of the InP epiready substrate, the temperature was increased to almost 540 ºC. During this experiment it was observed that around 520 °C the desorption of the InP layer drastically increased. This was observed in an abrupt change in the RHEED pattern, which changed from a streaky pattern to a spotty and much less intense pattern, been a clear sign of crystal quality degradation. Suggesting that the highest possible growth temperature for the InP can be found around 500 °C, although even this temperature could be too high for a flat epitaxial layer due to the continuous desorption of adatoms.

The growth temperature range was investigated from 350 ºC to 450 ºC, employing a V/III ratio of 15 and 30. In the Figure 5.2 and Figure 5.3. $10 \times 10\ \mu m$ AFM images are shown for the 15 and 30 V/III ratio, respectively. In all these samples a smooth surface was not achieved, defects are present in all the samples including small surface defects and larger defects of more than 5 μm diameter as shown in Figure 5.2 (c). Despite the larger defects at 450 ºC the rest of the surface showed an improvement suggesting that longer adatom diffusion would improve the overall morphology. Higher V/III ratio also presented an improvement.

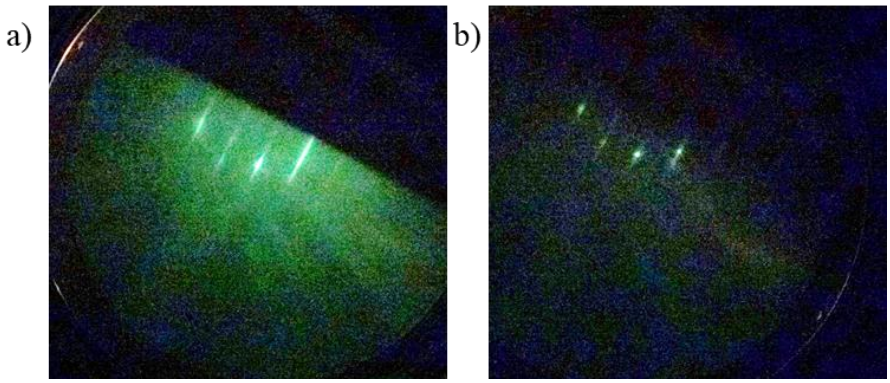

Figure 5.1 RHEED pattern of InP homoepitaxy for the $< 110 >$ direction, a) was taken around 400 °C and b) after exceeding 520 °C.

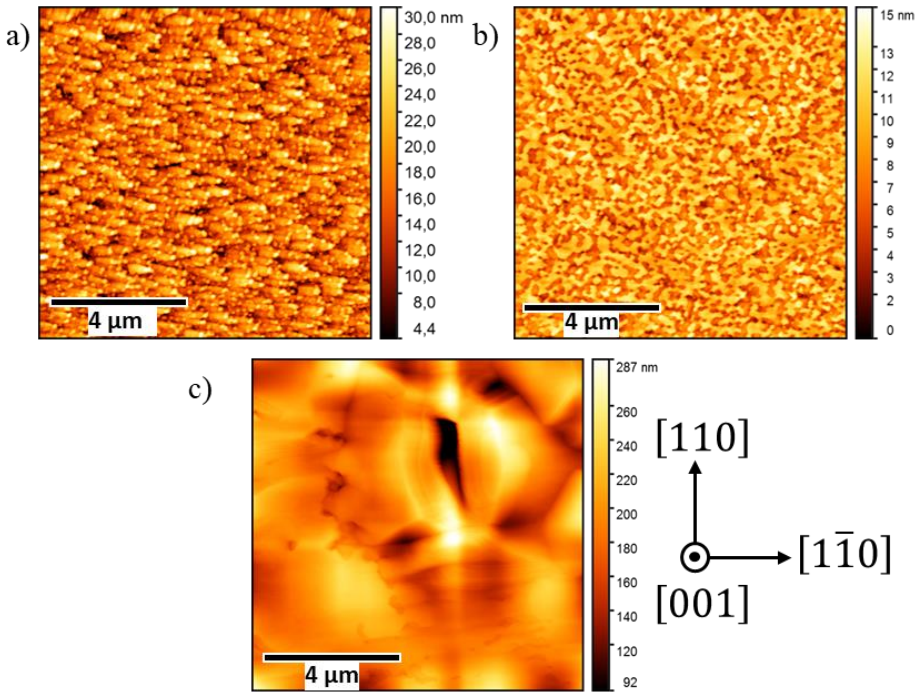

Figure 5.2 $10 \times 10\ \mu m$ AFM image of 50nm InP layer with $\frac{V}{III} = 15$ grown at a) 350 °C, b) 400 °C, and c) 450 °C. with RMS of 4.4 nm, 2.3 nm, and 31.7 nm, respectively. Here the horizontal orientation of the image corresponds to the $< 1\bar{1}0 >$ direction and the vertical to the $< 110 >$ direction as indicated; this orientation will be used in all the AFM images unless something else is mentioned.

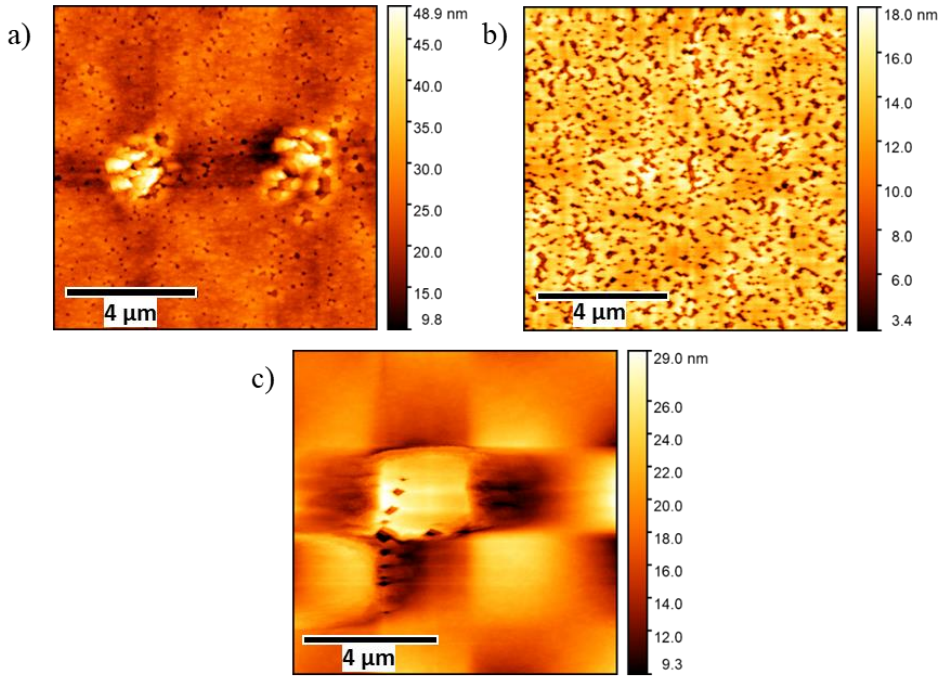

Figure 5.3 $10 \times 10\ \mu m$ AFM image of 50nm InP layer with $\frac{V}{III} = 30$ grown at a) 350 °C, b) 400 °C, and c) 450 °C. with an RMS of 4.5 nm, 2.8 nm, and 3.4 nm, respectively.

Another set of samples was investigated with a V/III ratio of 45, for the growth temperatures of 400 °C, 450 °C and 480 °C. Due to the previous results the temperature was increased to 480 ºC. In the Figure 5.4 we can observe $10 \times 10\ \mu m$ AFM images. A significant improvement was made for these growth conditions with the elimination of larger size defects.

Table 5-1 RMS value in nm for the InP homoepitaxial layers for all the different growth conditions, Two different areas are presented for each sample, $10 \times 10\ \mu m$ are consider the influence of the larger size defects while $1 \times 1\ \mu m$ area do not.

	RMS (nm)					
Growth Temperature (°C)	$\frac{V}{III} = 15$		$\frac{V}{III} = 30$		$\frac{V}{III} = 45$	
	$10 \times 10\ \mu m$	$1 \times 1\ \mu m$	$10 \times 10\ \mu m$	$1 \times 1\ \mu m$	$10 \times 10\ \mu m$	$1 \times 1\ \mu m$
350	4.4	2.9	4.5	1.2	-	-
400	2.3	1.2	2.8	2.3	11	8.6
450	31.7	0.4	3.4	0.2	0.4	0.1
480	-	-	-	-	0.2	0.1

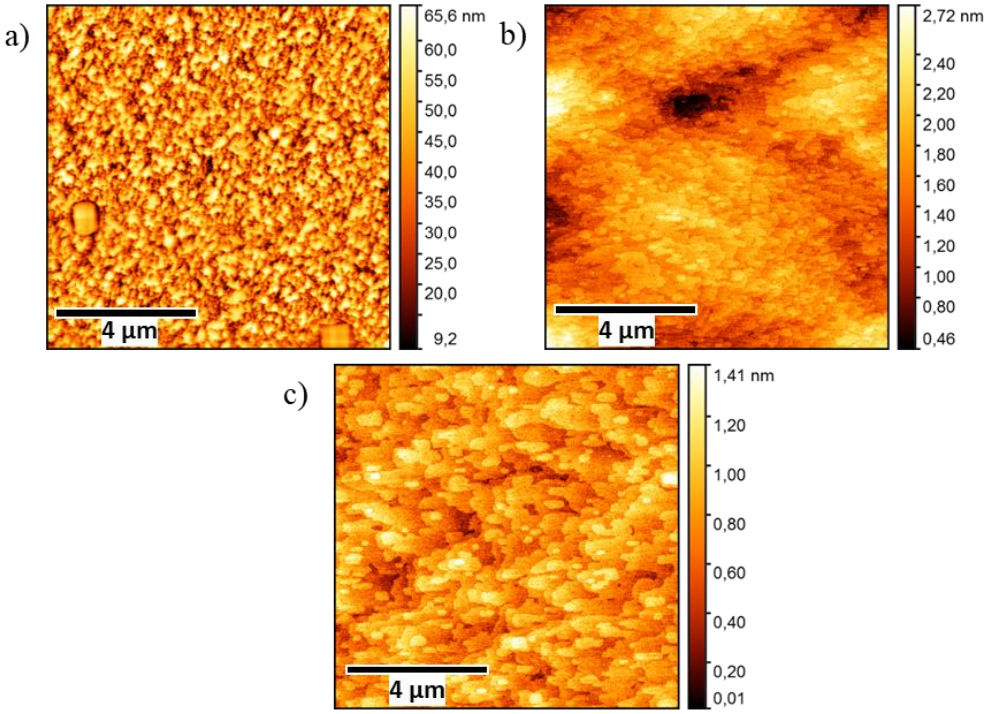

Figure 5.4 $10 \times 10\ \mu m$ AFM image of 50nm InP layer with $\frac{V}{III} = 45$ grown at a) 400 °C, b) 450 °C, and c) 480 °C. with an RMS of 11 nm, 0.4 nm, and 0.2 nm, respectively.

The data obtained from the AFM measurements is summarize in the Table 5-1. As the temperature increase the RMS value decrease, similarly for the V/III ratio. This information shows that the lowest RMS between all the samples is obtained at the highest temperature and the highest V/III ratio. In the table two values are shown, for each sample the RMS was measured for $10 \times 10\ \mu m$ and $1 \times 1\ \mu m$ surface area, the bigger area considered the influence of the larger size defects. This means that when the differences on the two different values exceed one order of magnitude this sample presented large size defects. As the Figure 5.4 shows in the sample with the lowest RMS value a step-flow like growth is achieved, also for the $V/III = 45$ and 480 ºC larger size defects are not observed. The flat surface was also observed by the streak RHEED patterns observed during the growth, corresponding to a (2×4) reconstruction. With these conditions it is expected to obtain coherent InP QDs.

5.1.2 InP Quantum dots morphology

5.1.2.1 Temperature dependence

After obtained the optimized conditions for the InP epitaxial layer, the formation of the quantum dots was investigated the first parameter investigated was the growth temperature. As in the InP homoepitaxial layer experiments the growth temperature plays a significant role in the dynamics of the growth.

In the next experiments an InP layer with nominal 2.3ML thickness was grown above a 100 nm thickness GaP layer, a $V/III = 45$ was employed with a 0.033ML/s growth rate with an In flux of 8.56×10^{-6}Pa. the GaP layer was grown with a $V/III = 4$ and a Ga flux of 4×10^{-5} Pa with a growth temperature of 600 °C and a 0.3µm/hr. growth rate, a 10min. thermal treatment is applied at 700 °C after the introduction of the sample. The growth temperature was ranged from 400 °C to 500 °C.

Under all the growth temperature conditions quantum dots were obtained. In the Figure 5.5 an example of the quantum dots obtained is shown with an average height of 2.5 nm. In this case homogenous size distribution was not achieved, large islands and small islands coexist, only the 500 ºC is formed only by large islands. It was possible to observe QDs with height ranged from 2 nm to 20 nm. For the growth temperature of 500 °C a much less density of quantum dots was observed, the high temperature seems to increase the mobility of adsorbed atoms and Ostwald ripening occurs which causes the disappearance of the small quantum dots and leave only the biggest quantum dots as shown in the Figure 5.5

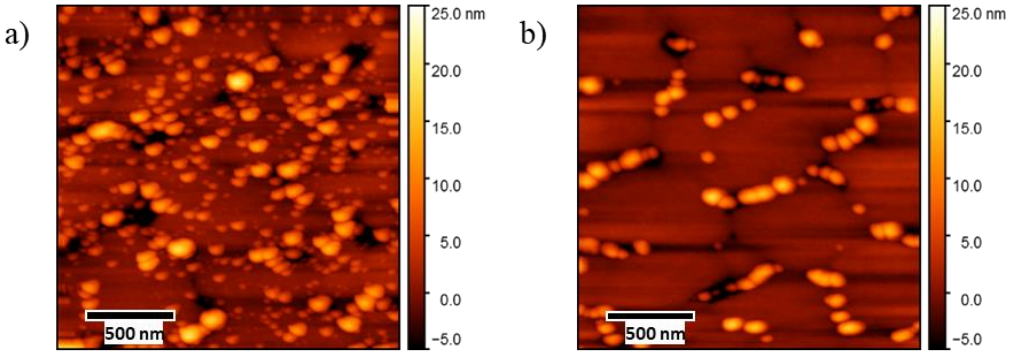

Figure 5.5 $2 \times 2\ \mu m$ AFM images of the quantum dots sample grown at a) 420 °C, and b) 500 °C.

To measure the average height and density of the quantum dots the Gwyddion software was employed using the segmentation algorithm for the selection of the quantum dots. In the Figure 5.6 the density is plotted with the Growth temperature dependence. Two different parameters in the algorithm for the measurements were employed due to the average size value been close to the minimal discernible value, This allows to distinguish between smaller and bigger QDs, with the restriction only the bigger QDs will be consider and without the restriction both smaller and bigger QDs are considered. Both measurements exhibit a similar behavior in the graph, the density seems to remain constant with the temperature dependence until reaching the 480 °C in the growth temperature. From this value on the density abruptly decrease.

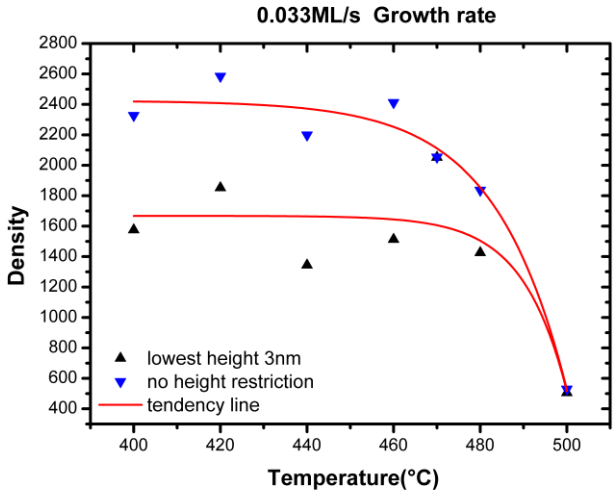

Figure 5.6 Density vs. Growth temperature of the quantum dots samples. The two different measurements correspond to the algorithm employed in the software, the black triangle consider the lowest height as 3 nm and the inverted triangle (▼) did not consider any height restriction.

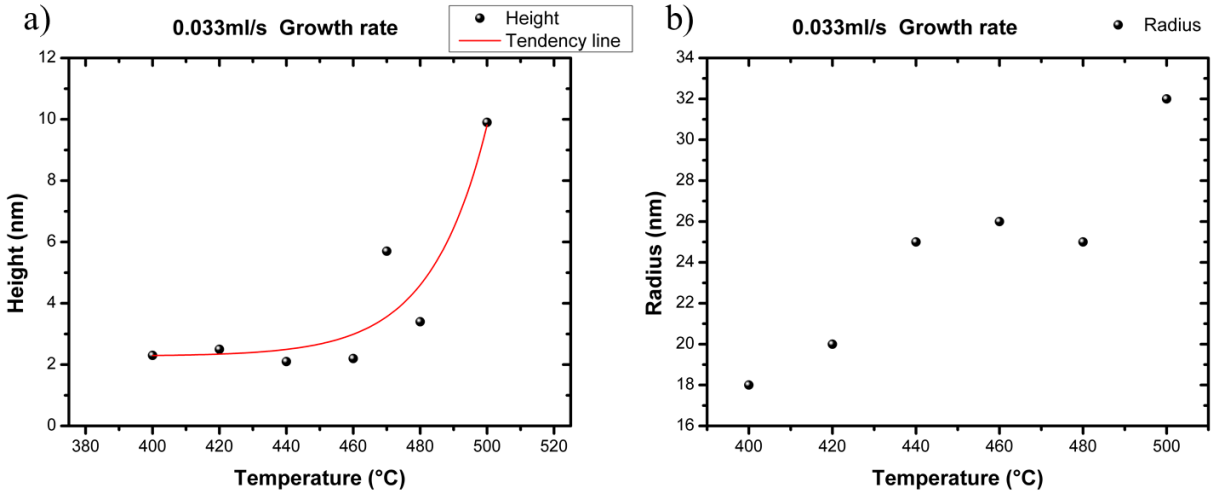

Figure 5.7 a) Height vs. Growth temperature plot of the quantum dots, the red line is the tendency line obtained. b) Radius vs. growth temperature.

As mentioned before after 480 °C in the growth temperature the mobility of the adsorbed atoms increases, at 500 ºC the highest values were obtained. This causes an alteration in the growth dynamics and coarsening becomes significant, decreasing the density and increasing the overall dimensions of the quantum dots. This can be observed in the Figure 5.7, the height remained at similar values until 460, after that it increased with the temperature, radius increase with the temperature.

Since the goal is to achieve QD in a GaAsPN matrix. 480 ºC of growth temperature is the most suitable because GaAsPN typical growth temperature is higher than 500 ºC, so the highest temperature is preferred, and since for 500 ºC a very strong dependence on the QD coarsening was observed, 480 ºC is a more stable condition.

5.1.2.2 Growth rate and V/III ratio dependence

The next parameter to investigate is the growth rate. Previous samples were grown at a constant 0.033ML/s. The samples had an InP layer with nominal 1.8ML thickness grown at 480 °C, it was grown above a 100 nm thickness GaP layer. The V/III ratio of 45 was employed with an In flux of 5.97×10^{-6}, 1.19×10^{-5}, 2.39×10^{-5}, 5.97×10^{-6} for the conditions studied are 0.025ML/s, 0.05ML/s, 0.1ML/s and 1.5ML/s, respectively. The GaP layer was grown with a $V/III = 45$ and a Ga flux of 4×10^{-5} Pa with a growth temperature of 670 °C and a 0.3µm/hr. growth rate. The AFM images are shown in the Figure 5.8 and the size distributions in the Figure 5.9. These distributions consider only the bigger QD, since it is expected that these type of QDs will produce the stacking.

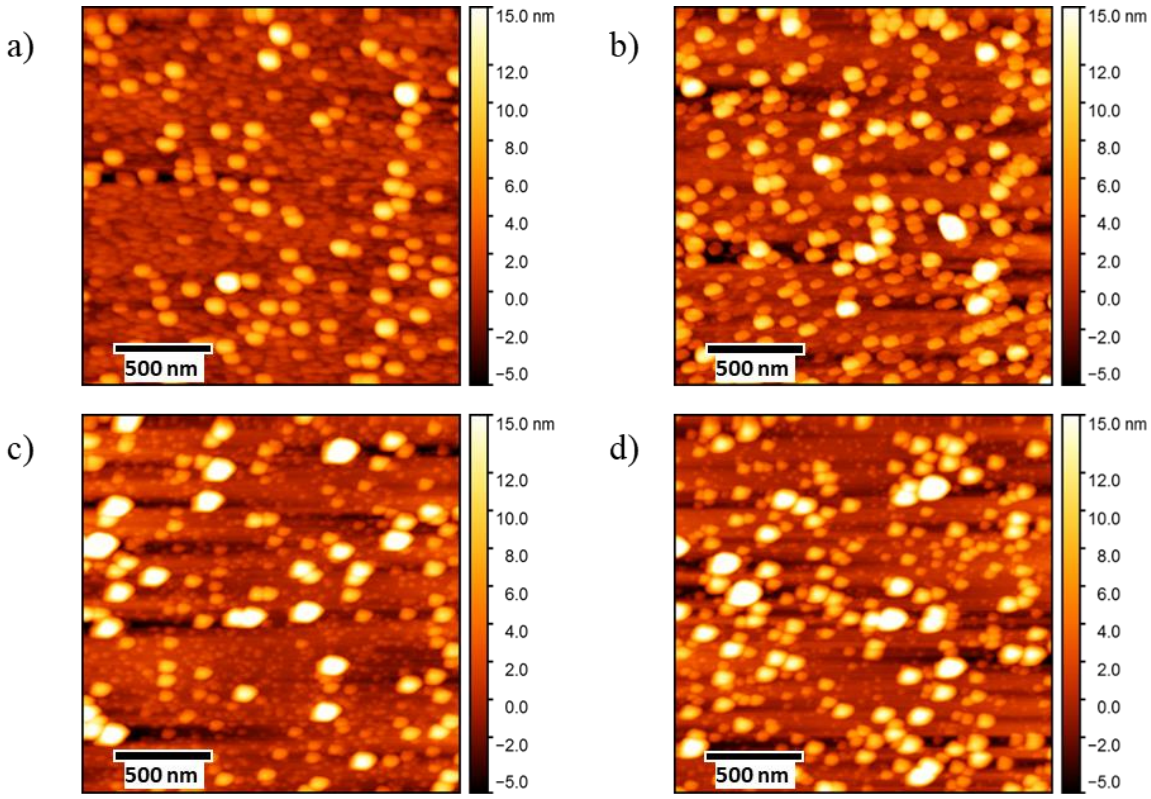

Figure 5.8 $2 \times 2\ \mu m$ AFM images of the quantum dots sample grown at 480 °C with a a) 0.025ML/s, b) 0.05ML/s, c) 0.1ML/s, and d) 0.15ML/s.

Table 5-2 Mean height and FWHM of the larger quantum dots for the different growth rates.

Growth rate (ml/s)	Mean height (nm)	FWHM (nm)
0.025	5.2	5.4
0.05	6.5	6.6
0.1	5.2	7.4
0.15	5.7	6.11

The values of the FWHM and mean height are shown in the Table 5-2, a normal distribution consisted of one peak was considered. For higher growth rate the distribution resembles a multimodal behavior as shown in the Figure 5.9 (c) and (d). From these experiments a more uniform size distribution of the QDs achieved at low growth rate was observed. Despite this low growth rate QDs with height superior at 10 nm remains.

By observing the RHEED pattern after the formation of the quantum dots, the angle of the chevrons was measured, which suggest that pyramidal quantum dots with (112) facets are forming as shown in the Figure 5.10, the RHEED pattern measurement conditions were not optimate since an overlap between the GaP streak pattern is observed, this may lead to a slightly change in the pattern observed.

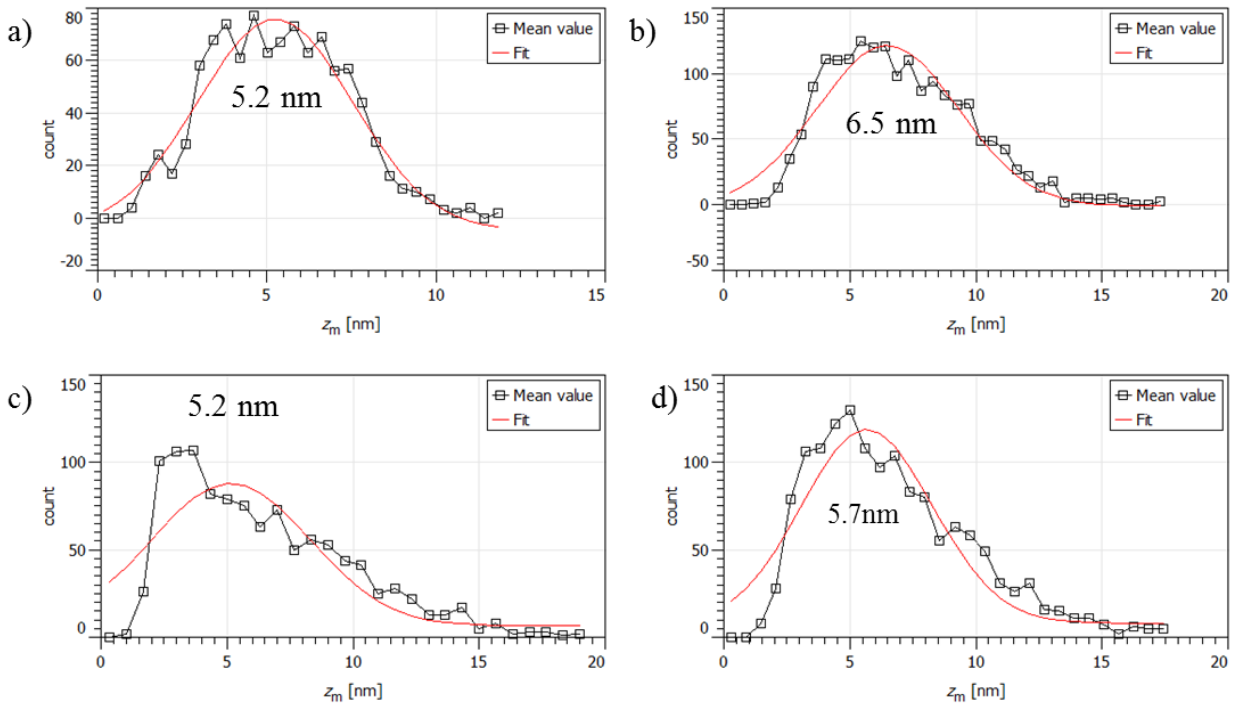

Figure 5.9 Mean height of the quantum dots for a) 0.025ML/s, b) 0.05ML/s, c) 0.1ML/s, and d)1.5ML/s growth rate. The red line is the fitted data.

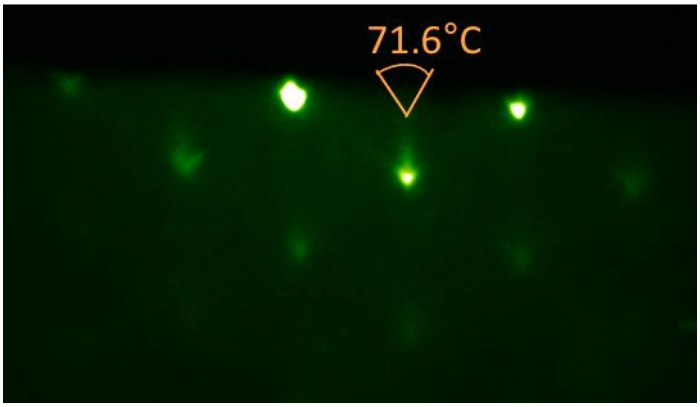

Figure 5.10 RHEED pattern along the $< 110 >$ direction showing the formation of chevrons, which is a clear indication of quantum dots formation.

To perform the stacking of QDs, samples were analyzed by TEM cross-sectional view. The sample shown in the Figure 5.11 with growth conditions for the InP layer are 480 °C of growth temperature, V/III = 45, In flux of 1.19×10^{-5} Pa and 1.8 ML thickness. Different size and shaped QDs were observed, like the AFM measurements presented. The generation of stacking faults occurred in larger QDs with height bigger than 8 nm as displayed in (a). Which confirmed the multimodal distribution growth and the importance of smaller size QDs. Samples with the purpose of studying capping and stacking of the QDs were prepared. In this samples the formation and propagation of structural defects occur mainly on the larger QDs (this will be presented in the following section5.2.2).

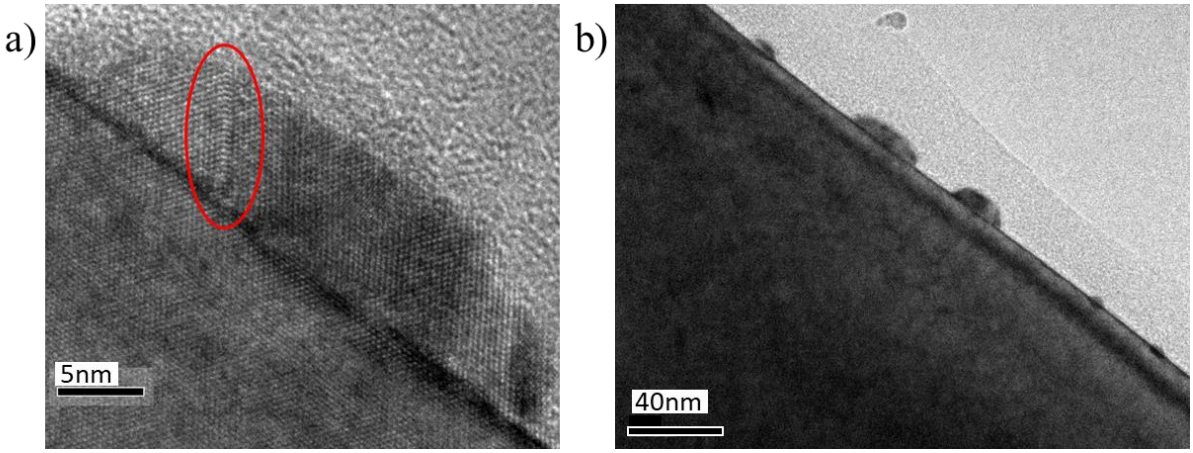

Figure 5.11 Cross-sectional TEM image under bright field conditions of uncapped quantum dots, (a) stacking fault was observed in this 8nm height QD. (b) QDs of multiple sizes.

Good crystal quality is required for stacking structure, since defects are being generated within the larger QDs this type of QDs are not desirable for the present purpose. To prevent the generation of this defects a smaller quantum dots are desirable.

To achieve free defect QDs, the V/III ratio was studied from 10 to 45, the dependence of the growth rate was also studied. The next samples had an InP layer with nominal 1.8 ML thickness grown at 480 °C, it was grown above a 100 nm thickness GaP layer.

In the Figure 5.12 and Figure 5.13 the z-scale range from -5 to 15 nm and in the Figure 5.14 from -1.5 to 3nm. This due the difference on QD size. In the Figure 5.15 the relevant data is summarized to compared between the different parameters, the z-color scale ranges from -5 to 15 nm indicated by the green shaded images, but the blue shaded images range from -1.5 to 3 nm. As the growth rate and/or V/III ratio increases, large InP islands with heights exceeding 10 nm appear. Even if large islands are formed, small islands coexist. The uniformity of InP QDs was improved by reducing both the growth rate and V/III ratio. Since the large island was already relaxed by introducing a misfit dislocation, I focused on small islands. For almost all samples, at least two types of islands can be seen in the blue shaded AFM images, in which the z-range is smaller than the other conditions. Here, I categorize them by the height QDs, that is, smaller-height as type-A, and bigger one as type-B. To determine the initial stage of InP island formation and the size change, the distribution of islands was measured from the AFM images. In Figure 5.16, the height distribution of the sample grown at a growth rate of 0.15 ML/s with a V/III ratio of 10 is presented. A multimodal distribution is observed, where the first peak is located around 2.5 nm, corresponding to the type-A QDs and a second peak around 5.3 nm for the type-B QDs. This multimodal distribution was also observed in plan-view TEM measurements for GaP capped QDs as previously mentioned. Type-A QDs are more common than type-B QDs, with low growth rates and small V/III ratios, the nucleation of the larger islands can be reduced, and the type-A QDs are predominant.

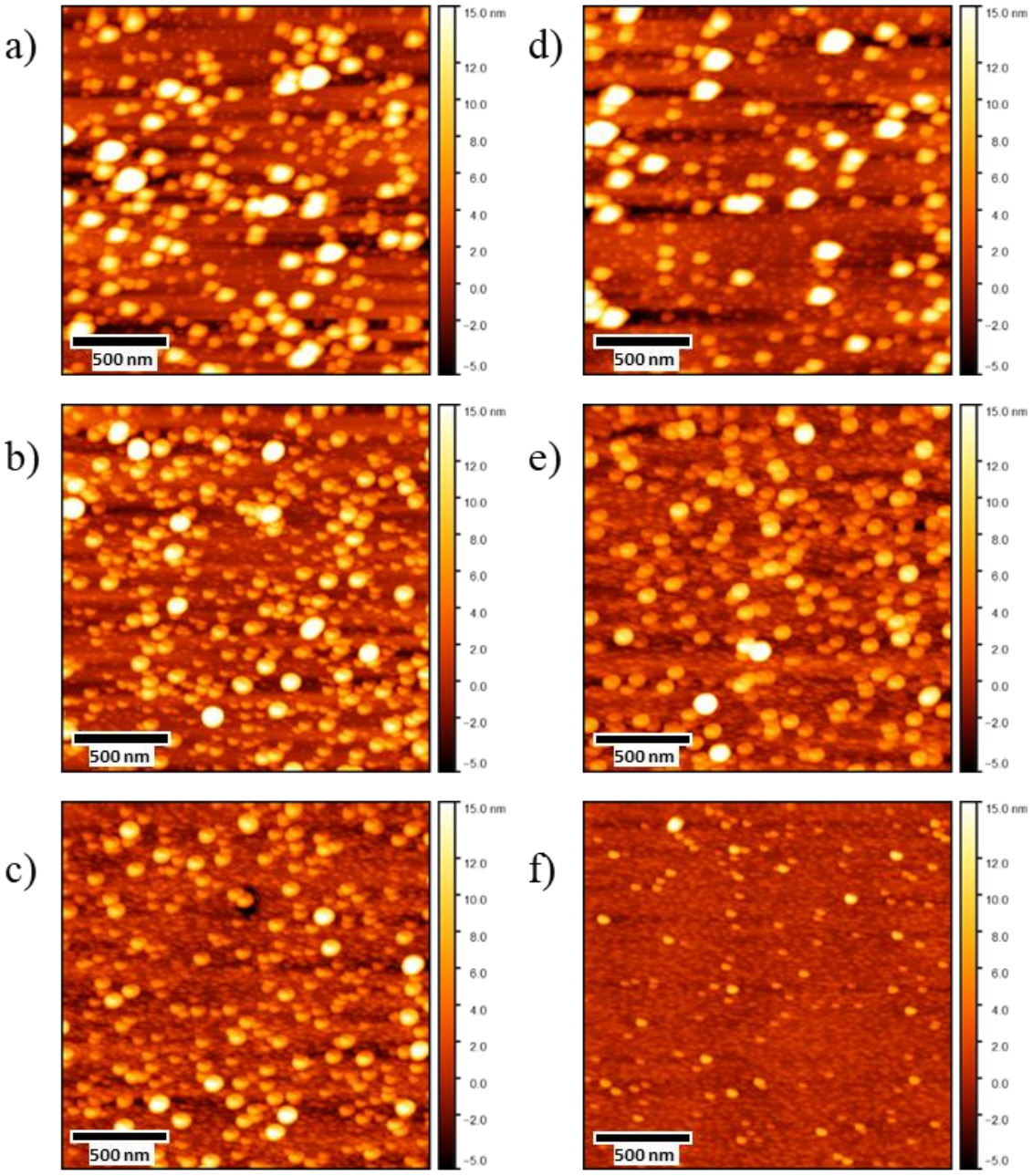

Figure 5.12 $2 \times 2\ \mu m$ AFM pictures of the InP QDs with growth rate of 0.15 ML/s and V/III ratio of a) 45, b) 20, c)10 and 0.1 ML/s growth rate for V/III of d) 45, e) 20 and f) 10.

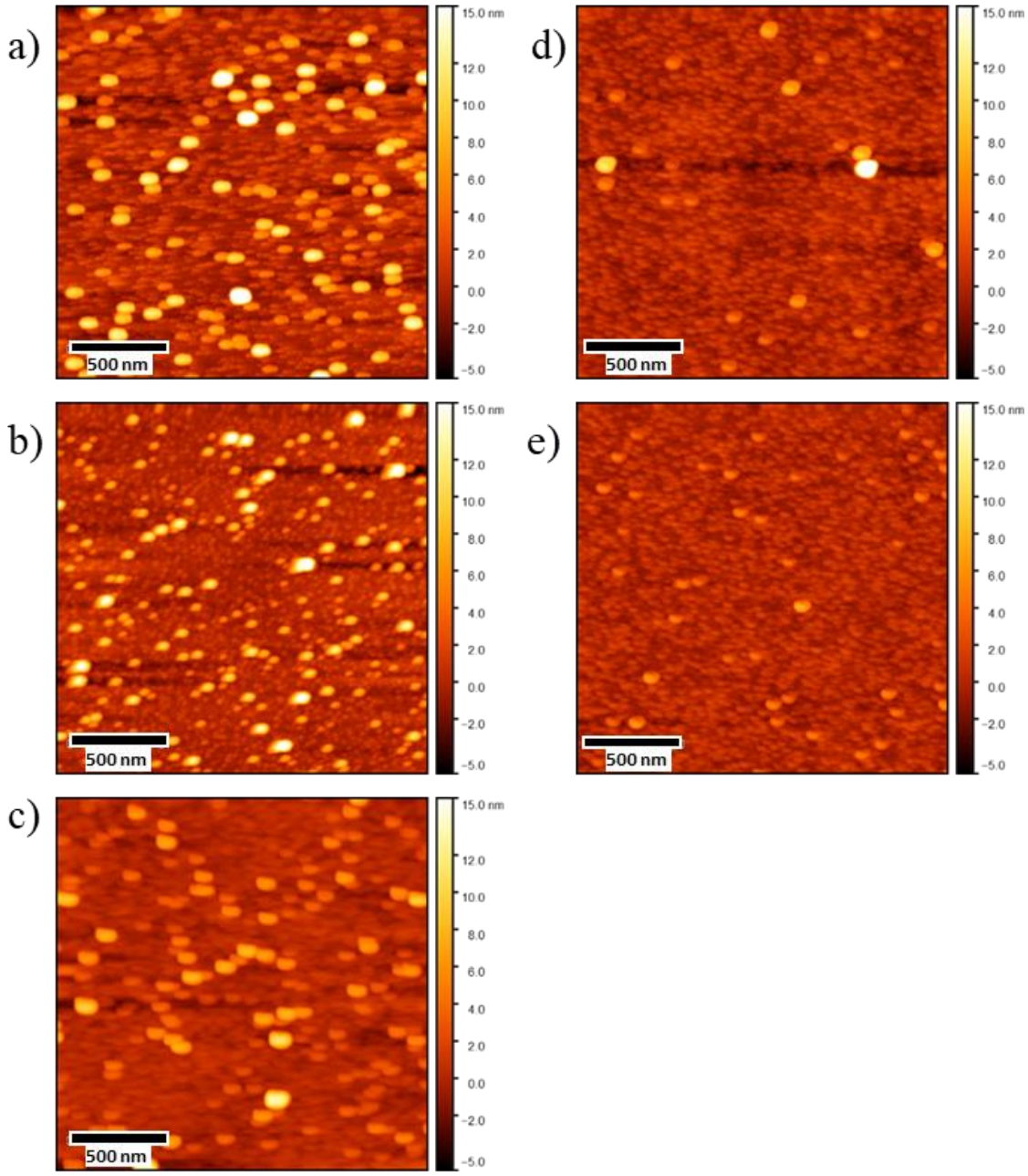

Figure 5.13 $2 \times 2\ \mu m$ AFM pictures of the InP QDs with growth rate of 0.05 ML/s and V/III ratio of a) 45, b) 30, c)20, d) 15 and e) 10.

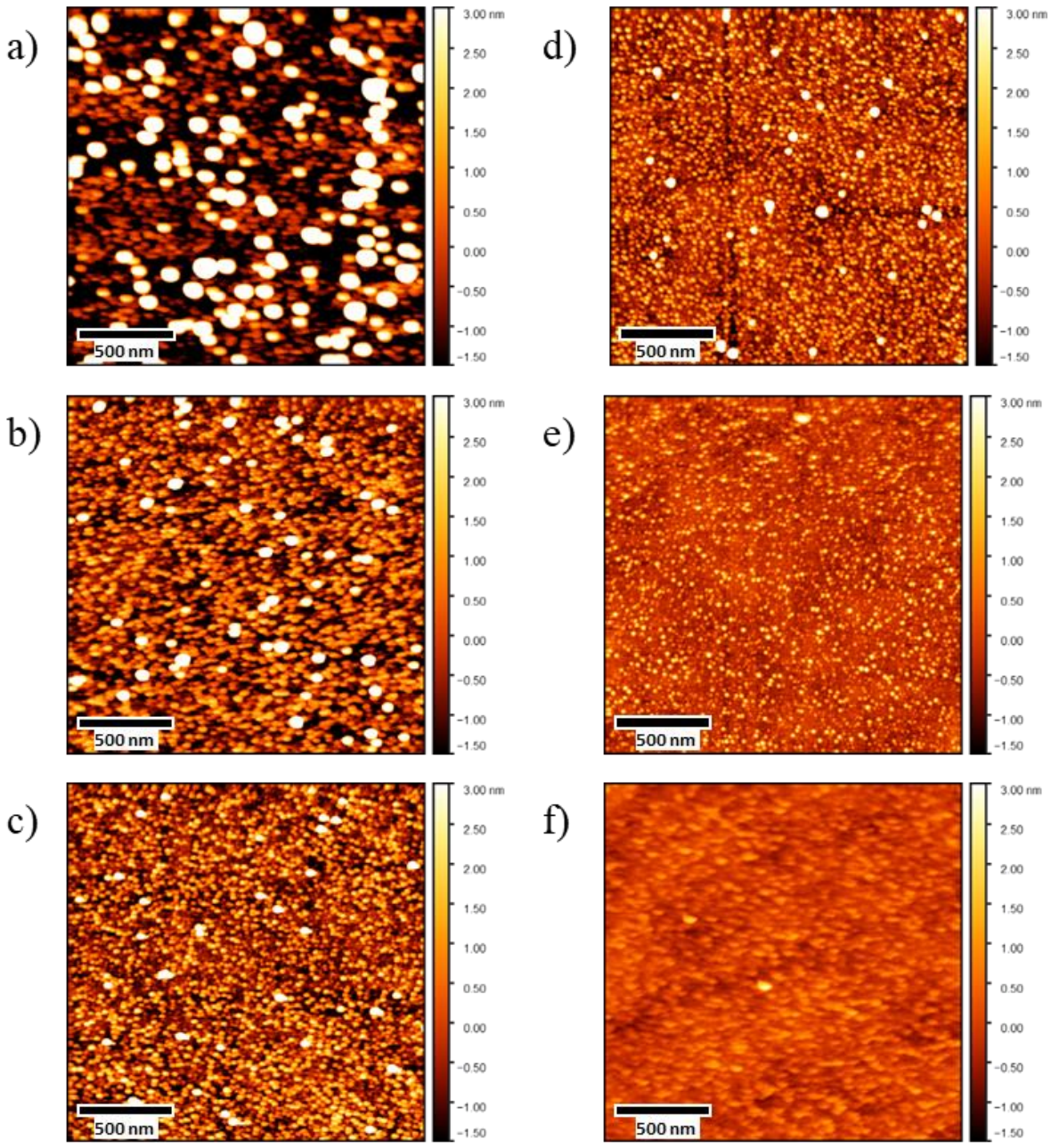

Figure 5.14 $2 \times 2\ \mu m$ AFM pictures of the InP QDs with growth rate of 0.025 ML/s and V/III ratio of a) 45, b) 30, c)25, d) 20, e)15 and f) 10.

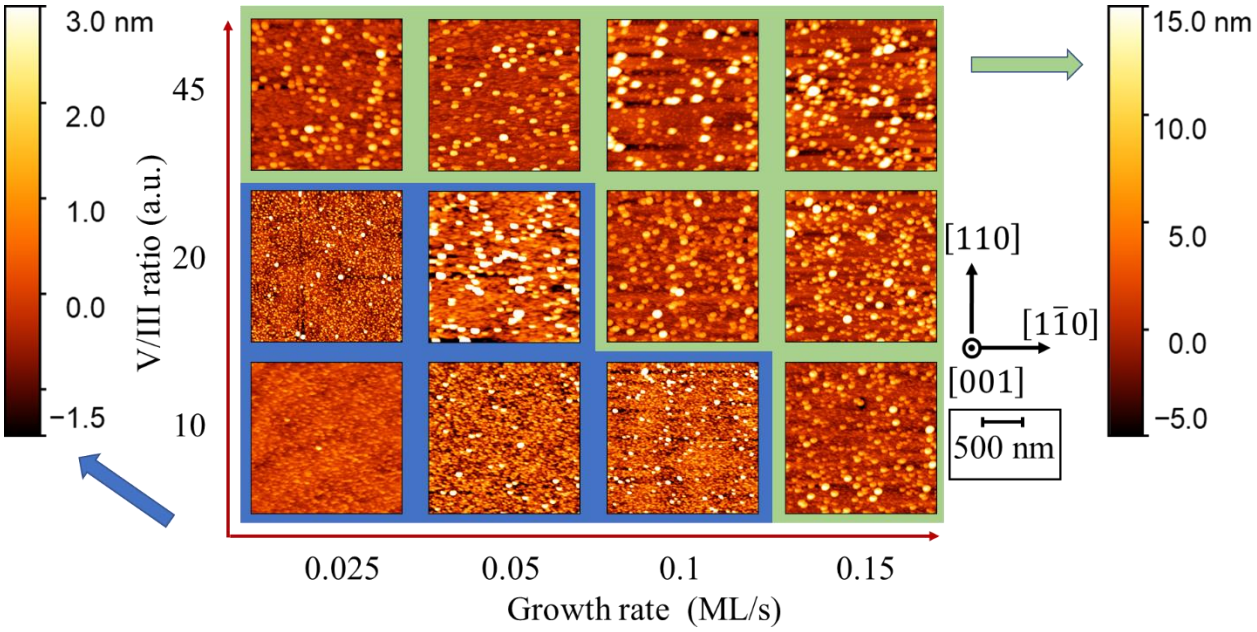

Figure 5.15 AFM images (2 μm × 2 μm) of 1.8 ML InP deposited on GaP for different growth rates and V/III ratios. The x- and y-axes represent the growth rate and V/III ratio, respectively. The z-range varies from -5 nm to 15 nm, except for the images indicated by the blue rectangle, in which the range varies from -1.5 to 3 nm as indicated by the right and left color scale, respectively.

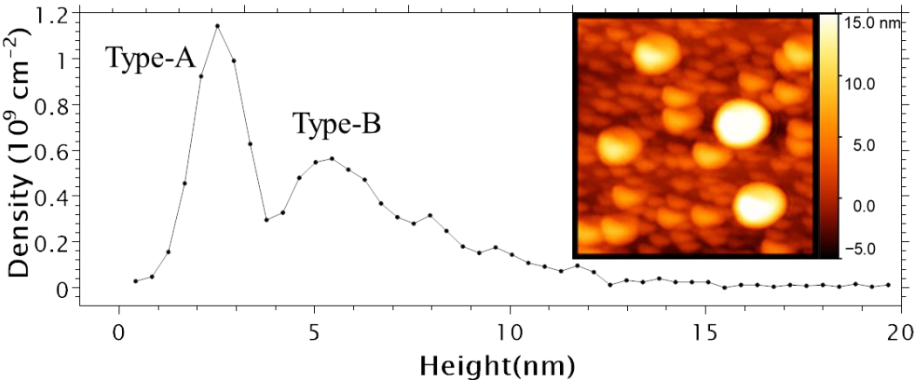

Figure 5.16 Mean height distribution of the sample grown at V/III ratio of 10 and growth rate 0.15 ML/s, with two main peaks around 2.5 nm and 5.3 nm. The inset shows a (0.5 μm × 0.5 μm) AFM image of the sample whose z-range is from -4 nm to 12 nm.

To understand the growth process of these two types of InP QDs, the V/III ratio dependence of the height distribution under the fixed growth rate was investigated. As shown in Fig. 5, type-A QDs indicate a narrow distribution, while type-B is broader than type-A QDs. For the samples grown at the growth rate lower than 0.1 ML/s, the type-B QDs could not be seen clearly due to high density of type-A QDs. From the experiments with finer V/III ratio step, the height of type-A QDs did not change monotonically, i.e., it was slightly lower than that of the typical value at V/III = 10 (labeled as A' in Figure 5.17), and then seemed to transfer to the higher one around V/III = 15. At V/III > 15, this behavior characterized by the reduction

of the distribution peak seems to occur in most of the samples. After the mode transfer from A' to A, the peak height of type-A QDs was slightly increased by the increase in the V/III ratio. Similarly, the density and size of type-B QDs increased with the V/III ratio.

As the growth rate increased, the size distribution became broader, and the density decreased with increasing growth rate. The decrease in QD density was caused by the formation of lattice relaxed big islands.

The formation of nonuniform QDs has always been a problem in the Stranski-Krastanov growth mode, and many studies have addressed the formation of QDs, especially in the InAs/GaAs system[65], [98], [99].

From the viewpoint of uniformity, no type-B QDs were present, since the type-B QDs barely started to nucleate at V/III < 15 under the lowest growth rate used in the present work (0.025 ML/s). But transition from type-A' to A occur around V/III= 15, and the peak height of type-A' is too low for achieve a vertical ordering, and thus, it was decided to use a growth rate of 0.025 ML/s and a V/III ratio of 20 for fabrication of vertically ordered QD arrays.

Generally, the reduction of quantum dot size leads larger quantum shifts while connected QDs show lowering the quantum states. Thus, the type-II band alignment is realized on the InP stacked arrays embedded in GaAsPN on Si, even though the obtained QD size seems to be slightly lower that the described in Section 2.6.4, with smaller QD size of 3nm height around 1.6 eV is still achievable.

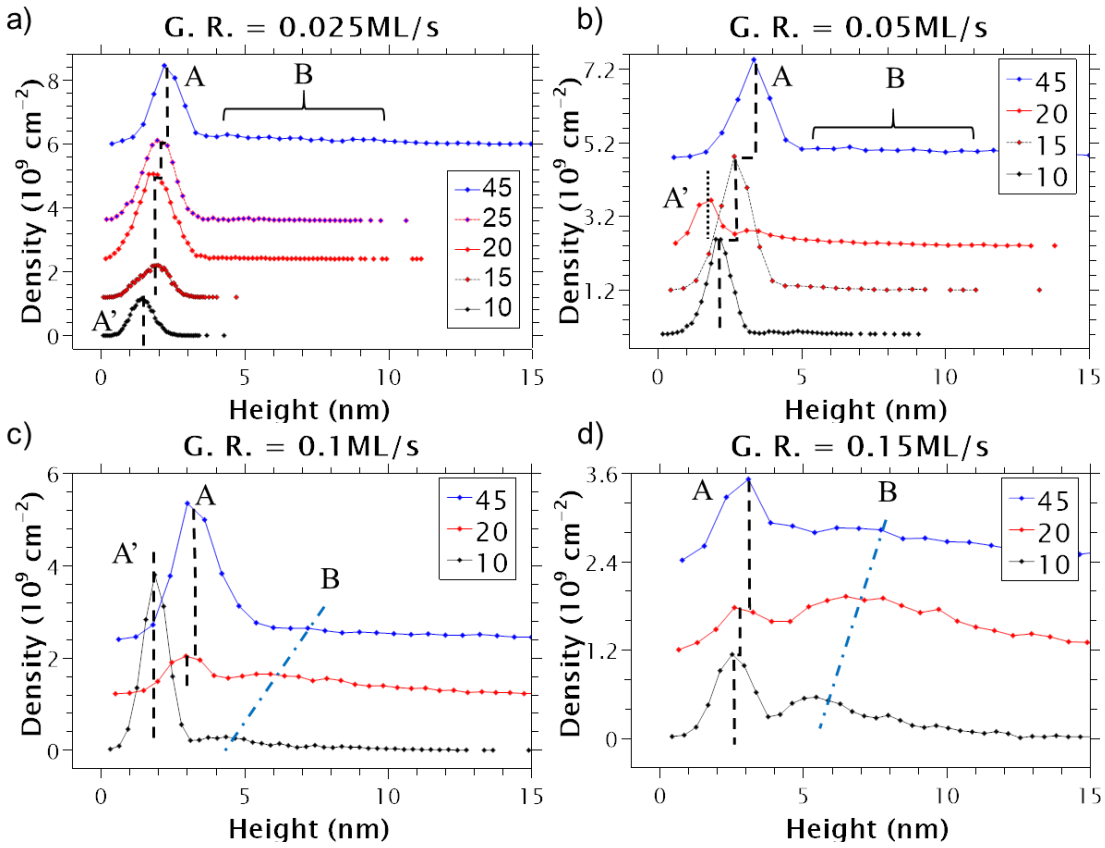

Figure 5.17 Size distribution graphs of various V/III ratios employed in this study for the grow rates of (a) 0.025 ML/s, (b) 0.05 ML/s, (c) 0.1 ML/s, and (d) 0.15 ML/s. Dashed lines show the different types of QDs.

An estimated volume from the InP QDs was obtained from some of the AFM measurements as shown in the Figure 5.18. For the different conditions it is concluded that smaller incorporation of In adatoms is achieved under low grow rate and low V/III ratio, this condition corresponds to the high diffusion behavior. This suggests that some portion of the In atoms are not incorporated to the surface and a desorption process is occurring.

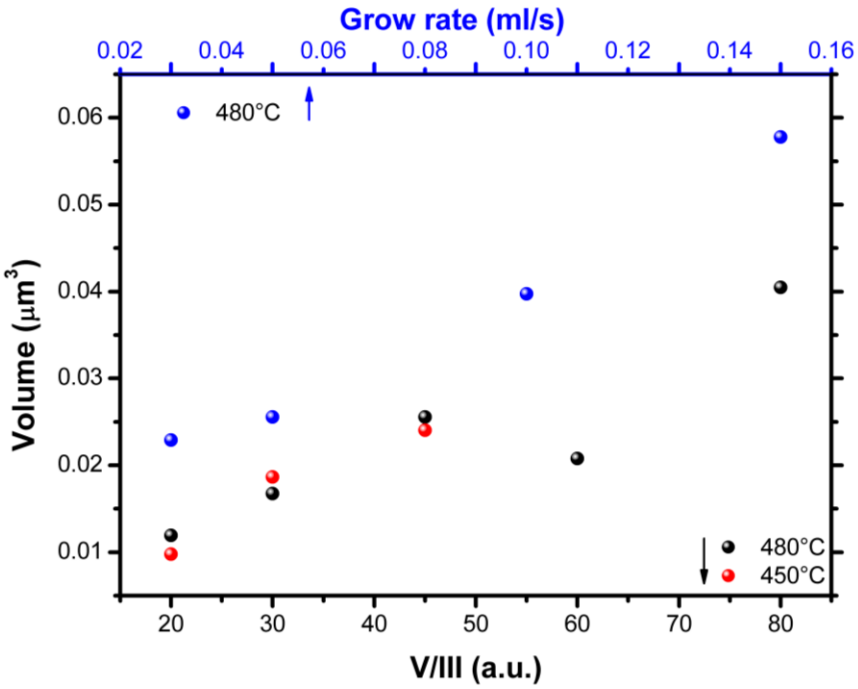

Figure 5.18 Estimated volume of the InP 1.8 ML QDs from the 2 μm × 2 μm AFM measurements for different conditions.

5.1.3 Growth interruption during InP QD growth

To improve the control in the height limit of the quantum dots, the growth interruption process was studied.

First, I evaluate the influence of the growth interruption. The growth interruption consists in interrupting the growth for a determinate period after the QD`s have been formed and the diffusion of the adatoms will change the distribution and geometry of the QD`s. For this experiment I grew an InP QD`s layer and kept the sample at the same temperature inside the chamber after the growth was finished for different intervals of time and then retrieve the sample from the MBE as usual, the time required to remove a sample from the chamber is around 6 min. The growth conditions employed are a growth rate of 0.05 ml/s for the 1.8 ML of InP growth at 480 °C with a V/III = 45 with 1.19×10^{-5} Pa for the Indium flux. The GaP layer was grown with a $V/III = 15$ and a Ga flux of 4×10^{-5} Pa with a growth temperature of 670 °C and a 0.3 μm/hr. growth rate. 30 s. 1 min. and 7 min. for interruption time were employed.

The AFM pictures presented in the Figure 5.19 showed how the growth interruption completely changed the distribution and size of the QDs. It evolves from having both type-A and type-B QDs to eliminate all the type-A QDs and only remain the type-B QDs with low density. The height distribution is shown in the

Figure 5.20. All the samples followed a bimodal distribution, as the growth interruption increased the height increased as well going from an initial 5.0 nm and 8.8 nm to 6.4 nm and 12.5 nm. Since a lower height is desire, the QDs conditions achieved at 30 s. is the desirable conditions. The mean radius at these conditions remains smaller than 50 nm, since it is planned to perform the stacking of the QDs by growth interruption, this 50nm radius is still suitable considering that the longest diffusion length at GaP for this temperature is still bigger than the radius which is advisable for the capping of the QDs.

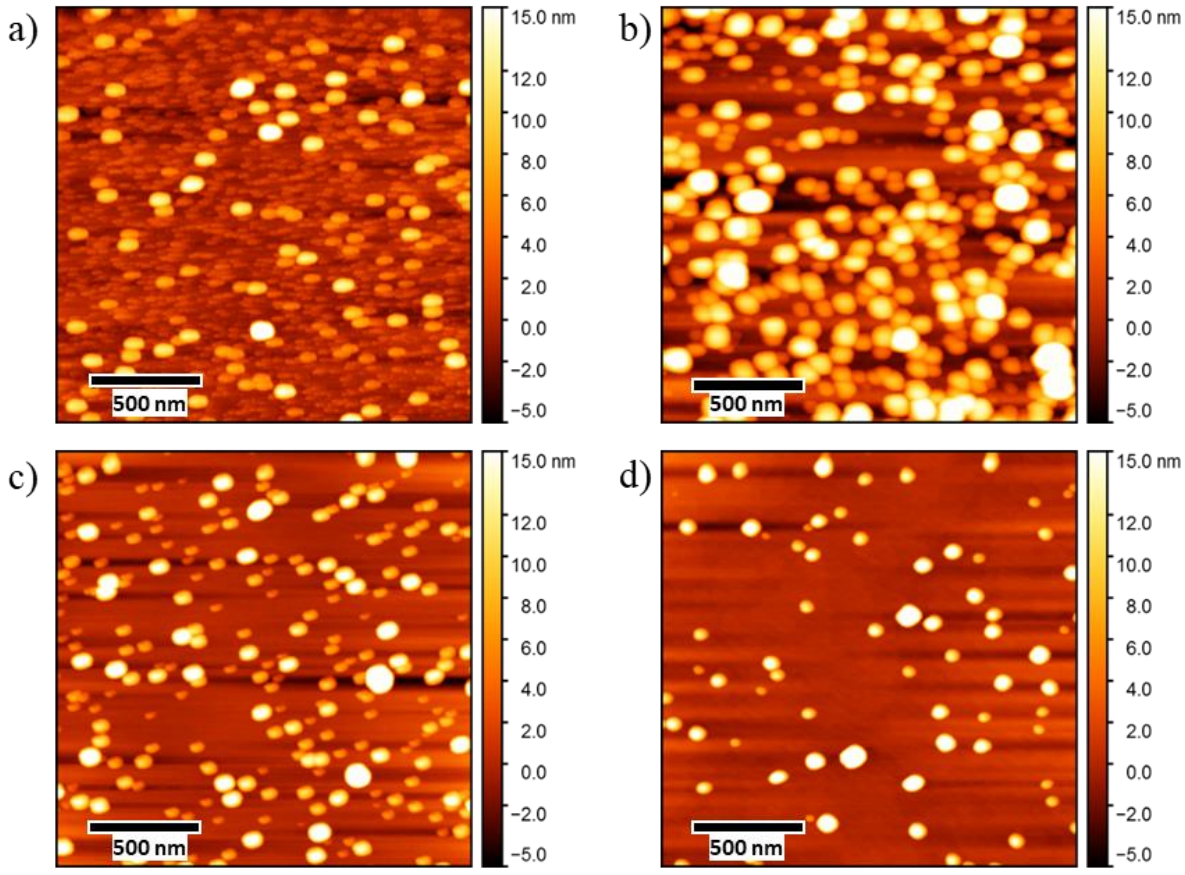

Figure 5.19 $2 \times 2\ \mu m$ AFM pictures of the growth interruption experiment for a) no growth interruption, b) 30s., c) 1min. and d) 7min. of growth interruption, respectively.

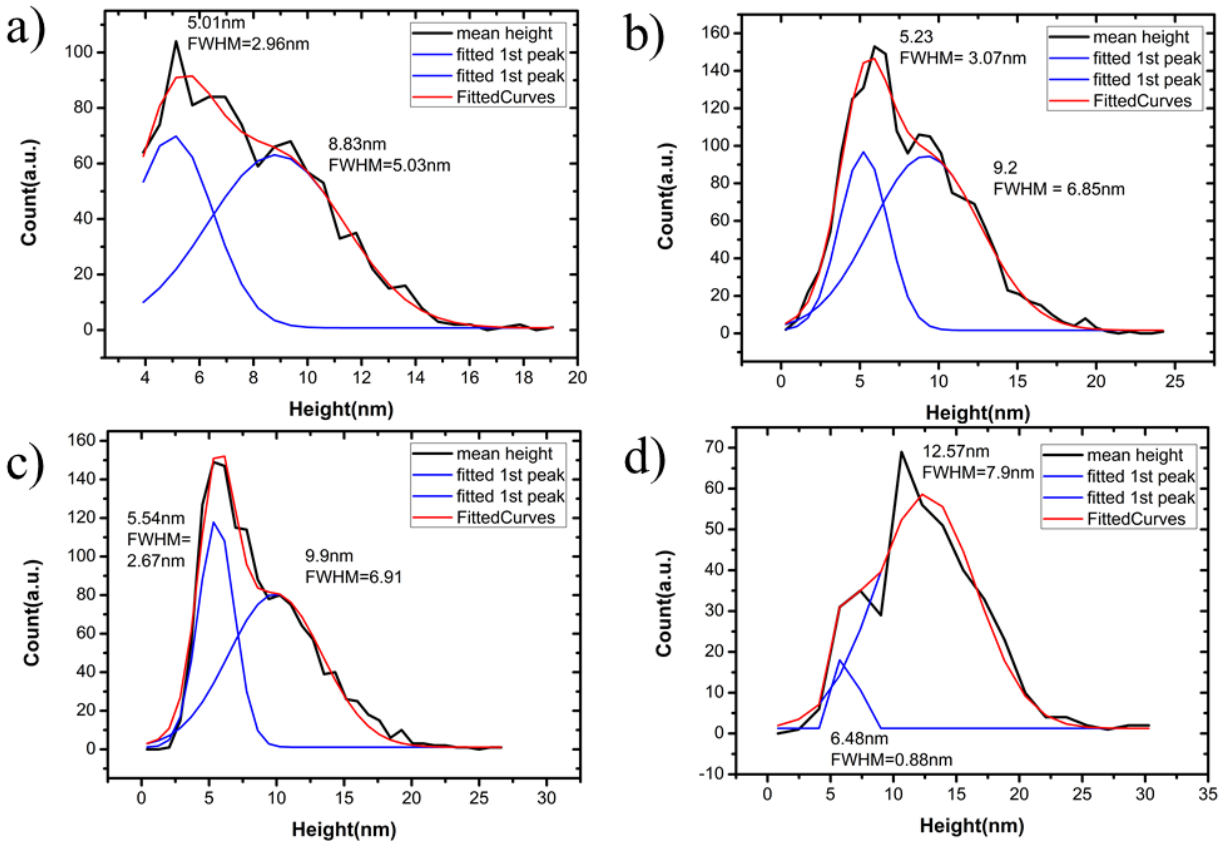

Figure 5.20 Height distribution for the growth interruption samples for a) no growth interruption, b) 30s., c) 1min. and d) 7min. of growth interruption, respectively.

It is necessary to remind the required time for sample removal from the chamber, reducing the temperature from 480 ºC to 400 ºC (in which most of the coarsening would occur) takes around 90 s. at the highest rate possible in our system. This means achieving the previous conditions requires more time than the mentioned.

5.2 Vertical alignment conditions

5.2.1 GaP capping growth conditions.

A very important step in the stacking of QDs is the capping procedure. It has been shown that the capping procedure can result in the alteration of the QD geometry[84], [85]. To reduce the number of steps during the stacking of the QDs, the growth temperature of the GaP capping layer is planned to be the same as the InP QDs. Since the growth temperature of the QD was decided in the previous section, now the growth parameters for the GaP capping layer at 480 ºC are studied. For this reason, samples were prepared for the GaP homoepitaxy at 480 ºC. The GaP layers was grown above a 100 nm thickness GaP buffer layer with a $V/III = 45$ and 0.3µm/hr. growth rate at 670 ºC, a 10 min. thermal treatment was applied at 700 °C after the introduction of the sample. The samples consisted of a 100nm thick GaP layer grown at 480 ºC, for $V/III = 3$ a 447 nm/hr. growth rate was employed. For $V/III = 2$; 672 nm/hr. and 336 nm/hr. growth rate were employed with a Ga flux of 8.96×10^{-5} Pa and Ga flux of 4.48×10^{-5} Pa, respectively. Another sample

with 50nm thickness, $V/III = 10$ and 300 nm/hr. growth rate. In the Figure 5.21 it is shown the AFM pictures for the different samples and the Table 5-3 shows the respective RMS values. Higher values as the V/III ratio and the growth rate increased were obtained. For the V/III ratio of 2 there is not a significant variation of the RMS despite the twice value of the growth rate. For the growth temperature of 480 ºC, the most important parameter is the V/III ratio. From this I can adjust the growth conditions for the GaP depending on the QDs growth conditions if a low V/III ratio can be preserved. This will be very helpful at the moment of growing the stacking structure.

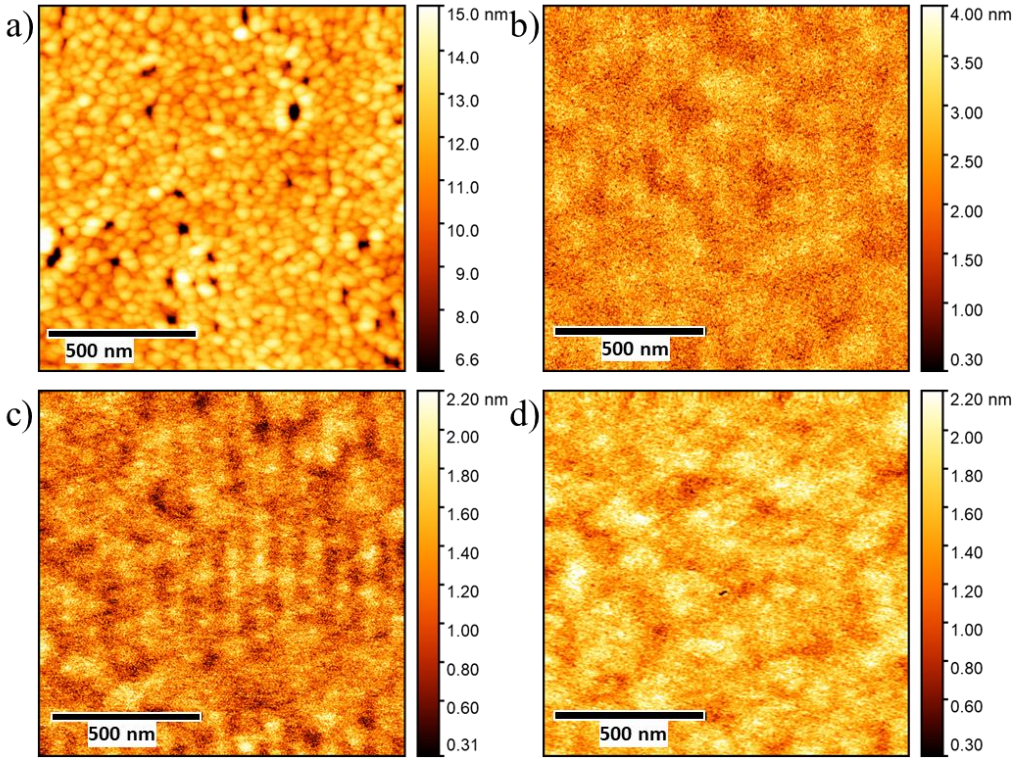

Figure 5.21 AFM pictures of GaP layers grown at 480 ºC for a) $2 \times 2\ \mu m$ with V/III ratio of 10, b) for $10 \times 10\ \mu m$ and V/III ratio of 3 ,c) and d) V/III ratio of 2 with growth rate of 672 and 447 nm/hr .

Table 5-3 RMS values for the different growth conditions of the GaP layer grown at 480 ºC.

Growth rate (nm/hr.)	$V/III = 10$	$V/III = 3$	$V/III = 2$
672	-	-	0.32nm
447	-	0.49nm	-
336	-	-	0.25nm
300	0.9nm	-	-

I also investigated the effect of the growth interruption duration for a partial capped QD. An InP quantum dot layer is grown and after that is cap by a 5 nm Ga layer, next I vary the time of the growth interruption and then retire the sample from the equipment, the surface was observed by AFM. A growth rate of 0.05 ML/s is employed for the 1.8 ML InP layer grown at 480 °C with a V/III ratio of 45, the 5nm capping layer is grown at 480 °C and a V/III ratio of 4. The duration of the growth interruption is 30 seconds, 1, 2, and 5 minutes.

In the Figure 5.22 we can observe the influence of the time during the growth interruption, in a) it is shown the InP QD layer without a capping layer for reference purpose, in b) we can observe the presence of a few InP QDs that remained after the deposition of the GaP layer, from c) to d) partially capped InP QDs does not remain in the surface, instead pits starts to appear in the surface as the 5 nm GaP layer remains at 480ºC, the density of the pits increase as time passes by. The 30s. sample [Figure 5.22c)] shows the smaller and with less density pits. It shows that despite been capped, not only the excess In atoms desorb but the In atoms from the partially capped QDs started to diffuse to the surface leaving the QD. In the Figure 5.23 a surface profile from a pit is presented showing that also the capped portion of the QD starts to diffuse outside the GaP capping layer and then desorb from the surface leaving as a pit as result. From the samples with longer growth interruption times, the number of pits drastically increased exceed the density of the type-B QDs, this suggest that not only partially capped QDs are being desorbed through this growth interruption process but also completely capped QDs. For these growth conditions, the growth interruption is acting as a In flushing at low temperature, desorbing the excess In atoms and some already capped In QDs. This indicates that at 480 ºC desorption of In is present at some rate.

Since a smooth surface is require for the stacking QDs layer, smaller QDs are required. Because despite the partially caped sample without growth interruption time shows InP QDs in the surface in fact it does includes some growth interruption time because after the deposition of the GaP layer the temperature cannot be completely reduce, this means that as I wait for the drop of the temperature unintentional annealing and quenching is still occurring. For the stacking experiments 30s. of growth interruption seems to improve the capping layer.

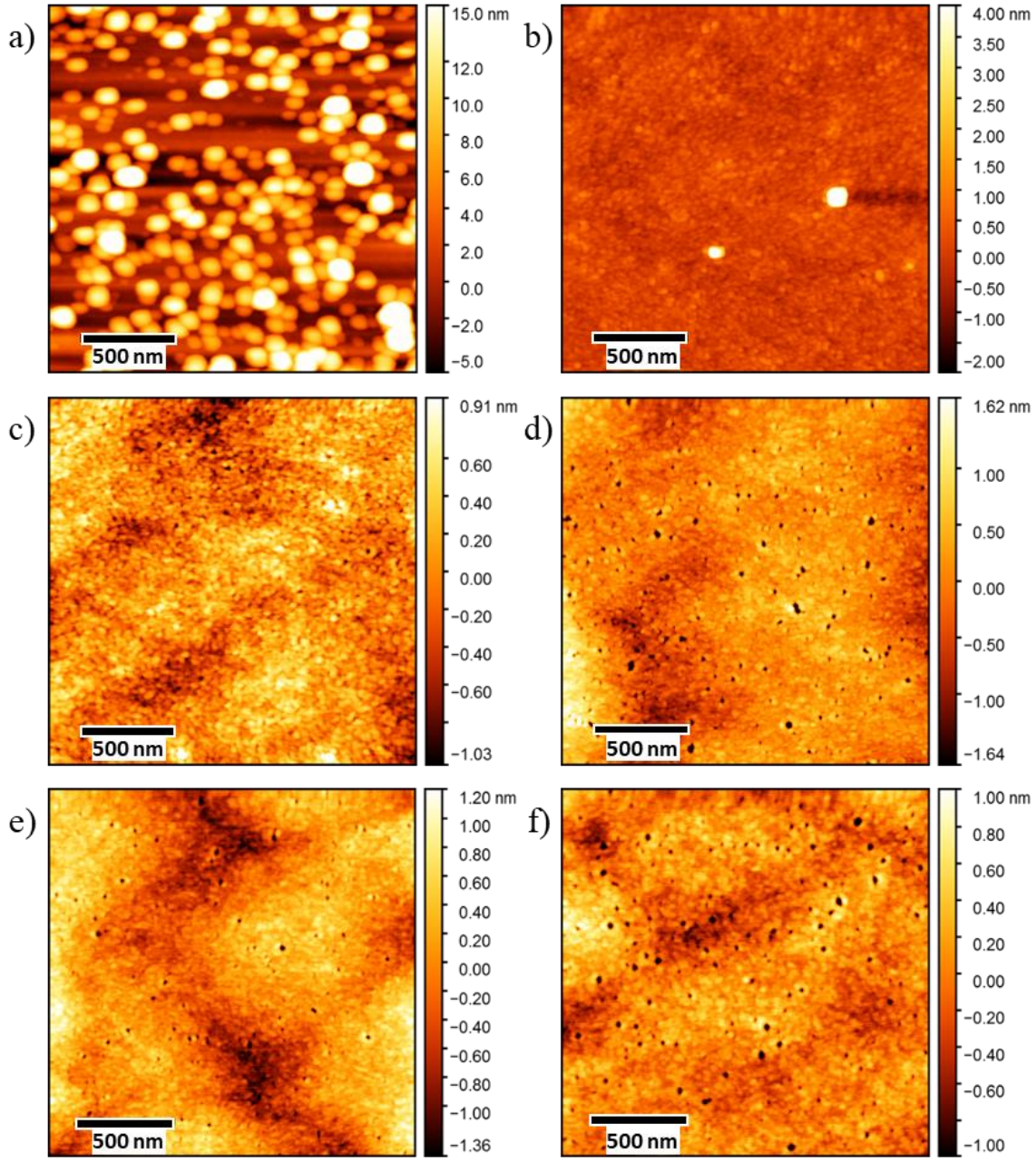

Figure 5.22 $2 \times 2\ \mu m$ AFM pictures of the a) InP QD`s, 5nm GaP caping layer b) with no growth interruption, c) 30s., d) 1min., e) 2min. and f) 5min.of growth interruption.

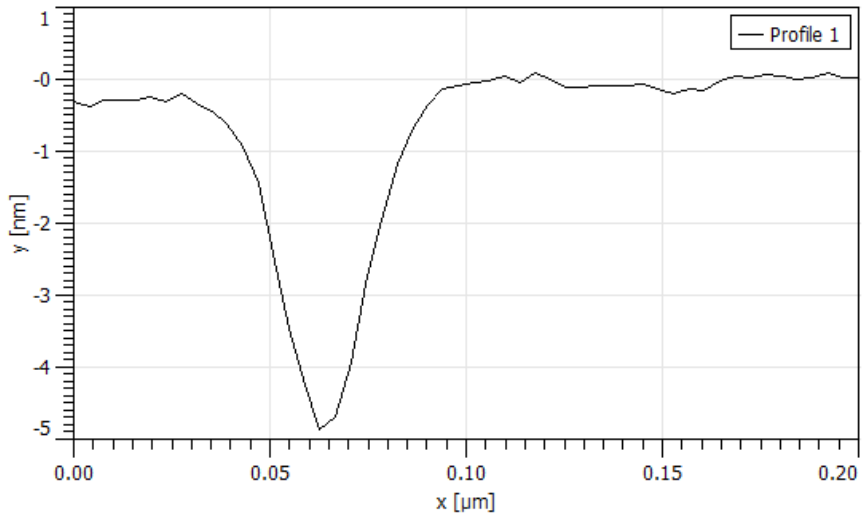

Figure 5.23 Surface profile obtained from a larger pit of the sample with 5 min. growth interruption. The depth of 5 nm is the same as the capping layer thickness.

5.2.2 InP QDs stacking conditions.

The multiple stacking of QDs layers is a promising technique to increase uniformity of size and shape as a result from the interacting strain fields that give rise to preferential direction of atom migration[100]. The layer thickness that separates the QD layers plays a determinant roll in this mechanism, the next section is focused in finding the suitable conditions to realized successfully coherent vertical alignment of QDs.

To perform the stacking of quantum dots, a sample with multiple layers of quantum dots embedded in the GaP matrix was prepared on a GaP (001) substrate, the purpose is to observe the effect of the embedding layer on the quantum dots and find the conditions for which the vertically stack is achieved. The firsts samples consist of 150 nm and 100 nm separated periods of QDs, respectively, this separation layer was grown at 480 ºC after the QD growth but after 25 and 50 nm it was grown at 670 ºC for the 150 nm and 100 nm separation layer, respectively. Each period consists of 2 QD InP layers with a capping layer, the values for the capping layer of the first sample are 120 nm, 100 nm, 80 nm, 60 nm, 40 nm, and 20 nm. From the first sample results, the capping layer thickness was decreased for the second sample to 50 nm, 40 nm, 30 nm, 20 nm, and 10nm. The growth conditions for the InP layer are 480 °C of growth temperature, V/III ratio of 45, In flux of 1.19×10^{-5} Pa, growth rate of 0.05 ML/s and 1.8 ML thickness. A growth interruption for the GaP spacer layers a V/III ratio of 10, 480 °C growth temperature and 0.3 µm/hr. growth rate.

In the Figure 5.24 the cross-sectional TEM images are shown, it is shown a vast range of QD size. The appearance of dislocations is observed in both samples, the dislocations are originated on the type-B QDs with height over 10 nm. Bigger dots were able to reach 20 nm height for 120, 100, 80 and 60 nm of capping layer thickness no stacking was observed. The stacking of QDs was started from 50 nm to lower capping layer thickness. Since the capping thickness that produce stacking is dependent of the QD size due to the different QD size, the stacking was produced in all the spacing layers below 50 nm thick. This suggest that the stacking occurred for the spacing layer from 1.5-2.5 times the size of the QDs. The height of the QDs ranged from 2-20 nm for this growth conditions.

For these samples, the optimized growth conditions of the QDs were not employed, because the larger size of type-b QDs observation is easier.

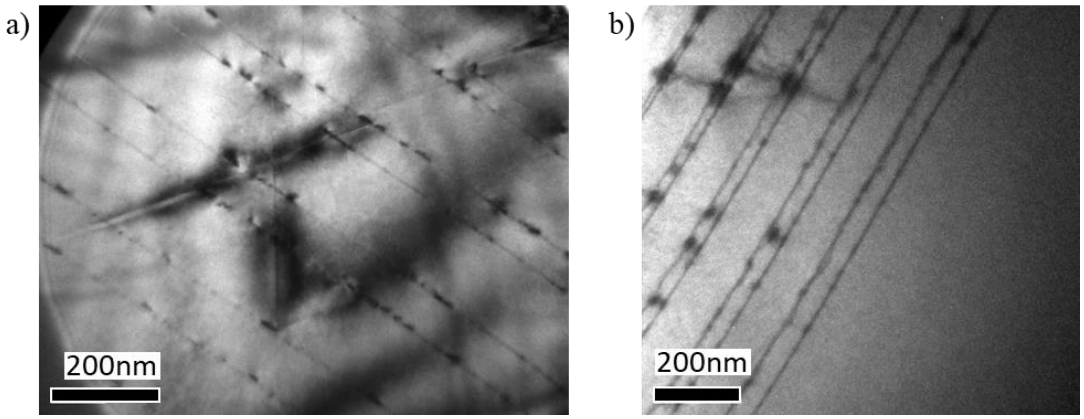

Figure 5.24 Cross-sectional TEM images of various capping layer thickness a) 20–120 nm and b)10–50 nm.

5.2.3 InP QDs growth interruption

The growth interruption of the QD was studied. A sample consist of 100 nm separated periods of QDs, the separation layer was grown at 670 ºC. Each period consists of 3 QD InP layers, the values for the capping layer are 30 nm, 20 nm, and 10 nm. The growth conditions for the InP layer are 480 °C of growth temperature, V/III ratio of 45, In flux of 5.33×10^{-6} Pa, growth rate of 0.022 ML/s and 1.8 ML thickness. For the GaP capping layers a V/III ratio of 4, 480 °C growth temperature and 0.336µm/hr. growth rate. A 30s. growth interruption was performed after the nucleation of the QDs before the capping layer growth.

As shown before the growth interruption at the end of the formation of the QDs altered the morphology. In the Figure 5.25 a) spherical shaped QDs are presented, the growth interruption seems to modify the size and shaped of the QDs, also the alteration of the GaP capping layer was observed. At the top of the type-B QDs the GaP did not grow smoothly due to the strain produced by the QDs. This effect was observed in the previous samples but with the InP growth interruption it became more frequent. The expected increased size of the QDs was the cause for the geometry change. The appearance of defects originated from the QDs is still a characteristic of the QDs.

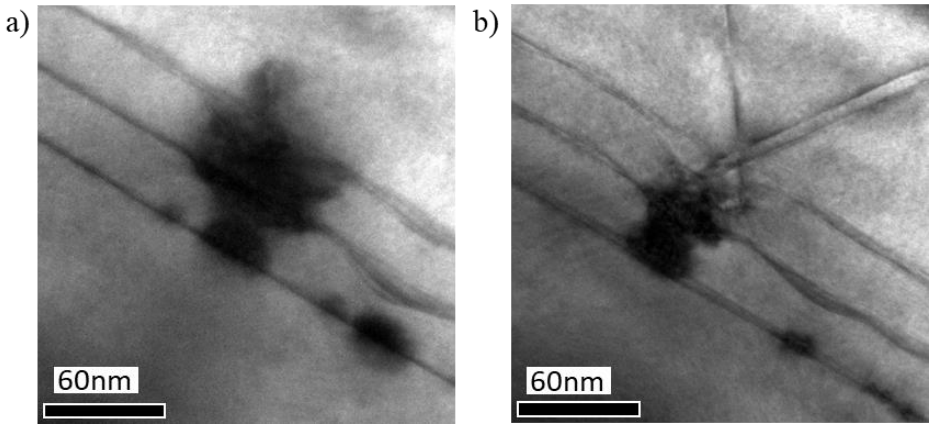

Figure 5.25 Cross-sectional TEM images for a spacing thickness of 30 nm. a) Spherical shaped QDs are observed, b) formation of dislocation was originated from bigger QDs.

5.2.4 Capping layer growth interruption

To increase the quality of the GaP capping layer and uniformity of the QDs, a growth interruption process was studied. A 60s. growth interruption was performed after the first 5 nm of the capping layer. The sample consist of 100 nm separated periods of QDs, the separation layer was grown at 670 ºC. Each period consists of 3 QD InP layers, the values for the capping layer are 30 nm, 20 nm, and 10 nm, under these conditions some uncapped QDs experienced the growth interruption process. The growth conditions for the InP layer are 480 °C of growth temperature, V/III ratio of 45, In flux of 1.19×10^{-5} Pa, growth rate of 0.05 ML/s and 1.8 ML thickness. For the GaP capping layers a V/III ratio of 4 at 480 °C and V/III ratio of 10 at 600 °C with 0.336µm/hr. growth rate. A reference sample was also prepared, the growth conditions are the same except the capping layer growth interruption. A 30 s. growth interruption was performed after the nucleation of the QDs. The duration of the temperature rising was around 1 min.

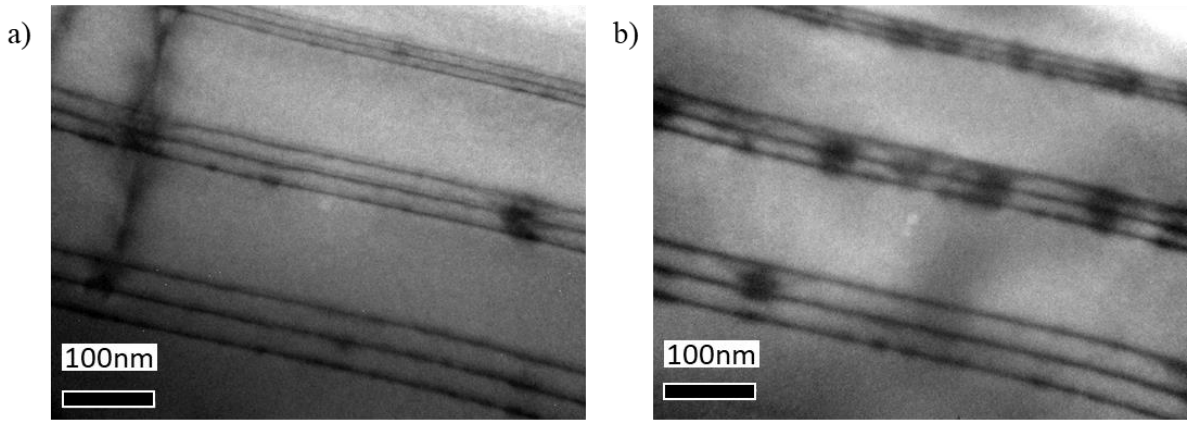

Figure 5.26 Cross-sectional TEM images for a spacing thickness of 30 nm, 20 nm, and 10 nm. a) Sample with capping layer growth interruption and b) reference sample.

In the Figure 5.26 it is shown the TEM cross-section images for the a) GaP growth interruption sample and b) the reference sample. Both samples presented defects through all the growth, and the behavior is similar. Yet a slightly lower density of defects and type-B QDs was observed with the capping layer growth interruption. This may be due to the improvement of the GaP capping layer previously to the nucleation of the QDs. In the case for growth interruption performed after a 5 nm capping thickness which is smaller than the type-B QDs, significant decrease in the density of the QDs was observed, the impact of the process relays in the growth interruption of uncapped QDs, as showed before helped in the desorption of higher QDs.

5.2.5 Indium flushing

Indium flushing technique [83] was also studied. The first sample for the In flushing technique consisted of an increase in the temperature before the capping layer was terminated and the last 5 nm were grown at 670 ºC with a GaP V/III ratio of 15. The sample consist of 100 nm separated periods of QDs, the separation layer was grown at 670 ºC. Each period consisted of 3 QD InP layers, the values for the capping layer are 50 nm, 40 nm, 30 nm, 20 nm, and 10 nm. The growth conditions for the InP layer are 480 °C of growth temperature, V/III ratio of 45, In flux of 3.28×10^{-5} Pa, growth rate of 0.133 ML/s and 1.8 ML thickness. For the GaP capping layers a V/III = 4, 480 °C growth temperature and 0.3 µm/hr. growth rate.

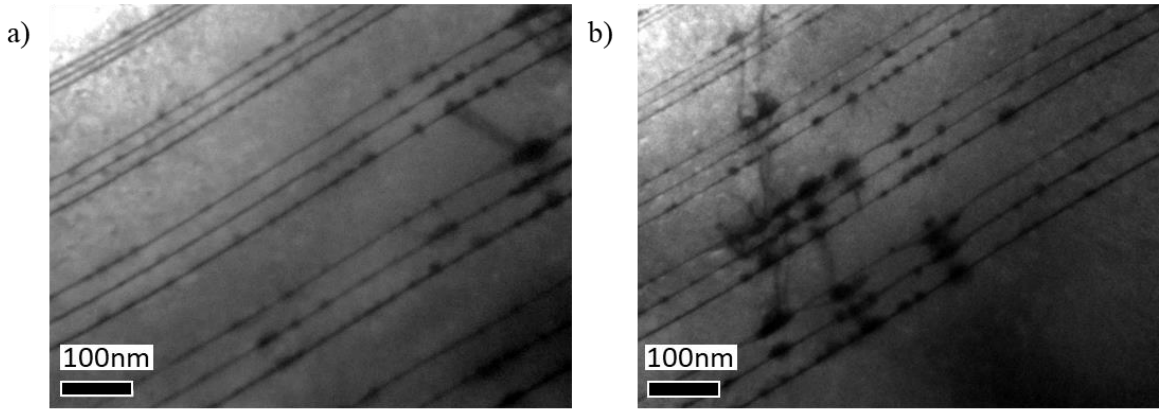

Figure 5.27 Cross-sectional TEM images for In flushing at the last 5nm of the capping layer for different capping layer thickness. a) and b) show different regions of the sample.

In the Figure 5.27 a) it was observed that the size of the type-B QDs was considerably reduced by the In flushing. This effect was stronger as the capping thickness was reduced, for the 10 nm capping layer almost no type-B QDs were observed. Despite the impact of the In flushing defects originated from type-B QDs were still observed in the sample as shown in Figure 5.27 b). The higher QD size for the thicker capping layers indicates that as the QD is completely covered and the GaP layer continues to embed the QD the effect of the In flushing decrease, for this reason with the 5 nm In flushing the type-b QD formation can be prevented.

To prevent significant intermixing of the In atoms the In flushing was studied at 600 ºC. Here I prepared a sample consisted of 2 periods with 20 nm thick capping layer. The first consisted of an In flushing after the first 15 nm of the capping layer and the last 5nm at 600 ºC, the second period applied the In flushing after the first 10 nm of the capping layer and the next 10 nm at 600 ºC. The growth conditions for the InP layer are 480 °C of growth temperature, V/III ratio of 45, In flux of 1.19×10^{-5} Pa, growth rate of 0.05 ML/s and 1.8 ML thickness. For the GaP capping layers a V/III ratio of 4 at 480 °C and V/III ratio of 10 at 600 °C with 0.3 µm/hr. growth rate. A 30 s. growth interruption was performed after the nucleation of the QDs.

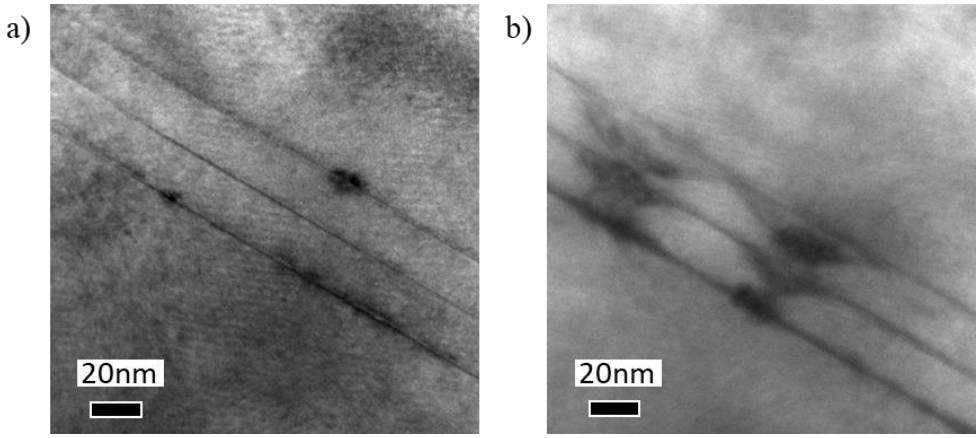

Figure 5.28 Cross-sectional TEM images for In flushing after a) 10 nm of capping layer and b) 15 nm of capping layer thickness.

From the Figure 5.28 it is shown that with the In flushing applied after 10nm of GaP capping layer the size of the QD is significantly reduced but still type-B QD appeared. With In flushing at 15nm QD size are bigger compared with the 10nm In flushing and could reach 10nm height.

The final sample for the In flushing test, consisted in rising the temperature to 600 ºC after the 5 nm of the capping layer. The first period consisted of growing 15 nm at 600 ºC after and in the second period after rising the temperature to 600 ºC, the temperature was preserved for 10s. and then decreased until 480 ºC at which the rest of the capping layer was deposited. The growth conditions for the InP layer are 480 °C of growth temperature, V/III ratio of 45, In flux of 1.19×10^{-5} Pa, growth rate of 0.05 ML/s and 1.8 ML thickness. For the GaP capping layers a V/III ratio of 4 at 480 °C and V/III ratio of 10 at 600 °C with 0.3µm/hr. growth rate. A 30s. growth interruption was performed after the nucleation of the QDs.

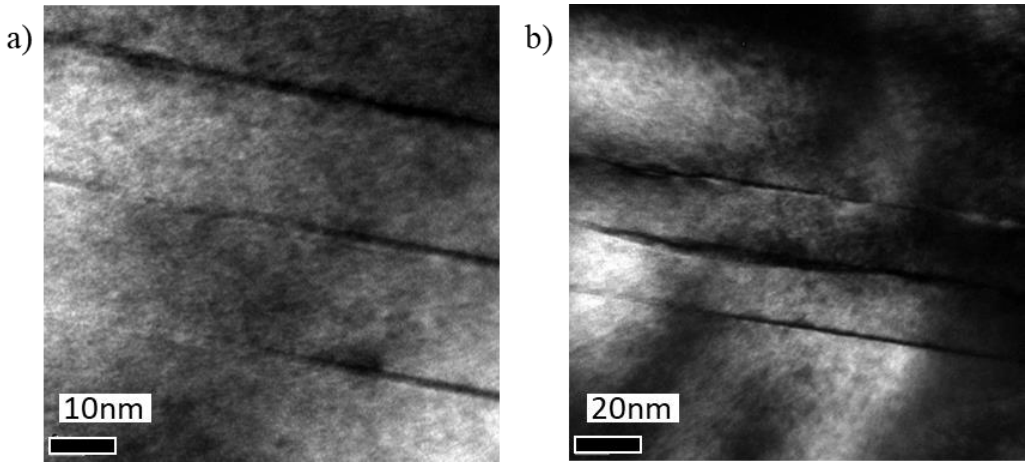

Figure 5.29 Cross-sectional TEM images for In flushing after 5 nm of capping layer grown at a) 600ºC and b) 480 ºC.

In the sample in which the capping layer was grown at 600 ºC after the In flushing I observed a very low formation of QDs, particularly type-A QDs were not observed and only a few type-B remained was shown in the Figure 5.29 a), for the situation in which the capping layer was grown at 480 ºC almost no QDs were observed at all b). For the second case the time that required to reduce the temperature to 480 ºC after the In flushing was 3min. Since the density of QDs is even lower in this case showed that influence of the time in the In flushing process, also that the In flushing can be performed at lower temperature. Despite the 5 nm capping layer no type-A QDs were observed after the In flushing process which means that completely capped QDs can also be desorbed at this temperature.

In flushing was probed to be very effective reducing the size of the type-B QDs but at the same time, completely elimination of type-A QDs was observed, for these temperatures it turned out to be very aggressive. For smaller QDs it needs to be completely optimized. Capping layer thickness, In flushing temperature and duration of In flushing are critical values for this technique. Duration is related to the temperature of the In flushing since the time required to rise and decrease the temperature. A disadvantage is the extra step of increasing the temperature. For a multilayered structure it will significantly increase the growth time.

From the previous sections very useful results which will enable the controlled stacking of QDs were obtained, first the GaP capping layer growth conditions indicated that low growth rate and low V/III ratio

achieve the flattest surface at 480 ºC, the impact of the V/III showed to be stronger than the growth rate. From this is possible to match the P flux of the GaP layer to the InP conditions to reduce any change during the growth. During the growth of an elaborated structure this can become an advantage.

From the stacking study it was observed that capping thickness is an important factor to the successfully stacking of the QDs, and this thickness depends on the QDs size. The stacking was observed within a capping thickness (h) between 1.5h and 2.5h, below 1.5h stacking is also possible but values close to 1h tends to create QD with defects and also reduce the quality of the GaP capping layer so bigger values are preferred.

The growth interruption of the QDs showed to modify the geometry of the QDs producing a spherical shape and increasing slightly the height of the QD, unfortunately bigger QDs are not the most desirable conditions due to the generation of defects. The growth interruption of the GaP capping layer was studied showing a reduction of the defects due to the QD size studied, the impact of the capping layer growth interruption would be more significative for QD height like the thickness at which the growth interruption is applied.

The In flushing was the most effective technique in reducing the size of the QD unfortunately without control it can desorb the entirety of the In atoms, a handicap is the time that it requires to increase the temperature and this time contributes to the In flushing, also this step increase the time and the complexity in a multilayer QDs stacking structure. Maintaining the simplicity in the structure growth is an advantage for any device. For these reasons in the next structure growth, was not employed.

5.2.6 Embedded QDs geometry

Due to the importance of the height of the QDs during the stacking, a sample with the optimized growth parameters was prepared for TEM cross-sectional study. The sample consisted in a 100nm GaP buffer layer grown at 670 ºC with a V/III ratio of 15, then a InP QD layer and finally a GaP capping layer was deposited. The growth conditions for the InP layer are V/III = 20, In flux of 5.97×10^{-6} Pa, growth rate of 0.025 ML/s and 1.8 ML thickness. For the 20 nm thick GaP capping layer a V/III ratio of 3 at 480 °C with 0.3µm/hr. growth rate was employed.

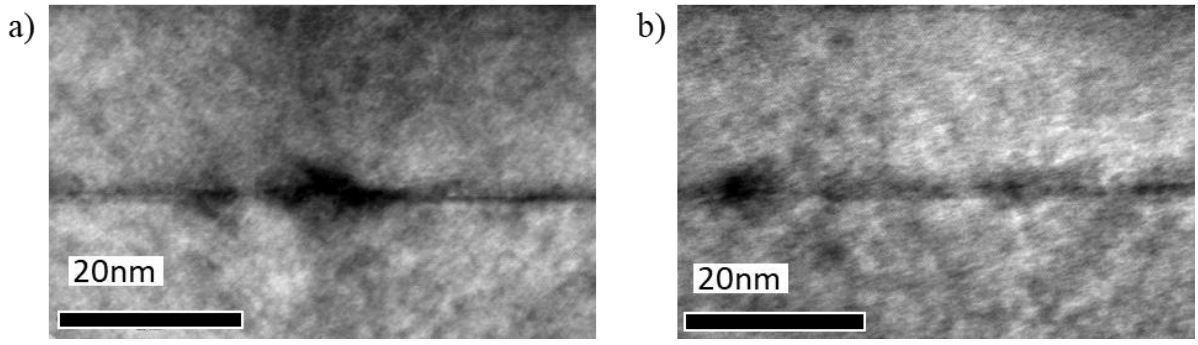

Figure 5.30 Cross-sectional TEM images of a) 4 nm and b) 2.5 nm height QD.

From the cross-section TEM images it was observed the height of the embedded QDs, the values obtained oscillated from 1.3 to 4.7 nm with diameter between 15 and 20 nm. In the Figure 5.30 examples for some of the QDs are shown. From these results it expected a stacking with capping layer thickness in the range

of 5 – 10 nm. To perform the stacking of quantum dots, a sample with multiple layers of quantum dots embedded in the GaP matrix was prepared. The sample consist of several periods of quantum dots, each period consists of 3 multi stacked QDs InP layers and, the values for the capping layers are 3 nm, 5 nm, 7 nm, and 10 nm. The growth conditions for the InP layer are 480 °C of growth temperature, V/III = ratio of 20, In flux of 5.97×10^{-6} Pa and 1.8 ML thickness. For the GaP spacer layers a V/III ratio of 2, 480 °C growth temperature and the 0.45µm/hr. for the growth rate. With a growth interruption process of 1 min after the GaP capping was employed.

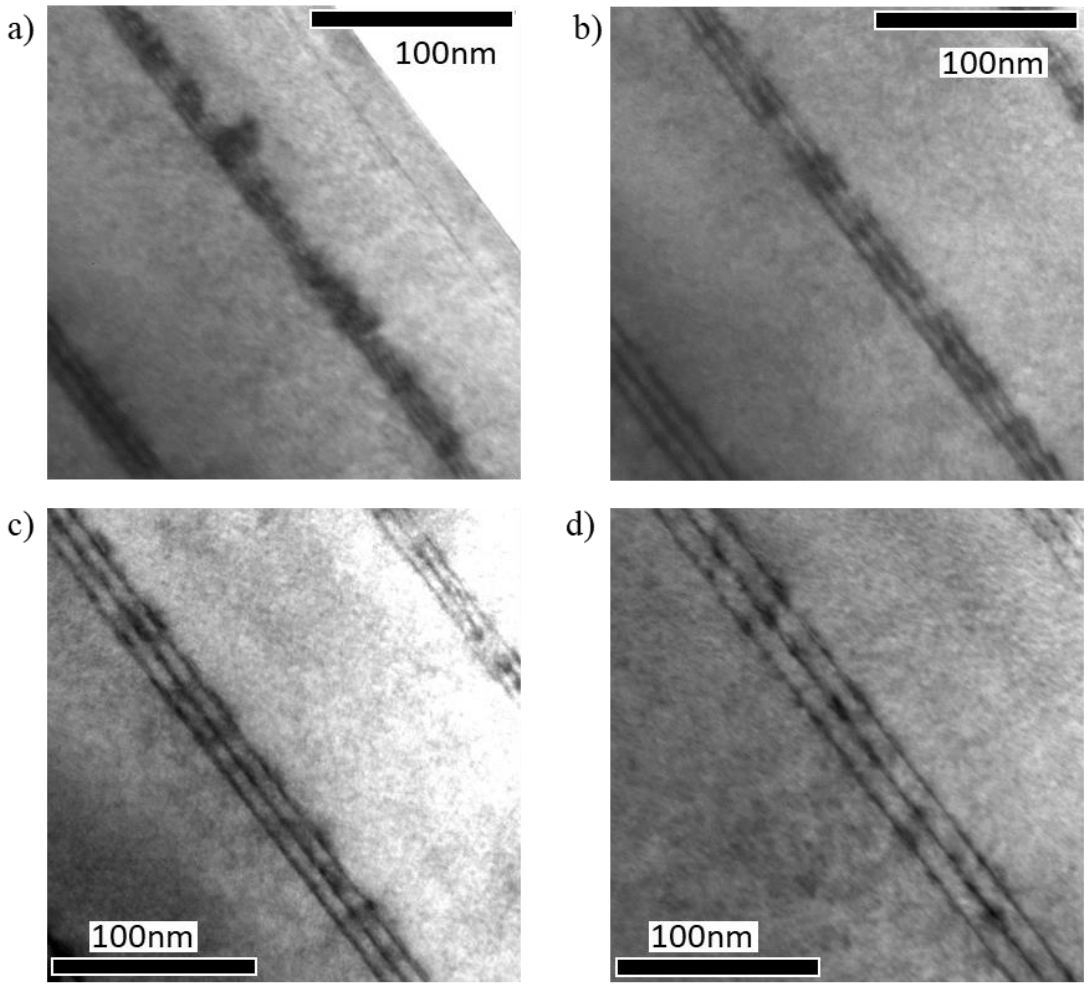

Figure 5.31 Cross-sectional TEM images of stacked QDs for a capping layer thickness of a) 3 nm, b) 5nm, c) 7 nm, and d) 10 nm.

In the Figure 5.31 TEM cross-sectional images with the different capping layers are shown. With 3 nm a) some defects are formed originated by the bigger QDs, with this thickness also a deformation of the GaP capping layer, this was observed by the waving of the InP wetting layer. With 5 nm b) the waving of the InP wetting layer was also observed but with less frequency, and no significant defects noticed. For 7 nm and 10 nm some stacking was observed but it was more frequent at 7 nm. This suggested that the stacking of coherent QDs is feasible between 7 nm and 10 nm.

5.3 Vertical alignment

5.3.1 Multiple QDs layers

To achieve the vertical alignment and observed the influence of the multiple stacking QDs, samples with multiple QD layers were prepared, the same conditions of the QD morphology study for the GaP buffer layer were employed on an epiready semi-insulator GaP (001) substrate. After decreasing the temperature to 480 °C, a 20 period InP/GaP was deposited consisting of a 1.8 ML thick InP layers with 7 nm and 10 nm thick GaP capping layers. The growth conditions for InP dots and GaP capping layers were 0.025 ML/s with V/III ratio of 20 and 0.3 µm/h with V/III ratio of 3, respectively. A growth interruption process of 1 min. was performed at the end of every capping layer to smooth the surface previous the deposit of the QDs.

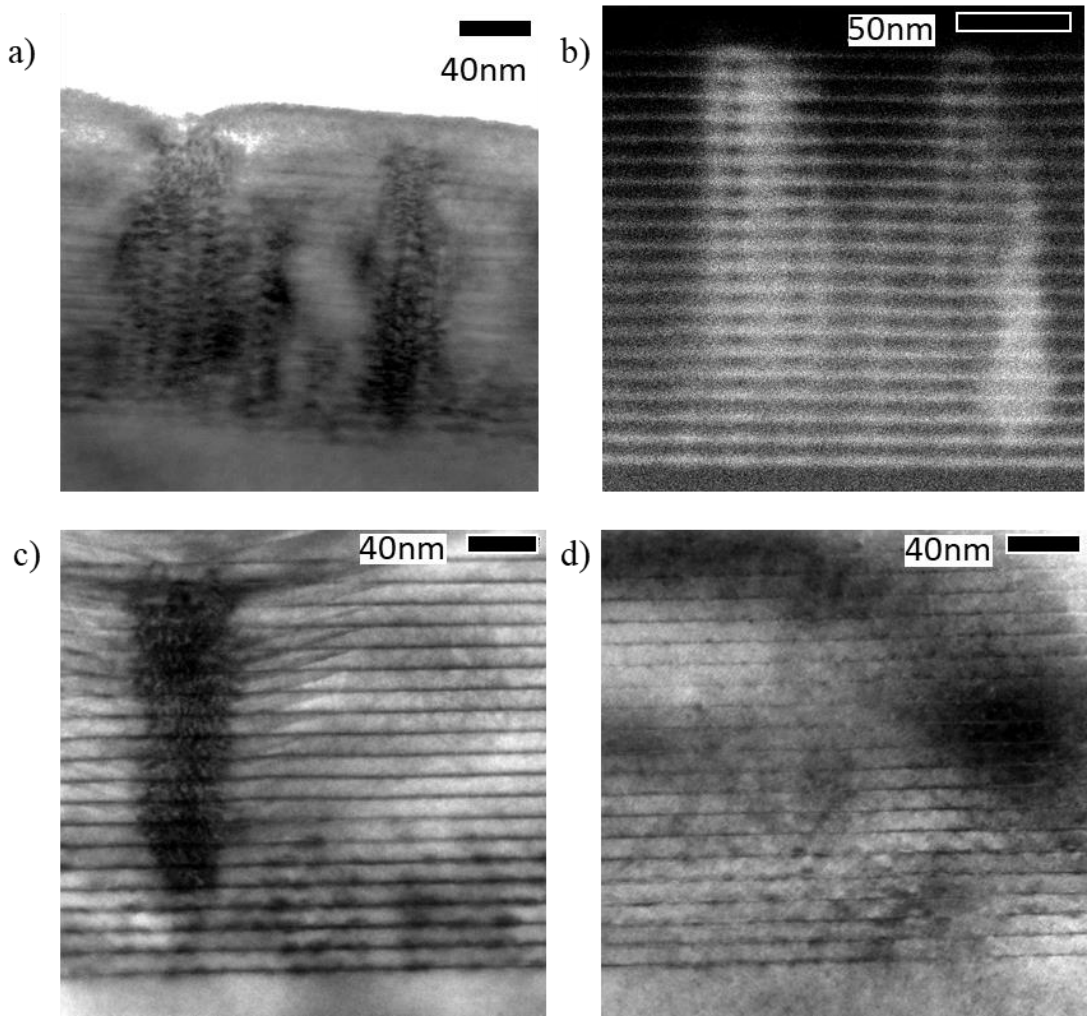

Figure 5.32 Cross-sectional TEM images of stacked QDs and defects formation for a capping layer thickness of a) 7 nm for bright field conditions, and by b) STEM bright field conditions. For 10 nm capping layer defects were observed c) originated at bigger QDs, and d) random nucleation of QDs.

From the TEM cross-section figures the presence of defects originated from stacked QDs was observed as shown in Figure 5.32 a) and c). In the sample with 7 nm successful stacking QDs was achieved along with defects generation through the QD columns. The origin of the defects occurred in the firsts InP layers of the growth, unlike the sample with 10 nm, where defects were originated after a few InP layers. Except for the defects generated almost no stacking of the QDs was observed in other sites of the sample with 10 nm capping thickness. In the Figure 5.33 it is observed a column of stacked QDs, as the number of layers increased the size of the QDs increased. This suggest that the 10 nm capping thickness does not produce a significant amount of stacked QDs and is only formed from the biggest QDs. To increase the formation of columns and decrease the defects originated an intermediate capping thickness was required.

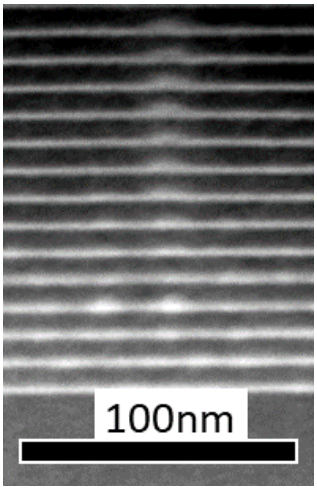

Figure 5.33 STEM cross-section image of stacked QDs with 10 nm of capping.

5.3.2 Two step-growth interruption process

To improve the overall morphology of the stacked QDs, two-step growth interruption as shown in the Figure 5.34, which compromised a QD top flattening by interruption after a partial capping of the QD and flattening of the GaP capping layer surface by another growth interruption after completing the capping, was adopted. A sample with 30 QD layers was prepared, the same conditions of the QD morphology study for the GaP buffer layer were employed on an epiready semi-insulator GaP (001) substrate. After decreasing the temperature to 480 °C, a 30 period InP/GaP was deposited consisting of a 1.8 ML thick InP layers with 8.5 nm thick GaP capping layers. the growth conditions for InP dots and GaP capping layers were 0.025 ML/s with V/III ratio of 20 and 0.3 µm/h with V/III ratio of 3, respectively. For the capping layer, the initial 5nm were followed by a growth interruption of 1 min. continued by the final 2.5 nm with a subsequent growth interruption of 1 min. During the growth of the stacked QDs and capping layers the growth temperature and the P flux was kept constant. A sample with the same conditions except for the first growth interruption after the initial 5 nm of the capping layers was prepared to compare the effectiveness, this procedure will be referred as standard growth.

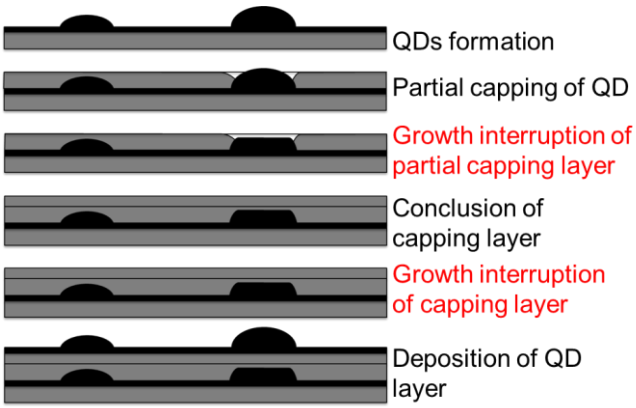

Figure 5.34 Sketch of the two step-growth process indicating the growth interruption steps.

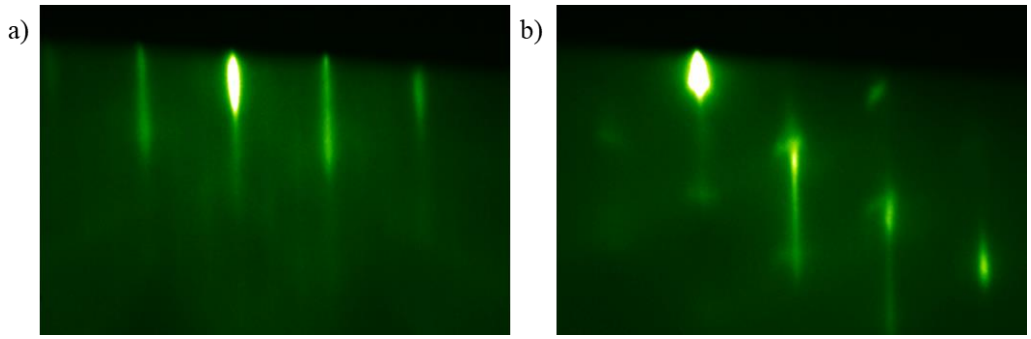

Figure 5.35 RHEED pattern images at the <110> direction of the a) GaP surface before the growth of the InP and b) after the formation of InP QDs.

Transition time of RHEED pattern from streaky to spotty was monitored to see the effects of the two-step interruption, at Figure 5.35 the RHEED patterns associated to this transition are presented. Figure 5.37 shows the change of the transition time of InP QD as increasing the stacked layer number. In case of the growth without the interruption process, transition time, i.e., InP QD formation time, was scattered and the streak pattern was broad and short after a few cycles because of GaP capping surface roughening as shown in the Figure 5.36. While RHEED pattern before the InP deposition was streaky, with the two-step interruption the transition time shows an initial reduction to a gradually constant value as the cycles increased, although, the P flux was kept constant for all the layers. This reduction could be associated with the increase of In adatoms due to the surface segregation, but the slightly large InP dots could be reevaporated during the first interruption preventing exceeding accumulation of In adatoms and for the later stacked layers would limit the maximum height of the QDs. From a single capped QD layer sample with growth interruption of the partial capped QD for long growth interruption time in Figure 5.22f), holes of which density was almost the same as that of InP QDs were observed. Meaning that excess In atoms evaporated or migrated away from the QD for partially covered InP QDs during the first growth interruption, resulting in the formation of more uniform QDs. For the reference sample a slightly constant decrease in the transition time was observed, this suggests an accumulation of the In adatoms.

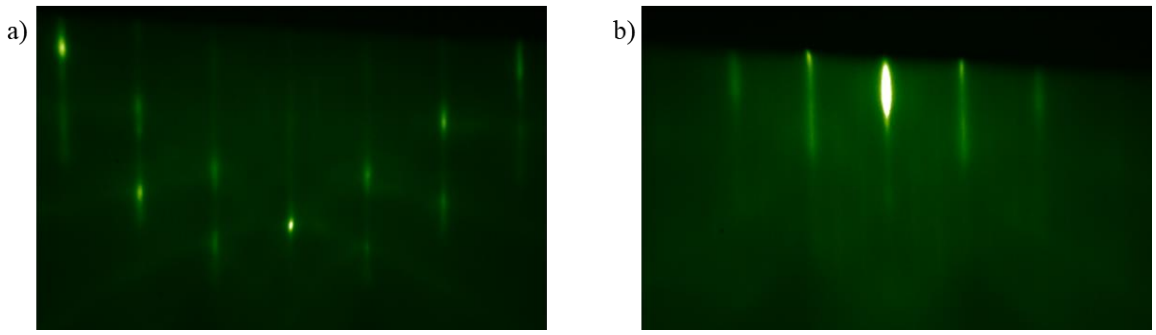

Figure 5.36 RHEED pattern images at the <110> direction from the 10th layer of the a) standard growth sample and b) the two-step growth interruption sample.

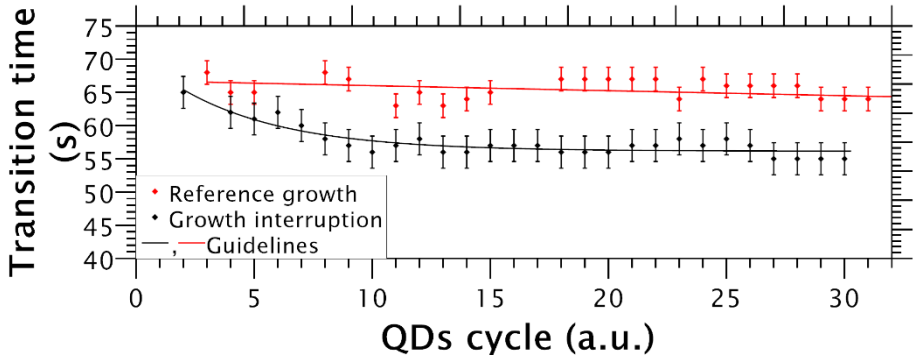

Figure 5.37 Graph of transition time of InP QD formation for the number of cycles obtained by the RHEED pattern monitoring of two samples with and without growth interruption. The transition time was measured from the 2nd and 3rd cycle for the two-step growth interruption and reference growth samples, respectively.

The size values of the QDs observed by cross-sectional TEM did not match those obtained from AFM; in general, similar tendencies of type-A and type-B formation were observed, but with slightly larger values. The AFM measurements can be used as a guide to observe the overall behavior of the QDs for the different growth parameters. Unfortunately, it can be considered as an exact measurement of the QD geometry due to the effects of unintentional annealing and quenching associated with the sample removal from the chamber process, as shown by Krzyzewski and Jones[101].

In Figure 5.38 it is shown cross-sectional TEM images of the 30 period InP/GaP QD structure grown with and without the two-step growth interruption process. For the sample without the growth interruption, the size of stacked QD increased and defects appeared in route of stacking [Figure 5.38(a)]. In contrast, sample with the proposed method, clear stacking of the InP QDs through the layers was present at [Figure 5.38(b)]. In this case, the height of the QDs was slightly increased from 3 to 4 nm from the bottom to the top layers. Through plan-view TEM measurements the density of the stacked columns was estimated. It was observed a difference in the shape of the dots associated to the stacked columns in both samples as shown in Figure 5.39 and an increase in the density for the two-step growth interruption method. Comparing with the cross-sectional images it was associated the larger dots to the stacked QDs with defects and the smaller regular circles associated with the free defect stacked columns. In the Figure 5.40 a bimodal distribution on the lateral size of the dots was observed, from the different peaks of the distribution it was possible to distinguish between the stacked columns with and without defects, with this an estimation of

the defect free columns was obtained. I calculated a 16.7% and 8.6% of defect columns for the standard growth and the two-step growth mode, respectively. The density of stacked columns (consisted of defect columns and defect free columns) was estimated as $N_s \sim 4.7 \times 10^9 cm^2$ and $N_s \sim 8.8 \times 10^9 cm^2$ for the standard growth and the two-step growth interruption, respectively, this means a density of defect columns of $N_D \sim 7.9 \times 10^8 cm^2$ and $N_D \sim 7.53 \times 10^8 cm^2$ for the standard growth and the two-step growth interruption, respectively. This Means an average distance of 106 nm between columns for the two-step growth interruption sample.

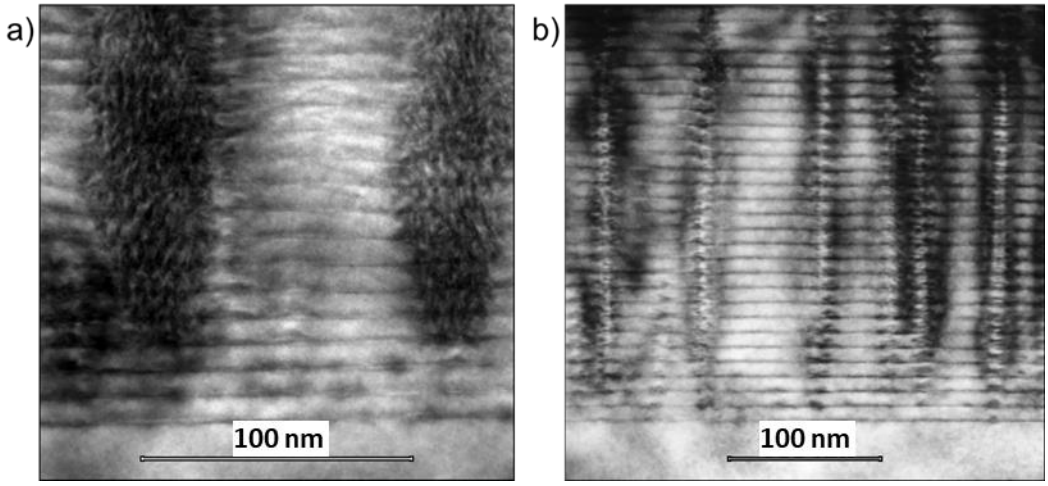

Figure 5.38 Cross-sectional TEM image of a 30 period InP/GaP sample showing defects generation (a) and stacked QDs (b) for a sample without and with the growth interruption process, respectively. Measurements were performed under bright-field conditions from the <110> direction.

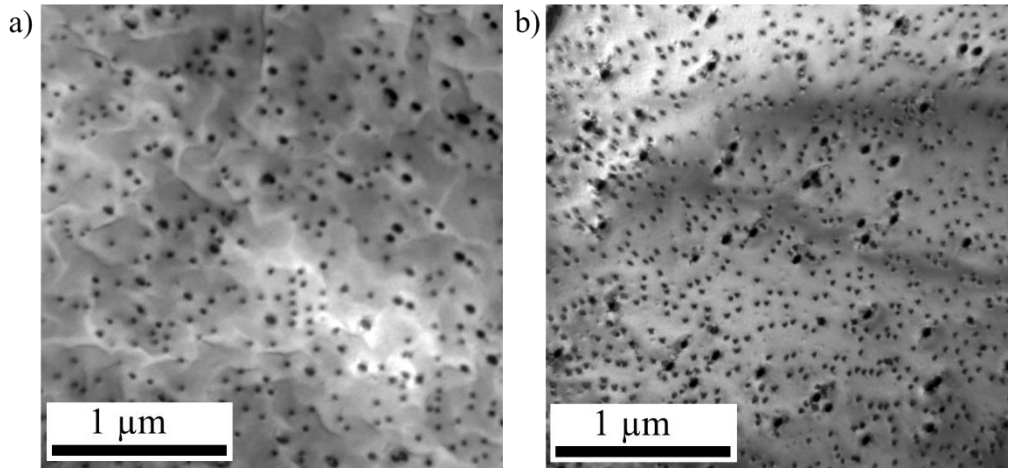

Figure 5.39 $2.7 \times 2.7\ \mu m$ plan-view TEM image of the sample by a) standard growth and b) with two-step growth interruption. Measurement was performed under bright-field conditions.

Due to the importance of a flat surface during the growth, the surface was corroborated by AFM, in the Figure 5.41 it is shown the AFM measurements of the standard growth and the two-step growth interruption samples, the generation of holes on both samples was observed with a depth mean value of -12.5 nm and -9.3 nm for the standard growth and two-step growth interruption sample, respectively. In the Figure 5.42 it is observed the influence of the stacked columns in the surface. Defect free columns after capping did not affect the surface and a flat surface was obtained, while defect columns modified the growth above them, and it propagated to the surface producing the holes observed in the AFM measurements. The density of the holes was measured, a value of $N_D \sim 1 \times 10^9 cm^2$ and $N_D \sim 7.13 \times 10^8 cm^2$ obtained from the AFM images, this means a percentual error of 26.9% for the standard growth and 5.2% for the two-step growth interruption mode compared to the values obtained from the TEM plan-view measurements. These values are presented in the Table 5-4. The closer values in the two-step growth interruption corroborates that the origin of the holes is the defect columns and the defect free columns do not produce a significant effect on the surface. The higher percentual error from the standard growth may be caused by the splice of the peaks obtained from the fitting of curve, as shown in the Figure 5.40 a clearer separation between the peaks is observed in the two-step growth interruption, this also suggest that the density of the defect columns obtained from the TEM plan-view measurements could be bigger.

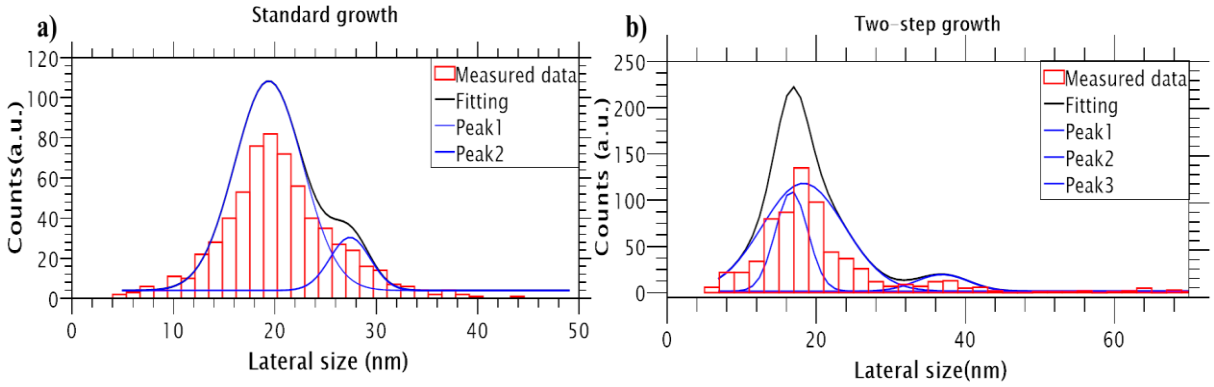

Figure 5.40 QD lateral size distribution obtained from plan-view TEM images for a) standard growth and b) with two-step growth interruption.

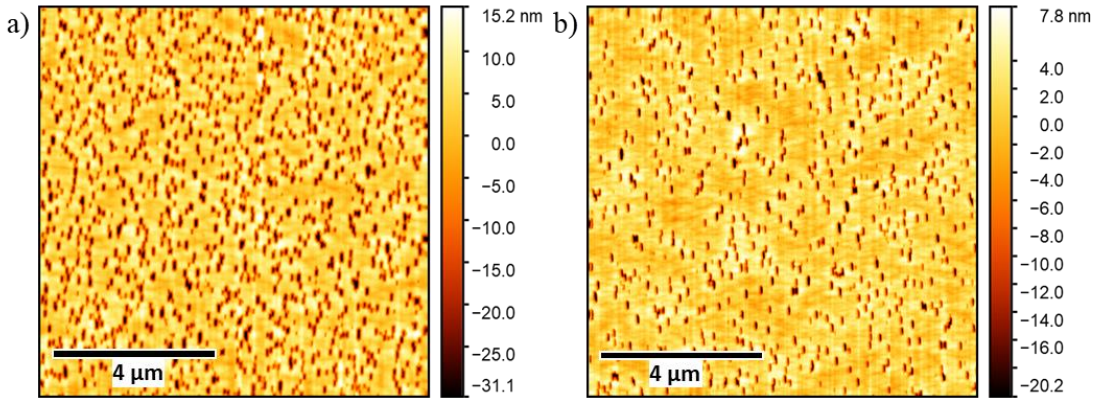

Figure 5.41 $10 \times 10\ \mu m$ AFM pictures of the surface after 20nm GaP capping on the final layer of the stacked InP columns for a) standard growth and b) two-step growth interruption method.

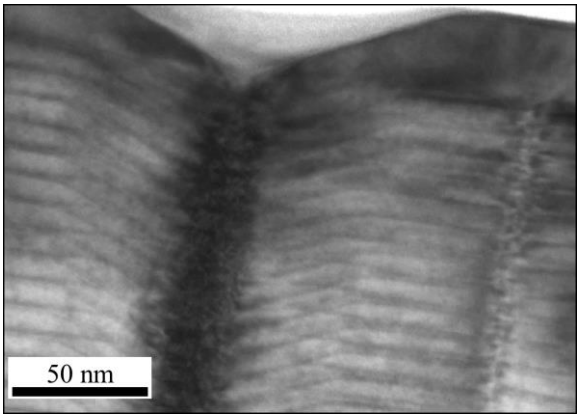

Figure 5.42 Cross-sectional TEM image the layers near the surface showing how defect columns modify the capped surface producing holes in the surface, while defect free columns do not.

Table 5-4 Density values of the total stacked QDs and defect columns for the standard growth and two-step growth interruption mode.

	Standard growth	**Two-step growth interruption**
Density of total Stacked QDs ($10^9 cm^2$)	4.73	8.78
Percentual fraction of defect columns by TEM	16.7 %	8.6 %
Density of defect columns ($10^9 cm^2$)	0.79	0.75
Density of holes by AFM ($10^9 cm^2$)	1	0.71

PL measurements of the standard growth and two step growth samples were performed, these measurements replicated the GaP layer measurements and no effect of InP was observed due to the low intensity obtained no information about the QDs was obtained.

5.4 Discussion

To produce a uniform distribution of QDs the precise control of the growth conditions is required. From the AFM measurements, a clear multimodal distribution of QDs was observed with a strong growth rate and V/III dependence. Temperature dependence was observed until high temperatures were reached, in which coarsening effects became significant. Porsche et al.[69] found that for InP/GaInP QDs with reduced surface diffusion growth conditions, type-A QDs are preferentially formed. In this study, the behavior is

opposite, suggesting that the surface diffusion is not the dominant process. The density and size of the type-B QDs increase with a higher growth rate and/or larger V/III ratio, suggesting that the growth rate of various facets form the QDs plays an important role. From AFM and/or TEM, type-A QDs has pyramidal shape surrounded by (111) facets, while the type-B QDs have a truncated pyramidal shape with (111) and (001) facets. In case of type-A QDs, the growth rate of the (001) facet is higher than that of the (111) facet, while type-B QDs, the opposite situation occurs. This suggests that for the high growth rate and/or high V/III ratio, the (111) facet is predominant, thus high-density type-B QDs occur, but for lower values, the opposite situation may occur. As shown in the Figure 5.6, 480˚ C of growth temperature is a very close temperature in which the desorption of most of the In adatom occurs, this means that the diffusion in this range is high. In this regime two main phenomenon affects the formation of the QDs, desorption and coalescence of QD. The desorption reduces the overall size of the QD whereas that coalescence contributes to the increase of the size. Since both phenomenon occurs at the same time, it is expected that the effects of both are present. On one side type-A QDs due to the desorption effect and type-B due to coalescence by high diffusion lengths. This can be noticed with the growth rate variation. With a low growth rate, the required time to deposit the same amount of ad atoms is longer and desorption occurs for a longer period. With a higher growth rate, less desorption occurs so that larger amount of type-B QDs remain. This effect can be observed in the Figure 5.15 where the amount of type-B QDs are reduced with growth rate. The appearance of type-A' dots may occur under specific conditions, and further work is required to understand the complete mechanism.

The InP QD growth conditions used for most of the samples were far from typical ones for InP homoepitaxy, i.e., very low growth rate and very low P overpressure. Considering these situations, the effect of the V/III ratio and/or growth rate on InP QD size can be dominated by the rate of P desorption from the various facet surfaces that form the InP island. Under optimized growth conditions, the nucleation of type-B QDs was significantly reduced, which enables the stacking of coherent QDs. From these conditions the capping process, meaning the GaP growth parameters are also significant for the stacking process. As shown in the Figure 5.38, despite the optimized growth conditions, during standard growth of GaP layers strain induced by the capped QDs makes the adsorption of In atoms more stable on top of the QDs, increasing the size for every subsequent cycle originating defects through the structure. The growth interruption process produced desorption of excess In atoms which helped to control the size and uniformity of the QDs significantly reducing the formation of defects. The estimation of GaP diffusion lengths for these growth conditions showed an anisotropic behavior, this situation may contribute with the capping of the partial capped QDs and improve the capping layer roughness. In the case of the formation of holes due to the defect formation during the stacking InP QDs, hole's lateral size could reach over 100nm length, this value exceeded the estimated diffusion length for these conditions. It may be possible to reduce the defect generation with longer diffusion lengths although further research is required. From the TEM samples it was observed a slighter improvement in the GaP capping layer after the growth interruption after the deposition of the capping layer. This step is important due to the diffusion of the adatoms into the rough capping layer formed due to the deposition of the InP QDs. Since a smooth capping layer can is required for the reduction of larger dots which generates defects in the subsequent layers. Defect measurement can be made by AFM measurements due to the formation of holes; this was corroborated by TEM cross sectional images. The implementation of strain compensation layers is expected to improve the quality of the structure. In flushing contributed to the diffusion of In atoms through the capping layer allowing the desorption of these, this showed big potential for controlling QDs geometry to reduce type-B QDs, unfortunately under the studied parameters it resulted in a strong reduction of QD density and desorption, further study would allow to be incorporated in the process.

5.5 Summary

Growth conditions of InP homoepitaxy and heteroepitaxy on GaP were studied, growth temperature showed a significant dependence on InP homoepitaxy surface, while for InP QDs the dependence was only observed at the higher temperatures in which the desorption of In atoms occurred. Strong dependence was observed on growth rate and V/III ratio. QDs showed multimodal size distribution for a vast range of growth parameters, smaller QDs with better size distributions were obtained under low growth rate and V/III ratio. Type A' QDs suggested a complicated growth process that should be further study. Bigger QDs presented the formation of defects which propagates to the upper layers of the growth.

QD size can be controlled by growth interruption, In flushing and the capping process. These processes are related with the diffusion of the In atoms for which the temperature and the duration have a strong dependence. In flushing showed the strongly exhibit this behavior by the desorption of the QDs. With the mentioned growth parameters QDs size that matches with the calculated dimension for the two-junction solar cell were obtained.

Capping layer thickness of QDs showed a strong dependence on the QDs height for the successful stacking. Optimized growth parameters and capping layer thickness allowed stacking of QDs, due to the strain fields which promoted the nucleation if the bigger QDs defects occurred on the stacked layers. The two-step growth interruption helped in the control of maximum height of QDs decreasing the number of defect columns generated, first by limiting the maximum height of the QD by the growth desorption of the partial capped QDs and second by the flattening of the capping layer with the second growth interruption. Measurement of defect columns was possible by TEM plan view and AFM, being consisted.

The optimized growth condition of 0.025 ML/s and V/III ratio of 20 along with a two-step growth interruption process successfully achieved vertical stacking of 30 period InP/GaP QD structure with good crystal quality, without the introduction of strain compensation layers. This is an important achievement in stacked QDs for carrier extraction.

For the target solar cell structure, it is planned to employ a GaAsPN grown on Si with a GaP buffer layer. In this work the stacking of InP QDs was not performed with a Si substrate due to time issues and since good quality GaP/Si have been achieved in the laboratory. One more important issue that may arise is the generation of defects during the GaAsPN capping layer since the introduction of InP may generate point defects. For the Targeted solar cell, the first issue is a Good quality GaP/Si heteroepitaxy. With the diffusion length study, I have estimated growth conditions in which diffusion anisotropy is observed and this knowledge is useful in the antiphase domains self-annihilation, since it is possible to estimate diffusion lengths based on the island formation on the GaP layer.

Chapter 6 Summary and Conclusions

In this work a novel structure for multilayered III-V-N/Si solar cell was proposed with theoretical calculations of its band alignments. Based on the calculation results, growth study of InP quantum dots was performed on InP/GaP matrix as the first approach to obtain the desired structure. To obtain better understanding of the growth mechanism of defect free GaP/Si heteroepitaxy the diffusion mechanism of the GaP was studied by the estimation of the diffusion lengths of two different directions during MBE growth. The morphology study of the InP QDs nucleation on a GaP matrix was performed for a wide range of growth conditions. Finally, for optimized conditions along with a two-step growth interruption it was shown a good quality 30-period stacked InP QDs layer without the introduction of strain compensation layers.

The general results can be summarized as follows:

The diffusion length of Ga adatom was estimated by using a one-dimensional diffusion growth model and their temperature dependence was discussed on two principal axes. It is quantitatively clarified that the diffusion length of the Ga adatoms increased with the temperature. Directional anisotropy in the diffusion length was observed along the $< 110 >$ and $< 1\bar{1}0 >$ directions. This anisotropy was highly consistent with a surface morphology i.e., elongation of the growth island along the $< 1\bar{1}0 >$ direction is also consistent with the larger diffusion length value along $< 1\bar{1}0 >$ direction. The diffusion length in GaP is related to the morphology of the islands and the orientation of this islands it´s determined by the longer value for the diffusion length. It seems that the diffusion mechanism is affected by the interaction of Ga adatom and the dimers of the (2×4) surface reconstruction. For MEE growth, the estimation of the diffusion length may not be suitable with the current model due to the growth mechanism.

In the InP QD study, a clear multimodal distribution of QDs was observed with a strong growth rate and V/III dependence. Two types of QDs were observed characterized by their geometry. It was found that, for a low growth rate and V/III ratio, more uniform and smaller QDs can be achieved, Suggesting that the growth rate of the various facets from the QDs plays an important role. A transition in QD size was observed for specific conditions. Since the nucleation of larger QDs tends to generate crystal defects, these are not the optimal conditions for the implementation of QDs in V-III-N/Si solar cells. To prevent the nucleation of bigger size QDs capping process, growth interruption and In flushing was studied. These processes are related with the diffusion and desorption of In atoms. Coarsening during growth interruption of InP QDs leads to the formation of bigger QDs and defect. Growth interruption of uncapped QDs allowed the control in the maximum height of the QDs, but if the process is extended for long time it resulted in the desorption of capped QDs, similarly In flushing showed to desorption of QDs.

With the stacking of several InP layers the overall geometry increased, resulting the formation of crystal defects towards the top of the structure. The capping process played a significant role in the stacking structure. Long growth interruption of the capping layer can desorb completely or promote the segregation of In atoms of any partially covered InP QD resulting in the degradation of the structure by the appearance of the holes. With the optimization of this process removal of excess In atoms achieved the control of the QD height. A second growth interruption process after the end of the GaP capping layer improved the flattening of the GaP layer. Finally, with optimized growth conditions and the two-step growth interruption process a significant improve in the QD stacking structure was possible.

6.1 Suggestions for future work

For the diffusion length study, growth rate and V/III parameters can be studied, also a more extensive study in the diffusion lengths by MEE, a revision of the model employed for the MEE conditions and the growth of more samples for different temperatures. Without the direct measurement of the diffusion lengths, it is still possible to estimate at least the anisotropy by the observation of the formed islands in the surface for the different growth conditions.

In the morphology study it was mentioned the transition from type-A to type- A' QDs, the growth conditions behavior has not been discovered, so the mechanism is not understood.

Characterization of the band gap and band alignment of the QDs is required, the weak signal provided by PL made it difficult to measure the value for these conditions. A more exhaustive work is required for this part.

Further improvement of the stacking structure is possible. As the transition time shown a decrease to a constant value, It is possible to reduce the amount of In supplied to continue decreasing the formation of larger QDs. This can be done by the observation of the RHEED pattern. If this kind of experiments provides an improvement of the stacking structure, it opens the possibility of change the growth conditions of the InP QDs. This may be necessary if in the more precise control of the QDs size.

In flushing conditions can be optimized for InP, a lower temperature can be employed, also the effect of the In flushing not for every layer but for a set of layers can be studied.

During the transition time measurement by the two-step growth interruption process the reduction of InP thickness based on the transition time can be studied, this would prevent the formation of type-B dots while achieve the formation of QDs.

The next step of this study would be the morphology study of InP QDs on GaAsPN, and the comparation with the results obtained in this work, thereafter, the stacking study with these materials, the results and the methodology of this work can be easily employed in this new structure. In addition, the clarification of the band alignment and the band gap values is needed, if the estimated size does not achieve the desired values further research would be needed.

The implementation of strain compensation layers would be needed for an adequate thickness of a solar cell.

And finally, the integration of the structure to a Si substrate.

References

[1] D. M. Chapin, C. S. Fuller, and G. L. Pearson, "A New Silicon p-n Junction Photocell for Converting Solar Radiation into Electrical Power," *J. Appl. Phys.*, vol. 25, no. 5, pp. 676–677, May 1954, doi: 10.1063/1.1721711.

[2] V. Petrova-Koch, "Milestones of Solar Conversion and Photovoltaics," in *High-Efficient Low-Cost Photovoltaics: Recent Developments*, V. Petrova-Koch, R. Hezel, and A. Goetzberger, Eds. Cham: Springer International Publishing, 2020, pp. 1–7.

[3] M. A. Green, Y. Hishikawa, E. D. Dunlop, D. H. Levi, J. Hohl-Ebinger, and A. W. Y. Ho-Baillie, "Solar cell efficiency tables (version 52)," *Prog. Photovoltaics Res. Appl.*, vol. 26, no. 7, pp. 427–436, 2018, doi: https://doi.org/10.1002/pip.3040.

[4] W. Shockley and H. J. Queisser, "Detailed Balance Limit of Efficiency of p-n Junction Solar Cells," *J. Appl. Phys.*, vol. 32, no. 3, pp. 510–519, 1961, doi: 10.1063/1.1736034.

[5] L. C. Hirst and N. J. Ekins-Daukes, "Fundamental losses in solar cells," *Prog. Photovoltaics Res. Appl.*, 2011, doi: 10.1002/pip.1024.

[6] N. Taylor, *Guidelines for PV power measurement in industry*. 2010.

[7] C. Kittel, "Introduction to Solid State Physics, 8th edition," *Wiley & Sons, New York, NY*. 2004.

[8] M. A. Green *et al.*, "Solar cell efficiency tables (Version 53)," *Prog. Photovoltaics Res. Appl.*, vol. 27, no. 1, pp. 3–12, 2019, doi: 10.1002/pip.3102.

[9] M. Green, E. Dunlop, J. Hohl-Ebinger, M. Yoshita, N. Kopidakis, and X. Hao, "Solar cell efficiency tables (version 57)," *Prog. Photovoltaics Res. Appl.*, vol. 29, no. 1, pp. 3–15, 2021, doi: 10.1002/pip.3371.

[10] F. Shimura, "Single-Crystal Silicon: Growth and Properties," in *Springer Handbook of Electronic and Photonic Materials*, S. Kasap and P. Capper, Eds. Cham: Springer International Publishing, 2017, p. 1.

[11] M. D. Archer and R. Hill, *Clean electricity from photovoltaics. London: Imperial College Press*, vol. 1. 2001.

[12] Y. Abdulraheem, I. Gordon, T. Bearda, H. Meddeb, and J. Poortmans, "Optical bandgap of ultra-thin amorphous silicon films deposited on crystalline silicon by PECVD," *AIP Adv.*, vol. 4, no. 5, 2014, doi: 10.1063/1.4879807.

[13] J. Loferski, "Theoretical Considerations Governing the Choice of the Optimum Semiconductor for Photovoltaic Solar Energy Conversion," *J. Appl. Phys.*, vol. 27, pp. 777–784, 1956.

[14] D. A. Cusano, "CdTe solar cells and photovoltaic heterojunctions in II–VI compounds," *Solid. State. Electron.*, vol. 6, no. 3, pp. 217–232, 1963, doi: https://doi.org/10.1016/0038-1101(63)90078-9.

[15] H. J. T. Nkuissi, F. K. Konan, B. Hartiti, and J.-M. Ndjaka, "Toxic Materials Used in Thin Film Photovoltaics and Their Impacts on Environment," in *Reliability and Ecological Aspects of Photovoltaic Modules*, A. Gok, Ed. Rijeka: IntechOpen, 2020.

[16] R. W. Miles, K. M. Hynes, and I. Forbes, "Photovoltaic solar cells: An overview of state-of-the-art cell development and environmental issues," *Prog. Cryst. Growth Charact. Mater.*, vol. 51, no. 1–3, pp. 1–42, 2005, doi: 10.1016/j.pcrysgrow.2005.10.002.

[17] T. Markvart and L. Castañer, *Practical Handbook of Photovoltaics: Fundamentals and Applications*. 2003.

[18] K. Summers and J. Radde, "Potential health and environmental impacts associated with the manufacture and use of photovoltaic cells," no. August, 2004.

[19] B. O'Regan and M. Grätzel, "A low-cost, high-efficiency solar cell based on dye-sensitized colloidal TiO2 films," *Nature*, 1991, doi: 10.1038/353737a0.

[20] M. Grätzel, "Dye-sensitized solar cells," *J. Photochem. Photobiol. C Photochem. Rev.*, vol. 4, no. 2, pp. 145–153, 2003, doi: 10.1016/S1389-5567(03)00026-1.

[21] Y. Cao *et al.*, "11% efficiency solid-state dye-sensitized solar cells with copper(II/I) hole transport materials," *Nat. Commun.*, vol. 8, pp. 1–8, 2017, doi: 10.1038/ncomms15390.

[22] N.-G. Park, "Organometal Perovskite Light Absorbers Toward a 20% Efficiency Low-Cost Solid-State Mesoscopic Solar Cell," *J. Phys. Chem. Lett.*, vol. 4, no. 15, pp. 2423–2429, Aug. 2013, doi: 10.1021/jz400892a.

[23] C. S. Ponseca *et al.*, "Organometal Halide Perovskite Solar Cell Materials Rationalized: Ultrafast Charge Generation, High and Microsecond-Long Balanced Mobilities, and Slow Recombination," *J. Am. Chem. Soc.*, vol. 136, no. 14, pp. 5189–5192, Apr. 2014, doi: 10.1021/ja412583t.

[24] S. P. Singh and P. Nagarjuna, "Organometal halide perovskites as useful materials in sensitized solar cells," *Dalt. Trans.*, vol. 43, no. 14, pp. 5247–5251, 2014, doi: 10.1039/C3DT53503G.

[25] M. Jeong *et al.*, "Stable perovskite solar cells with efficiency exceeding 24.8% and 0.3-V voltage loss," *Science (80-.).*, vol. 369, no. 6511, pp. 1615–1620, 2020, doi: 10.1126/science.abb7167.

[26] A. De Vos, "Detailed balance limit of the efficiency of tandem solar cells," *J. Phys. D. Appl. Phys.*, vol. 13, no. 5, pp. 839–846, May 1980, doi: 10.1088/0022-3727/13/5/018.

[27] R. Cariou *et al.*, "III-V-on-silicon solar cells reaching 33% photoconversion efficiency in two-terminal configuration," *Nat. Energy*, 2018, doi: 10.1038/s41560-018-0125-0.

[28] T. Takamoto, H. Washio, and H. Juso, "Application of InGaP/GaAs/InGaAs triple junction solar cells to space use and concentrator photovoltaic," 2014, doi: 10.1109/PVSC.2014.6924936.

[29] R. R. King *et al.*, "40% efficient metamorphic GaInPGaInAsGe multijunction solar cells," *Appl. Phys. Lett.*, 2007, doi: 10.1063/1.2734507.

[30] J. F. Geisz *et al.*, "Six-junction III–V solar cells with 47.1% conversion efficiency under 143 Suns concentration," *Nat. Energy*, 2020, doi: 10.1038/s41560-020-0598-5.

[31] N. H. Karam *et al.*, "Recent developments in high-efficiency Ga0.5In0.5P/GaAs/Ge dual- and triple-junction solar cells: Steps to next-generation PV cells," *Sol. Energy Mater. Sol. Cells*, 2001, doi: 10.1016/S0927-0248(00)00207-5.

[32] R. R. King *et al.*, "40% efficient metamorphic GaInPGaInAsGe multijunction solar cells," *Appl. Phys. Lett.*, vol. 90, no. 18, pp. 90–93, 2007, doi: 10.1063/1.2734507.

[33] F. Dimroth *et al.*, "Wafer bonded four-junction GaInP/GaAs//GaInAsP/GaInAs concentrator solar cells with 44.7% efficiency," *Prog. Photovoltaics Res. Appl.*, 2014, doi: 10.1002/pip.2475.

[34] L. Cuadra, A. Martí, and A. Luque, "Present status of intermediate band solar cell research," *Thin Solid Films*, vol. 451–452, pp. 593–599, 2004, doi: 10.1016/j.tsf.2003.11.047.

[35] A. Luque and A. Martí, "Increasing the Efficiency of Ideal Solar Cells by Photon Induced Transitions at Intermediate Levels," *Phys. Rev. Lett.*, vol. 78, no. 26, pp. 5014–5017, 1997, doi: 10.1103/PhysRevLett.78.5014.

[36] A. Martí *et al.*, “Six not-so-easy pieces in intermediate band solar cell research,” doi: 10.1117/1.JPE.3.031299.

[37] A. Luque, A. Martí, E. Antolín, and C. Tablero, “Intermediate bands versus levels in non-radiative recombination,” *Phys. B Condens. Matter*, vol. 382, no. 1–2, pp. 320–327, 2006, doi: 10.1016/j.physb.2006.03.006.

[38] N. López, L. A. Reichertz, K. M. Yu, K. Campman, and W. Walukiewicz, “Engineering the Electronic Band Structure for Multiband Solar Cells,” *Phys. Rev. Lett.*, vol. 106, no. 2, p. 28701, Jan. 2011, doi: 10.1103/PhysRevLett.106.028701.

[39] K. Zelazna *et al.*, “Photoreflectance studies of optical transitions in GaNPAs intermediate band solar cell absorbers,” *Sol. Energy Mater. Sol. Cells*, vol. 188, no. April, pp. 99–104, 2018, doi: 10.1016/j.solmat.2018.08.024.

[40] T. Tanaka, K. Saito, Q. Guo, K. M. Yu, and W. Walukiewicz, “Improved photovoltaic properties of ZnTeO-based intermediate band solar cells,” in *Physics, Simulation, and Photonic Engineering of Photovoltaic Devices VII*, 2018, vol. 10527, pp. 130–135, doi: 10.1117/12.2292911.

[41] T. Tayagaki and T. Sugaya, “Type-II InP quantum dots in wide-bandgap InGaP host for intermediate-band solar cells,” *Appl. Phys. Lett.*, vol. 108, no. 15, pp. 1–6, 2016, doi: 10.1063/1.4946761.

[42] T. Tanoue and H. Sakaki, “A new method to control impact ionization rate ratio by spatial separation of avalanching carriers in multilayered heterostructures,” *Appl. Phys. Lett.*, vol. 41, no. 1, pp. 67–70, 1982, doi: 10.1063/1.93331.

[43] A. Louwen, W. G. J. H. M. Van Sark, A. P. C. Faaij, and R. E. I. Schropp, “Re-assessment of net energy production and greenhouse gas emissions avoidance after 40 years of photovoltaics development,” *Nat. Commun.*, vol. 7, pp. 1–9, 2016, doi: 10.1038/ncomms13728.

[44] S. Almosni *et al.*, “Evaluation of InGaPN and GaAsPN materials lattice-matched to Si for multi-junction solar cells,” *J. Appl. Phys.*, vol. 113, no. 12, 2013, doi: 10.1063/1.4798363.

[45] S. Nacer and A. Aissat, “Simulation and optimization of current and lattice matching double-junction GaNAsP/Si solar cells,” *Superlattices Microstruct.*, vol. 89, pp. 242–251, 2016, doi: 10.1016/j.spmi.2015.11.001.

[46] D. A. Kudryashov, A. S. Gudovskikh, E. V. Nikitina, and A. Y. Egorov, “Design of multijunction GaPNAs/Si heterostructure solar cells by computer simulation,” *Semiconductors*, vol. 48, no. 3, pp. 381–386, 2014, doi: 10.1134/S1063782614030154.

[47] H. Kroemer, “Polar-on-nonpolar epitaxy,” *J. Cryst. Growth*, vol. 81, no. 1–4, pp. 193–204, Feb. 1987, doi: 10.1016/0022-0248(87)90391-5.

[48] A. C. Lin, M. M. Fejer, and J. S. Harris, “Antiphase domain annihilation during growth of GaP on Si by molecular beam epitaxy,” *J. Cryst. Growth*, vol. 363, pp. 258–263, 2013, doi: 10.1016/j.jcrysgro.2012.10.055.

[49] K. Yamane *et al.*, “Growth of a lattice-matched GaAsPN p–i–n junction on a Si substrate for monolithic III–V/Si tandem solar cells,” *Appl. Phys. Express*, vol. 10, 2017, [Online]. Available: http://iopscience.iop.org/1882-0786/10/7/075504.

[50] C. Ratcliff, T. J. Grassman, J. A. Carlin, and S. A. Ringel, “High temperature step-flow growth of gallium phosphide by molecular beam epitaxy and metalorganic chemical vapor deposition,” *Appl. Phys. Lett.*, vol. 99, no. 14, 2011, doi: 10.1063/1.3644956.

[51] J. A. Piedra-Lorenzana *et al.*, “Estimation of Ga adatom diffusion length for GaP growth by molecular beam epitaxy,” *J. Cryst. Growth*, vol. 512, no. February, pp. 37–40, Apr. 2019, doi: 10.1016/j.jcrysgro.2019.02.008.

[52] C. Cornet *et al.*, “Zinc-blende group III-V/group IV epitaxy: Importance of the miscut,” *Phys. Rev. Mater.*, vol. 4, no. 5, 2020, doi: 10.1103/PhysRevMaterials.4.053401.

[53] K. Yamane, T. Kawai, Y. Furukawa, H. Okada, and A. Wakahara, “Growth of low defect density GaP layers on Si substrates within the critical thickness by optimized shutter sequence and post-growth annealing,” *J. Cryst. Growth*, vol. 312, no. 15, pp. 2179–2184, 2010, doi: 10.1016/j.jcrysgro.2010.04.038.

[54] S. Sukrittanon *et al.*, “Enhanced conversion efficiency in wide-bandgap GaNP solar cells,” *Appl. Phys. Lett.*, vol. 107, no. 15, 2015, doi: 10.1063/1.4933317.

[55] A. Y. Cho and J. R. Arthur, “Molecular beam epitaxy,” *Prog. Solid State Chem.*, 1975, doi: 10.1016/0079-6786(75)90005-9.

[56] J. Jeans, *An Introduction to the Kinetic Theory of Gases*. Cambridge University Press, 1982.

[57] C. T. Foxon and B. A. Joyce, “Interaction kinetics of As4 and Ga on {100} GaAs surfaces using a modulated molecular beam technique,” *Surf. Sci.*, 1975, doi: 10.1016/0039-6028(75)90035-7.

[58] C. T. Foxon and B. A. Joyce, “Interaction kinetics of As2 and Ga on {100} GaAs surfaces,” *Surf. Sci.*, 1977, doi: 10.1016/0039-6028(77)90273-4.

[59] E. A. Wood, “Vocabulary of Surface Crystallography,” *J. Appl. Phys.*, vol. 35, no. 4, pp. 1306–1312, Apr. 1964, doi: 10.1063/1.1713610.

[60] J. J. Lander and J. Morrison, “Low-Energy Electron Diffraction Study of Silicon Surface Structures,” *J. Chem. Phys.*, vol. 37, no. 4, pp. 729–746, Aug. 1962, doi: 10.1063/1.1733155.

[61] J. A. Appelbaum, G. A. Baraff, and D. R. Hamann, “The Si (100) surface. III. Surface reconstruction,” *Phys. Rev. B*, vol. 14, no. 2, pp. 588–601, Jul. 1976, doi: 10.1103/PhysRevB.14.588.

[62] Y. J. Li *et al.*, “Origin of $p(2\ifmmode\times\else\texttimes\fi{}1)$ Phase on Si(001) by Noncontact Atomic Force Microscopy at 5 K,” *Phys. Rev. Lett.*, vol. 96, no. 10, p. 106104, Mar. 2006, doi: 10.1103/PhysRevLett.96.106104.

[63] I. Daruka and A. L. Barabási, “Dislocation-Free Island Formation in Heteroepitaxial Growth: A Study at Equilibrium,” *Phys. Rev. Lett.*, vol. 79, no. 19, pp. 3708–3711, 1997, doi: 10.1103/PhysRevLett.79.3708.

[64] J. W. Matthews and A. E. Blakeslee, “Defects in epitaxial multilayers: I. Misfit dislocations,” *J. Cryst. Growth*, vol. 27, pp. 118–125, 1974, doi: https://doi.org/10.1016/S0022-0248(74)80055-2.

[65] P. B. Joyce *et al.*, “Growth rate effects on the size, composition and optical properties of InAs/GaAs quantum dots grown by molecular beam epitaxy,” *J. Cryst. Growth*, vol. 227–228, pp. 1000–1004, 2001, doi: 10.1016/S0022-0248(01)00967-8.

[66] F. Hatami *et al.*, “InP quantum dots embedded in GaP: Optical properties and carrier dynamics,” *Phys. Rev. B - Condens. Matter Mater. Phys.*, vol. 67, no. 8, 2003, doi: 10.1103/PhysRevB.67.085306.

[67] M. Kawabe and T. Ueda, “Self-annihilation of antiphase boundary in gaas on si(100) grown by molecular beam epitaxy,” *Jpn. J. Appl. Phys.*, vol. 26, no. 6A, pp. 944–946, 1987, doi: 10.1143/JJAP.26.L944.

[68] K. Yoshikawa *et al.*, “Silicon heterojunction solar cell with interdigitated back contacts for a photoconversion efficiency over 26%,” *Nat. Energy*, 2017, doi: 10.1038/nenergy.2017.32.

[69] J. Porsche, A. Ruf, M. Geiger, and F. Scholz, “Size control of self-assembled InP/GaInP quantum islands,” *J. Cryst. Growth*, vol. 195, no. 1–4, pp. 591–595, 1998, doi: 10.1016/S0022-0248(98)00570-3.

[70] Y. Nabetani, K. Sawada, Y. Furukawa, a Wakahara, S. Noda, and a Sasaki, “Self-assembled InP islands grown on GaP substrate,” *J. Cryst. Growth*, vol. 193, no. June, pp. 470–477, 1998, doi: 10.1016/S0022-0248(98)00545-4.

[71] W. T. Masselink, F. Hatami, G. Mussler, and L. Schrottke, “InP quantum dots in (1 0 0) GaP: Growth and luminescence,” *Mater. Sci. Semicond. Process.*, vol. 4, no. 6, pp. 497–501, 2001, doi: 10.1016/S1369-8001(02)00008-2.

[72] F. Hatami, W. T. Masselink, and L. Schrottke, “Radiative recombination from InP quantum dots on (100) GaP,” *Appl. Phys. Lett.*, vol. 78, no. 15, pp. 2163–2165, 2001, doi: 10.1063/1.1361277.

[73] J. F. Geisz and D. J. Friedman, “III-N-V semiconductors for solar photovoltaic applications,” *Semicond. Sci. Technol.*, 2002, doi: 10.1088/0268-1242/17/8/305.

[74] K. Yamane, N. Urakami, H. Sekiguchi, and A. Wakahara, “III-V-N compounds for multi-junction solar cells on Si,” *2014 IEEE 40th Photovolt. Spec. Conf. PVSC 2014*, pp. 2792–2796, 2014, doi: 10.1109/PVSC.2014.6925509.

[75] K. Derendorf *et al.*, “Fabrication of GaInP/GaAs//Si solar cells by surface activated direct wafer bonding,” *IEEE J. Photovoltaics*, 2013, doi: 10.1109/JPHOTOV.2013.2273097.

[76] S. Birner *et al.*, “Nextnano: General purpose 3-D simulations,” *IEEE Trans. Electron Devices*, 2007, doi: 10.1109/TED.2007.902871.

[77] B. A. Joyce and D. D. Vvedensky, “Self-organized growth on GaAs surfaces,” *Mater. Sci. Eng. R Reports*, vol. 46, no. 6, pp. 127–176, 2004, doi: 10.1016/j.mser.2004.10.001.

[78] P. Michler, *Single Quantum Dots: Fundamentals, Applications and New Concepts*. Springer, 2003.

[79] L. E. Brus, “Electron-electron and electron-hole interactions in small semiconductor crystallites: The size dependence of the lowest excited electronic state,” *J. Chem. Phys.*, 1984, doi: 10.1063/1.447218.

[80] T. Kippeny, L. A. Swafford, and S. J. Rosenthal, “Semiconductor nanocrystals: A powerful visual aid for introducing the particle in a box,” *J. Chem. Educ.*, 2002, doi: 10.1021/ed079p1094.

[81] M. Gutiérrez *et al.*, “Critical barrier thickness for the formation of InGaAs/GaAs quantum dots,” *Mater. Sci. Eng. C*, vol. 25, no. 5–8, pp. 798–803, 2005, doi: 10.1016/j.msec.2005.06.052.

[82] Y. Furukawa, S. Noda, M. Ishii, a. Wakahara, and a. Sasaki, “Stacking number dependence of size distribution of vertically stacked InAs/GaAs quantum dots,” *J. Electron. Mater.*, vol. 28, no. 5, pp. 452–456, 1999, doi: 10.1007/s11664-999-0095-x.

[83] Z. R. Wasilewski, S. Fafard, and J. P. McCaffrey, “Size and shape engineering of vertically stacked self-assembled quantum dots,” *J. Cryst. Growth*, vol. 201, pp. 1131–1135, 1999, doi: 10.1016/S0022-0248(98)01539-5.

[84] H. Sasakura, S. Kayamori, S. Adachi, and S. Muto, “Effect of indium-flush method on the control of photoluminescence energy of highly uniform self-assembled InAs quantum dots by slow molecular beam epitaxy growth,” *J. Appl. Phys.*, vol. 102, no. 1, 2007, doi: 10.1063/1.2752598.

[85] G. Lian, J. Yuan, L. Brown, G.-H. Kim, and D. Ritchie, “Modification of InAs quantum dot structure by the growth of the capping layer,” *Appl. Phys. Lett.*, vol. 73, pp. 49–51, Jul. 1998, doi: 10.1063/1.121719.

[86] P. W. Voorhees, “The Theory of Ostwald Ripening,” *J. Stat. Phys.*, vol. 38, no. 1/2, pp. 231–252, 1985, [Online]. Available: internal-pdf://217.141.214.65/Voorhees-1985-The theory of Ostwald ripening.pdf internal-pdf://2141644038/Voorhees-1985-The theory of Ostwald ripening1.pdf.

[87] J. Kim *et al.*, “Growth mechanism of highly uniform InAs/GaAs quantum dot with periodic arsine interruption by metalorganic chemical vapor deposition,” *J. Appl. Phys.*, vol. 110, no. 4, 2011, doi: 10.1063/1.3624665.

[88] C. G. de Walle, “Band lineups and deformation potentials in the model-solid theory,” *Phys. Rev. B*, vol. 39, no. 3, pp. 1871–1883, 1989, doi: 10.1103/PhysRevB.40.10632.

[89] G. B. Bachelet, D. R. Hamann, and M. SchÏter, “Pseudopotentials that work: From H to Pu,” *Phys. Rev. B*, vol. 26, no. 8, pp. 4199–4228, 1982, doi: 10.1103/PhysRevB.26.4199.

[90] J.E. Ayers and J. E. Ayers, *Heteroepitaxy of Semiconductors: Theory, Growth, and Characterization*. 2007.

[91] X. Q. Shen, D. Kishimoto, and T. Nishinaga, “Arsenic pressure dependence of surface diffusion of ga on nonplanar gaas substrates,” *Jpn. J. Appl. Phys.*, vol. 33, no. 1R, p. 11, 1994, doi: 10.1143/JJAP.33.11.

[92] T. Nishinaga and A. Yamashiki, “Recent understandings of elementary growth processes in MBE of GaAs,” vol. 344, pp. 495–499, 1999.

[93] T. Sugaya, T. Nakagawa, Y. Sugiyama, Y. Tanuma, and K. Yonei, “Difference in Diffusion Length of Ga Atoms under As2 and As4 Flux in Molecular Beam Epitaxy ,” *Japanese J. Appl. Phys. Part 1 Regul. Pap. Short Notes Rev. Pap.*, vol. 36, pp. 5670–5673, 1997.

[94] M. López and Y. Nomura, “Surface diffusion length of Ga adatoms in molecular-beam epitaxy on GaAs(100)–(110) facet structures,” *J. Cryst. Growth*, vol. 150, no. 110, pp. 68–72, 1995, doi: 10.1016/0022-0248(95)80182-C.

[95] K. Ohta, T. Kojima, and T. Nakagawa, “Anisotropic surface migration of Ga atoms on GaAs (001),” *J. Cryst. Growth*, vol. 95, no. 1–4, pp. 71–74, 1989, doi: 10.1016/0022-0248(89)90354-0.

[96] 西永頌, 結晶成長. 朝倉書店, 2014.

[97] Y. Takagi, H. Yonezu, K. Samonji, T. Tsuji, and N. Ohshima, “Generation and suppression process of crystalline defects in GaP layers grown on misoriented Si(100) substrates,” *J. Cryst. Growth*, vol. 187, no. 1, pp. 42–50, 1998, doi: 10.1016/S0022-0248(97)00862-2.

[98] D. Leonard, K. Pond, and P. M. Petroff, “Critical layer thickness for self-assembled InAs islands on GaAs,” *Phys. Rev. B*, 1994, doi: 10.1103/PhysRevB.50.11687.

[99] K. Yamaguchi, K. Yujobo, and T. Kaizu, “Stranski-Krastanov growth of InAs quantum dots with narrow size distribution,” *Jpn. J. Appl. Phys.*, vol. 39, no. 12 A, pp. 1–5, 2000, doi: 10.1143/jjap.39.l1245.

[100] Q. Xie, A. Madhukar, P. Chen, and N. P. Kobayashi, “Vertically Self-Organized InAs Quantum Box Islands on GaAs(100),” *Phys. Rev. Lett.*, vol. 75, no. 13, pp. 2542–2545, Sep. 1995, doi: 10.1103/PhysRevLett.75.2542.

[101] T. J. Krzyzewski and T. S. Jones, “Ripening and annealing effects in InAs/GaAs(001) quantum dot formation,” *J. Appl. Phys.*, vol. 96, no. 1, pp. 668–674, 2004, doi: 10.1063/1.1759788.